RESEARCH ARTICLE

WILEY

Construction of hybrid 1D-0D networks for efficient and accurate blood flow simulations

Beatrice Ghitti[1] | **Pablo J. Blanco[2]** | **Eleuterio F. Toro[3]** | **Lucas O. Müller[1]**

[1]Department of Mathematics, University of Trento, Trento, Italy

[2]National Laboratory for Scientific Computing LNCC, Petrópolis, Brazil

[3]Laboratory of Applied Mathematics DICAM, University of Trento, Trento, Italy

Correspondence
Beatrice Ghitti, Department of Mathematics, University of Trento, via Sommarive, 14 - 38122, Trento, Italy.
Email: beatrice.ghitti@unitn.it

Funding information
University of Trento, Grant/Award Number: L. 232/2016; CNPq, Grant/Award Numbers: 301224/2016-1, 407751/2018-1; FAPESP, Grant/Award Number: 2014/50889-7

Abstract

The one-dimensional (1D) modeling of blood flow in complex networks of vessels and cardiovascular models can result in computationally expensive simulations. The complexity of such networks has significantly increased in the last years, in terms of both enhanced anatomical detail and modeling of physiological mechanisms and mechanical characteristics. To address such issue, the main goal of this work is to present a novel methodology to construct hybrid networks of coupled 1D and 0D vessels and to perform computationally efficient and accurate blood flow simulations in such networks. Departing from both the 1D and lumped-parameter (0D) nonlinear models for blood flow, we propose high-order numerical coupling strategies to solve the 1D, 0D, and hybrid coupling of vessels at junctions. To effectively construct hybrid networks, we explore different a-priori model selection criteria focusing in obtaining the best possible trade-off between computational cost of the simulations and accuracy of the computed solutions for the hybrid network with respect to the 1D network. The achievement of the expected order of accuracy is verified in several test cases. The novel methodology is applied to two different arterial networks, the 37-artery network and the reduced ADAN56 model, where, in order to identify the best performing *a-priori* model selection criteria, the quantitative assessment of CPU times and errors and the qualitative comparison between results are carried out and discussed.

KEYWORDS

a-priori model selection criteria, computational efficiency, high-order numerical schemes/couplings, hybrid 1D-0D networks, reduced-order blood flow models

1 | INTRODUCTION

In the last decades, modeling and simulation of blood flow have become of primary importance in different contexts, such as biomedical engineering, and with a vast range of applications, from basic research to clinic, either to study and understand the normal physiological function of the cardiovascular system or to investigate different pathological conditions. Cardiovascular modeling has been pursued using different levels of model complexity and sophistication, from lumped-parameter/zero-dimensional (0D) to distributed (1D and 3D) models. In this framework, one-dimensional

(1D) blood flow models represent a well-established and powerful approach to study hemodynamics, accurately describe wave propagation phenomena and predict pressure and flow waveforms in large vessels, at a reasonable computational cost. When compared to measurements from in vivo models[1,2] and to patient-specific data,[3,4] the computational results obtained from 1D blood flow models prove the ability of the 1D formulation to capture the main features of pressure pulse conformation and flow rate distribution in different vascular districts, offering a good balance between computational cost and accuracy. Hence, 1D blood flow models have been and are still extensively used to simulate and study wave propagation phenomena in arterial networks and, just in the last years, also in the venous circulation. Key contributions in this field include the works of Aviolo,[5] Stergiopulos et al.,[6] Olufsen et al.,[7] Formaggia et al.,[8] Sherwin et al.,[9] Mynard and Nithiarasu,[10] Reymond et al.,[11,12] and, more recently, of Müller and Toro,[4,13] Blanco et al.[3,14] and Mynard and Smolich.[15] The complexity of vessel networks used in 1D blood flow models for the cardiovascular system has significantly increased over time. In the last years, more complex networks and models have been constructed in terms of enhanced anatomical detail, first of all by considering a larger number of arteries. For example, the anatomically detailed arterial network (ADAN) model developed by Blanco et al.[3,14] is made of 2142 arteries, including 1598 arterial segments with a well-acknowledged name and 544 perforator arteries. In Reference 16, the authors assessed the impact of vascular anatomy definition degree in the predictions of blood flow models of the arterial network, by systematically comparing results obtained with the above mentioned ADAN model and those obtained with an anatomically simplified network containing the main 86 vessels. Furthermore, in Reference 17, the 1D ADAN network was coupled to cerebral arteriolar networks automatically generated using the constrained constructive optimization (CCO) technique. On the other hand, the incorporation of a 1D network for the venous circulation can contribute to the definition of more complex and detailed networks and models. A distinctive feature of the global, closed-loop, multiscale mathematical model for the human circulation developed by Müller and Toro in References 4 and 13 is the detailed description of the venous system, particularly for intracranial and extracranial veins, which accounts for fundamental mechanisms affecting cerebral venous hemodynamics. In Reference 15, Mynard and Smolich presented a model that accounts for wave propagation in anatomically realistic systemic (including coronary and cerebral) arterial/venous networks, pulmonary arterial/venous networks, and portal veins. In addition to the anatomically detailed description of arterial or venous networks, many other factors can contribute to the complexity of cardiovascular models and networks, such as the level at which biological mechanisms and mechanical characteristics of the cardiovascular system are modeled. For instance, when coupling the blood circulation to the cerebrospinal-fluid (CSF) and brain dynamics, these two systems have different temporal scales since CSF absorption/generation is slow compared to blood flow and, therefore, the time needed to reach periodic equilibrium of the solution is significant, thus strongly increasing the computational time and cost.[18] Control mechanisms, such as the baroreflex/chemoreflex controls and cerebral autoregulation, act over long time scales if compared with the cardiac cycle duration,[19-21] so then requiring long simulation times which impact on computational costs and efficiency. Including the viscoelastic properties of vessel walls into the 1D blood flow models, to define more realistic and physically consistent models, also demands a considerably higher computational cost for solving the corresponding PDE system, with respect to the purely elastic case.[22]

As a consequence, the 1D modeling of blood flow in such anatomically detailed and complex cardiovascular networks and models can result in computationally expensive simulations, even when exploiting parallel computing, which can further increase when long time scales are to be simulated. Several strategies and methodologies have been proposed and developed to address such challenges, either by working on faster and more efficient solvers for the 1D models, or by introducing 0D models coupled with or in place of the 1D models, to improve the computational efficiency and optimize the topological complexity of the vascular networks.

In the first framework, it is worth to mention the work of Müller et al.,[22] where the authors posed the need for accurate, robust and efficient numerical schemes to simulate 1D blood flow phenomena and able to produce results at a low computational cost. To address such issue, the authors proposed a high-order and robust fully local time-stepping (LTS) numerical scheme for 1D blood flow simulations in networks of elastic and viscoelastic vessels, and compared to a global time stepping (GTS) approach. When applying this to ADAN model, the GTS to LTS computational time ratios are 10.80 and 136.07, for the elastic and viscoelastic cases, respectively, demonstrating the benefits in terms of speed-up obtained by adopting an LTS over a GTS strategy.

In turn, several works concerning lumped-parameter/zero-dimensional models to simulate arterial blood flow are also found in the literature, to address the issues of computational efficiency and optimization of topological complexity. In Reference 23, a method to optimize the number of arterial segments included in 1D blood flow models and to find the model with the fewest number of necessary arteries for a given clinical application, by lumping distributed 1D segments into 0D Windkessel models, was presented. Similarly in Reference 24, in the context of patient-specific 1D blood

flow modeling, Epstein et al. investigated the effect of a reduction in the number of arterial segments in a given distributed 1D model on the shape of the simulated pressure and flow waveforms, by systematically lumping peripheral 1D model branches into Windkessel models. On the other hand, in Reference 25, the authors proposed a bond graph based lumped-parameter mathematical model, by fully preserving the topology of the original 1D network, to address the issue of execution time and the question of granularity in the context of modeling the cerebral circulation. Furthermore in Reference 26, a distributed lumped-parameter (DLP) modeling framework was proposed to efficiently compute blood flow and pressure in vascular domains at a computational cost that is orders of magnitude lower than that of computational fluid dynamics (CFD) simulations.

In this work, we propose an adaptive model selection approach to construct hybrid networks of 1D-0D vessels, which is based on appropriate *a-priori* model selection criteria, which are employed to convert 1D segments into the corresponding 0D counterparts. First of all, the family of nonlinear lumped-parameter models for blood flow presented in Reference 27 is considered, where these 0D models were derived in a way to preserve certain important nonlinear properties of the original 1D model. Then, equipped with both a 1D and 0D description of blood flow in vascular segments, we extend the coupling approach developed in References 28 and 29 for junctions of 1D vessels to appropriately couple 1D and 0D vessels through a hybrid coupling strategy. From a numerical point of view, in order to design accurate and efficient numerical schemes to solve networks of vessels, the high-order coupling between 1D vessels is achieved by considering the strategy presented in Müller and Blanco[30] and designing a simplified approach. Furthermore, as one of the main novelties of this work, we present and validate a methodology for the high-order hybrid numerical coupling of 1D and 0D vessels. The proposed numerical technique takes into account the interaction between 1D and 0D vessels and ensures that the desired accuracy of the solution in the 1D vessels is preserved and not affected by the coupling with 0D vessels. Finally, as a last necessary ingredient, we implement an adaptive model selection strategy to instantiate concrete hybrid networks. This methodology is based on relevant *a-priori* model selection criteria, defined in terms of geometrical and mechanical vessel properties or of flow distribution information. Given any generic vascular network, these model selection criteria are used to determine, *a-priori*, the most suitable model, either 1D or 0D, to adopt for each vessel. In particular, our aim is to identify those criteria providing the best trade-off between the computational cost of the simulations in the resulting hybrid networks and a good level of accuracy in the predicted results with respect to the reference, but computationally more expensive, 1D solution. The improvement in the computational efficiency must not come at the expense of a significant loss in terms of accuracy of the solution, pressure, and flow waveforms, in both 1D and 0D vessels, but a good balance between these two essential computational and modeling aspects is needed.

As briefly reviewed in the previous paragraph, several methods and approaches have been developed, which deal with 1D and 0D models to simulate blood flow in networks of vessels to address the issues of computational cost, execution time and optimization of topological complexity. However, here the proposed novel methodology presents some main essential aspects that were never found combined together in the above cited works. First, when constructing both 0D and hybrid network configurations, the topology and geometry of the original 1D network are preserved, so that blood flow and pressure distribution and waveforms can be reproduced and analyzed in each 1D/0D vessel of the original 1D network. Second, even if they are simpler than the 1D models, the adopted nonlinear 0D blood flow models preserve important nonlinear properties of the original 1D description, which strongly improve their ability to predict flow and pressure results in very good agreement with the reference 1D results, as demonstrated in Reference 27. Finally, the numerical coupling strategy designed to couple 1D and 0D vessels at junctions preserves the order of accuracy of the solution in 1D vessels. Furthermore, we point out that, to the best of our knowledge, a methodology to construct hybrid networks of 1D-0D vessels based on some model selection criteria and to simulate blood flow in such networks has never been reported before, in the open literature.

In this study, the different model selection criteria considered and tested are defined in terms of geometrical and mechanical vessel properties or of flow distribution information. As we will see throughout this work by applying the proposed strategy to different arterial networks of moderate complexity, the vessel compliance and intravascular volume will be identified as the most suitable model selection criteria to construct hybrid networks of vessels, providing the best trade-off between computational cost and accuracy. We consider this work as the first step towards a high-performance computational framework for the solution of highly complex networks. This methodology is expected to be significantly more effective when applied to much more complex networks and models where the heterogeneity of spatial and/or temporal scales is relevant, such as the ADAN model presented by Blanco et al.[3,14] and the global, closed-loop, multiscale model of the entire cardiovascular system developed by Müller and Toro.[4,13,18]

The rest of the article is structured as follows. In Section 2, we introduce the mathematical models used to describe both 1D and 0D blood flow in compliant vessels and the coupling equations defined for each type of junctions to couple

together 1D and/or 0D vessels. Afterwards, in Section 3, we present the numerical methods used in this work. First, the numerical schemes adopted to solve 1D and 0D blood flow models are reported; next, the high-order numerical coupling procedures proposed to solve the 1D, 0D and hybrid coupling of vessels are illustrated. To conclude the section, an adaptive model selection strategy to construct hybrid networks of vessels is devised. In Section 4, we perform a series of numerical experiments and discuss the obtained results. In particular, a set of convergence rate studies is first carried out and then, the proposed adaptive model selection strategy built upon several different *a-priori* model selection criteria is tested and applied to two arterial networks. The numerical experiments section is closed by presenting a quantitative study of a simple bifurcation model where 1D simulation results are compared against 3D results to validate the adopted 1D junction model and assess its ability to describe and reproduce flow splitting and wave propagation at junctions. We conclude with Section 5, where final considerations are made and future work is outlined.

2 | MATHEMATICAL MODELS

Most complete mathematical models for blood flow in compliant vessels consider coupled PDE systems describing fluid flow, wall mechanics, and their interaction. The overall methodology falls within the field of 3D-FSI models. However, due to their complexity and computational cost, at the present time, it is still unrealistic to think of deploying 3D-FSI models for very large vascular networks and cardiovascular models, or even for the full human vasculature. One-dimensional models derived from the cross-sectional averaging of full 3D models offer a reasonable alternative: they allow for simplified FSI simulations that describe the propagation of pressure and flow in large networks for a reduced computational cost. Indeed, in the last years, several studies have shown the ability of the 1D blood flow models to capture the main features of pressure, flow and area waveforms in large vessels, when compared to both 3D-FSI numerical data[31-34] and 3D-CFD results,[10,35-40] as well as to in vivo measurements[4,7,11-13,18] and in vitro experiments,[1,2,41] demonstrating that these models can be adopted to accurately simulate physiologically and clinically relevant problems at a reasonable computational cost. Hence, in the field of computational hemodynamics and mathematical modeling of the cardiovascular system, 1D models have been popular and widely used since the mid of the last century. The simplicity of 1D and 0D models over 3D models has facilitated their acceptance among researchers working in the field of blood flow modeling. Moreover, a strong argument in favor of this simplified modeling perspective is the more straightforward connection with measurable physiological signals and clinical variables. The main goal of the present work is to develop an efficient modeling and computational approach for large networks of vessels. We aim at combining the 1D model to a family of "cheaper" 0D models in a way to improve the computational efficiency of 1D-0D simulations, while still preserving a certain level of accuracy in the predicted results. Here we consider 1D models as the reference model and assess the predictive capability and ability of the proposed hybrid 1D-0D models to generate accurate results at a lower computational cost.

The mathematical model presented in this article includes both a one-dimensional and a zero-dimensional description of blood flow in compliant vessels, together with the coupling equations based on conservation principles that allow to arbitrarily couple 1D and 0D vessels in a network. First, in Sections 2.1 and 2.2, the one-dimensional model and the family of lumped-parameter models for blood flow are introduced. Afterwards, in Section 2.3, the proposed methodology to couple 1D and/or 0D vessels and to solve the different types of junctions is described.

2.1 | One-dimensional blood flow model

One-dimensional (1D) blood flow in elastic vessels is described by the following system of nonlinear, first-order hyperbolic equations

$$
\begin{cases}
\partial_t A + \partial_x q = 0, \\
\partial_t q + \partial_x \left(\alpha \dfrac{q^2}{A} \right) + \dfrac{A}{\rho} \partial_x p = f,
\end{cases}
\tag{1}
$$

where x is the axial coordinate of the vessel and $t > 0$ is time; $A(x, t)$ is the cross-sectional area of the vessel; $q(x, t)$ is the flow rate; $p(x, t)$ is the average internal pressure over a cross-section; α is a momentum correction factor, also called Coriolis coefficient, and $f(x, t) = -k_R \frac{q}{A}$ is the friction force per unit length of tube, where $k_R > 0$ is the viscous resistance

coefficient. Both parameters α and k_R depend on the assumed velocity profile. Here, an axisymmetric velocity profile is prescribed, from which the following definitions of α and k_R are obtained

$$\alpha = \frac{\zeta + 2}{\zeta + 1}, \quad k_R = 2(\zeta + 2)\pi\frac{\mu}{\rho}, \tag{2}$$

where ζ represents the velocity profile order, ρ and μ are the constant blood density and viscosity. The value $\zeta = 9$ defines a blunt velocity profile, while, for a Poiseuille flow, the parabolic velocity profile is obtained by setting $\zeta = 2$. For the Coriolis coefficient, the choice $\alpha = 1$, which indicates a perfectly flat velocity profile, is commonly used since it simplifies the analysis of the resulting 1D model.

To close system (1), pressure $p(x, t)$ is related to the cross-sectional area $A(x, t)$ and other vessel parameters by the following algebraic relation

$$p(x, t) - p_{ext}(x, t) = \psi(A(x, t); A_0, K, m, n, P_0), \tag{3}$$

with

$$\psi(A(x, t); A_0, K, m, n, P_0) = K\left[\left(\frac{A(x, t)}{A_0}\right)^m - \left(\frac{A(x, t)}{A_0}\right)^n\right] + P_0, \tag{4}$$

where $p_{ext}(x, t)$ is the external pressure acting on the vessel and P_0 is the reference pressure at which $A = A_0$. The above relation describes the elastic deformation of the vessel wall with variations of the transmural pressure, assuming that dissipative (viscous) effects are negligible. Pressure $p(x, t)$ also depends on parameters A_0, K, m, and n, which take into account geometrical and mechanical properties of the vessel. Normally, m and n are parameters derived from higher-order models or simply computed from experimental measurements. Typical values for arteries are $m = 0.5$ and $n = 0$, whereas for collapsible tubes, such as veins, it is assumed $m = 10$ and $n = -1.5$.

In particular, if we assume all these parameters to be independent of x and we consider arterial vessels, then $K > 0$ in (3) denotes the arterial stiffness and it is modeled as in References 42 and 43 by

$$K \equiv K_a = \frac{\sqrt{\pi}h_0 E}{(1 - v^2)\sqrt{A_0}}, \tag{5}$$

where h_0 is the vessel wall thickness, E is the Young's modulus and v is the Poisson ratio. To model incompressible vessel walls, we adopt $v = 0.5$.

We note that system (1) can be rewritten under the classical form of balance laws, that is

$$\partial_t \boldsymbol{Q} + \partial_x \boldsymbol{F}(\boldsymbol{Q}) = \boldsymbol{S}(\boldsymbol{Q}), \tag{6}$$

with $\boldsymbol{Q} = (A, q)^T$ the vector of conserved variables and

$$\boldsymbol{F}(\boldsymbol{Q}) = \begin{pmatrix} q \\ \alpha\dfrac{q^2}{A} + \dfrac{KA}{\rho}\left[\dfrac{m}{m+1}\left(\dfrac{A}{A_0}\right)^m - \dfrac{n}{n+1}\left(\dfrac{A}{A_0}\right)^n\right] \end{pmatrix}, \quad \boldsymbol{S}(\boldsymbol{Q}) = \begin{pmatrix} 0 \\ -k_R\dfrac{q}{A} \end{pmatrix}, \tag{7}$$

where $\boldsymbol{F}$ is the flux function and $\boldsymbol{S}$ is the source term. The same model can also be reformulated in quasi-linear form as

$$\partial_t \boldsymbol{Q} + \boldsymbol{A}(\boldsymbol{Q})\partial_x \boldsymbol{Q} = \boldsymbol{S}(\boldsymbol{Q}), \tag{8}$$

with coefficient matrix

$$\boldsymbol{A}(\boldsymbol{Q}) := \frac{\partial \boldsymbol{F}}{\partial \boldsymbol{Q}}. \tag{9}$$

Finally, we introduce here also the wave speed, denoted by c, as follows

$$c = \sqrt{\frac{A}{\rho}\frac{\partial p}{\partial A}}. \tag{10}$$

2.2 | Lumped-parameter blood flow models

Along with the 1D blood flow model described in Section 2.1, here we consider the family of nonlinear zero-dimensional (0D) or lumped-parameter models for blood flow in a compliant vessel derived in Reference 27. In this recent work, the traditional approach of deriving lumped-parameter models for blood flow in a single vessel[43-45] is extended, in order to preserve important nonlinear properties of the original 1D blood flow model (1). Such properties include the nonlinear pressure-area relation (3) and the pressure-dependent parameters characterizing the 0D models, such as the resistance R and the inductance L. Indeed, by including these nonlinearities, we obtain more realistic and physically consistent 0D models, representing a powerful tool to improve the computational efficiency of blood flow simulations, while still preserving and well reproducing the main features of pressure and flow waveforms in networks of vessels.

Given a vessel with $x \in [x_L, x_R]$ of length $l = |x_R - x_L|$, the system of ordinary differential equations (ODEs) governing the family of nonlinear lumped-parameter models is obtained by integrating in space the 1D equations in (1) over the interval $[x_L, x_R]$ and reads

$$\begin{cases} \dfrac{d}{dt}V(t) = Q_{\text{in}}(t) - Q_{\text{out}}(t), \\ L(\widehat{A})\dfrac{d}{dt}Q(t) = P_{\text{in}}(t) - R(\widehat{A})Q(t) - P_{\text{out}}(t). \end{cases} \tag{11}$$

The mean (volumetric) flow rate $Q(t)$ and the intravascular volume $V(t) := \widehat{A}(t)l$ represent the problem state variables, with $\widehat{A}(t)$ being the time-dependent average cross-sectional area of the vessel, that is

$$\widehat{A}(t) = \frac{1}{l}\int_{x_L}^{x_R} A(x,t)\, dx. \tag{12}$$

The ODE system (11) also involves input and output quantities,

$$Q_{\text{in}}(t) = q(x_L, t), \quad P_{\text{in}}(t) = p(x_L, t) \quad \text{and} \quad Q_{\text{out}}(t) = q(x_R, t), \quad P_{\text{out}}(t) = p(x_R, t),$$

respectively, which need to be defined together with initial conditions. The parameters characterizing the 0D model are the nonlinear resistance $R(\widehat{A})$ and inductance $L(\widehat{A})$, defined by

$$L(\widehat{A}) := \frac{\rho l}{\widehat{A}}, \quad R(\widehat{A}) := \frac{\rho k_R l}{\widehat{A}^2}. \tag{13}$$

These parameters are said to be *nonlinear* in the sense that they do no longer depend on a constant reference cross-sectional area A_0, but on the time-dependent average cross-section $\widehat{A}(t)$, which in turn, as we will see in the following, will depend on the mean pressure $P(t)$ acting on the vessel in a nonlinear way.

In the traditional approach of deriving 0D models, the model parameters are constant, namely $L_0 = L(A_0)$ and $R_0 = R(A_0)$, and pressure P is linearly related to volume V via the constant compliance C_0, that is

$$C_0 := l\left(\frac{\partial A}{\partial p}\right)\Big|_{A=A_0}. \tag{14}$$

In system (11), pressure P is directly computed from the average cross-sectional area $\widehat{A}$ via the nonlinear tube law (3), given by

$$\widehat{P}(t) - P_{ext}(t) = K\left[\left(\frac{\widehat{A}(t)}{A_0}\right)^m - \left(\frac{\widehat{A}(t)}{A_0}\right)^n\right] + P_0, \tag{15}$$
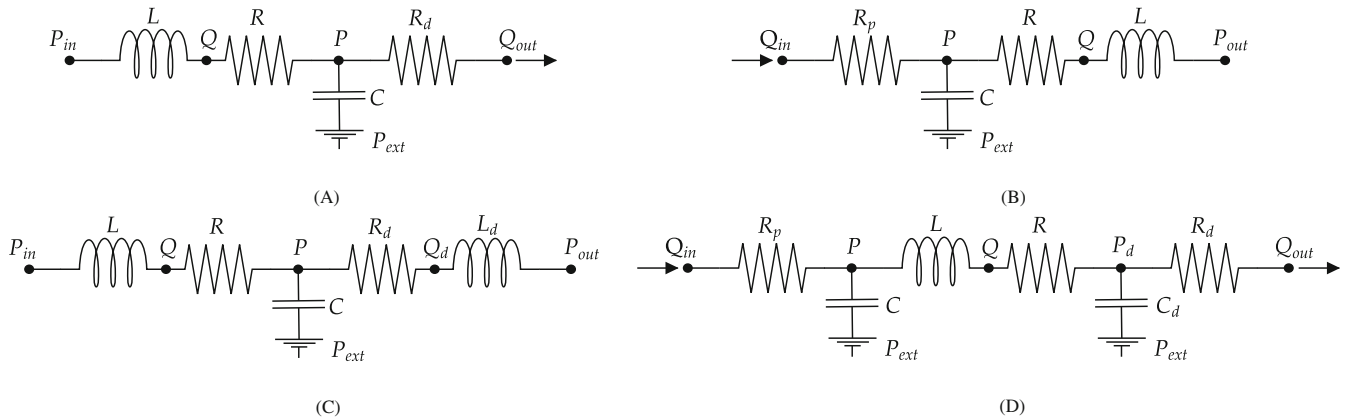
FIGURE 1 Representation of the four 0D vessel configurations, depending on the different assumptions about the data prescribed at the inlet and outlet of the segment. In the linear case, C is the constant vessel wall compliance, while, in the nonlinear case, C represents the mechanical properties of the vessel wall embedded in the nonlinear pressure-area relation (15). In both linear and nonlinear cases, R represents the resistance induced to the flow by the blood viscosity, while L is the inductance to flow, corresponding to the inertial term in the momentum balance equation. (A) (P_{in}, Q_{out})-type 0D vessel; (B) (Q_{in}, P_{out})-type 0D vessel; (C) (P_{in}, P_{out})-type 0D vessel; (D) (Q_{in}, Q_{out})-type 0D vessel

so that the nonlinearity of the original 1D pressure-area relation of the vessel is fully preserved also in this family of 0D models.

We also point out that in the momentum balance equation of system (11) the nonlinear convective terms have been neglected. For a discussion on the choice of neglecting the contribution of the convective terms in the 0D models, see Reference 27.

ODE system (11) defines a family of nonlinear 0D models. Indeed, four different 0D models are obtained depending on the different possible assumptions about the data prescribed at the inlet and outlet of the vessel. These models determine all the possible configurations of the same 0D vessel, which are the (P_{in}, Q_{out}), (Q_{in}, P_{out}), (P_{in}, P_{out}) and (Q_{in}, Q_{out})-type 0D vessels, displayed in Figure 1A, all of them describing flow and volume/pressure dynamics in a compliant vessel. The ODE systems governing the different 0D vessel configurations are given in Section S.1 of the Supporting Information, while for the full derivation and complete characterization of this family of nonlinear lumped-parameter models for blood flow the reader is referred to Reference 27.

We observe that a single vessel can be also represented by connecting in series two 0D vessels of the same type, either (P_{in}, Q_{out}) or (Q_{in}, P_{out}), to obtain a more accurate description of its dynamics. From now on, we will refer to these additional 0D vessel configurations as two-split (P_{in}, Q_{out})-type and two-split (Q_{in}, P_{out})-type 0D vessels.

2.3 | Coupling equations

Given a generic vascular network, each vessel can be modeled either as a 1D domain or as a 0D compartment. In the first case, its physics will be described by the 1D blood flow model (1). In the latter case, the vessel will be represented according to one of the four possible 0D vessel configurations presented in Section 2.2 and its dynamics will governed by the corresponding ODE system reported in Section S.1 of the Supporting Information. Our aim is to, departing from a network of vessels, allow for any possible combination of 1D and 0D vessels to be considered. In this way, hybrid network configurations can be constructed, including both 1D and 0D vessels, where three different types of junction/coupling can be found: 1D coupling, 0D coupling, and hybrid coupling. In this section, we illustrate the adopted coupling approach and derive the coupling equations that must be satisfied for each junction type. Indeed, a crucial aspect for constructing consistent networks of vessels is how to provide boundary conditions at terminal vertexes and algebraic coupling conditions between 1D and 0D domains at internal vertexes.

The coupling approach is based on conservation principles. Indeed, the coupling of two or more vessels at a junction must satisfy the following properties: (i) the conservation of mass, and (ii) the continuity of total pressure (or some approximation). Furthermore, only in the 1D and hybrid couplings, additional relations are obtained by imposing the continuity of the Riemann invariants in each 1D vessel.

2.3.1 | 1D coupling equations

If we have a junction J shared by N 1D vessels, a Riemann problem can be defined at the junction interface. Indeed, a junction between two or more 1D vessels defines a Riemann problem with discontinuous geometrical and mechanical vessel properties. In the case of subcritical flow, namely when $|u| < c$, this problem has been extensively studied and its exact solution has been derived in Toro and Siviglia[28] first and in Spilimbergo et al.[29] next. Also here, we will still restrict to this subcritical flow condition. The Riemann problem formulated for N 1D vessels sharing vertex J reads

$$\begin{cases} \partial_t \boldsymbol{Q}_k + \boldsymbol{A}(\boldsymbol{Q}_k)\partial_x \boldsymbol{Q}_k = 0, \\ \boldsymbol{Q}_k(x,0) = \boldsymbol{Q}_k^{1D}, \end{cases} \quad \text{for} \ \ k = 1, \ldots, N, \tag{16}$$

with $x \in [0, l_k]$, where we have dropped the vessel index k from the spatial coordinate x for the sake of simplicity in the notation.

Then, the self-similar solution to the Riemann problem (16) consists of $2N$ constant states, the N initial condition states $\boldsymbol{Q}_k^{1D} = \left(A_k^{1D}, q_k^{1D}\right)^T$, with $k = 1, \ldots, N$, provided by the 1D vessels, and the N unknown boundary states $\boldsymbol{Q}_k^* = \left(A_k^*, q_k^*\right)^T$, with $k = 1, \ldots, N$, to be determined, which will provide coupling conditions for each one of the vessels converging to the junction J. By following the approach proposed in References 28 and 29, we can construct the Riemann problem solution and compute these unknown boundary states.

First, under the assumption of adopting a two-rarefaction Riemann solver, which assumes, at each boundary, the head and tail waves traveling into the 1D domain to be rarefaction waves, the unknown boundary states $\boldsymbol{Q}_k^*$, with $k = 1, \ldots, N$, are connected to the initial condition states $\boldsymbol{Q}_k^{1D}$, with $k = 1, \ldots, N$, via the continuity of the generalized Riemann invariants, as follows

$$\frac{q_k^*}{A_k^*} - \frac{q_k^{1D}}{A_k^{1D}} + g_{1D}^k \int_{A_k^{1D}}^{A_k^*} \frac{c(\tau)}{\tau} d\tau = 0, \quad \text{for} \ \ k = 1, \ldots, N. \tag{17}$$

where g_{1D}^k is the auxiliary function

$$g_{1D}^k = \begin{cases} -1, & \text{if } x_J^k = 0, \\ 1, & \text{if } x_J^k = l_k, \end{cases} \tag{18}$$

and x_J^k is the local coordinate of the kth vessel, evaluated at vertex J. In this way, we obtain the first N nonlinear equations.

On the other hand, the state vectors $\boldsymbol{Q}_k^*$, with $k = 1, \ldots, N$, are connected among themselves via the linearly degenerate stationary contact discontinuity generated by the discontinuous variation of mechanical and geometrical properties of vessels converging at junction J. From the eigenstructure analysis of the coefficient matrix $\boldsymbol{A}$ of the continuous problem (8), we find the following wave relations associated to this stationary contact discontinuity

$$f_{MC}(q_1^*, \ldots, q_N^*) = \sum_{k=1}^{N} g_{1D}^k q_k^* = 0, \tag{19}$$

and

$$p_{tot,1}^* - p_{tot,k}^* = 0 \quad \Rightarrow \quad p(A_1^*) + \frac{1}{2}\rho\left(\frac{q_1^*}{A_1^*}\right)^2 - p(A_k^*) - \frac{1}{2}\rho\left(\frac{q_k^*}{A_k^*}\right)^2 = 0, \quad \text{for} \ \ k = 2, \ldots, N. \tag{20}$$

Equation (19) enforces mass conservation at the junction; the other $N - 1$ relations prescribe the continuity of total pressure p_{tot}^* between the vessels. In other words, the wave relations associated to the stationary contact discontinuity exactly coincide with those physically consistent conservation principles that we would expect to be satisfied at a junction. Full details on the derivation of wave relations in (19) and (20) are given in References 28 and 29.

In conclusion, we obtain a nonlinear system of $2N$ equations in $2N$ unknowns that can be numerically solved to compute the sought boundary states $\boldsymbol{Q}_k^*$, with $k = 1, \dots, N$.

2.3.2 | 0D coupling equations

To couple 0D vessels at a junction, we extend the coupling procedure presented in Reference 27, where the 0D coupling must satisfy the conservation of flow and also imposes a common pressure on all branches, to ensure the continuity of pressure at the junction. By enforcing pressure continuity only, instead of total pressure continuity as in the 1D coupling, the problem to be solved at the junction is linear. However, in order to arrange compatible 0D vessel types into a network, with inlets and outlets coupled appropriately, restrictions on admissible 0D vessel configurations are necessary for vessels converging at the junction.

Here, we extend this approach in order to find appropriate coupling conditions between 0D vessels that do not require any restrictions on the admissible 0D vessel types converging at a junction, but still ensuring the linearity of the coupling problem to be solved. Otherwise, solving a 0D coupling problem would become as computationally expensive as solving a 1D nonlinear coupling problem.

Suppose to have a junction connecting an arbitrary number M of 0D vessels, sharing their inlets or outlets at the junction point. Then, the input and output quantities to be prescribed at the inlets and outlets of these vessels, P_{in}/Q_{in} and P_{out}/Q_{out}, respectively, depending on the configuration of each vessel, need to be determined in a way to ensure mass conservation and continuity of total pressure. This is done by prescribing to all inlets and outlets converging at the junction a common pressure P^*, which represents an approximation of the total pressure P_{tot}^* and is computed by enforcing the conservation of mass, that is

$$f_{MC}(P^*) = \sum_{j=1}^{M} g_{0D}^j Q_j^* = 0, \tag{21}$$

where g_{0D}^j is the auxiliary function similar to the one defined in the 1D coupling problem

$$g_{0D}^j = \begin{cases} -1, & \text{if } v^j \text{ shares its inlet,} \\ 1, & \text{if } v^j \text{ shares its outlet,} \end{cases} \tag{22}$$

and

$$Q_j^* = \begin{cases} Q^j, & \text{if } v^j \text{ shares its inlet/outlet of } P\text{-type,} \\ Q_{in}^j(P^*) = \dfrac{P^* - P^j}{R_p^j}, & \text{if } v^j \text{ shares its inlet of } Q\text{-type,} \\ Q_{out}^j(P^*) = \dfrac{P^j - P^*}{R_d^j}, & \text{if } v^j \text{ shares its outlet of } Q\text{-type,} \end{cases} \tag{23}$$

for $j = 1, \dots, M$. Note that the flow rates Q_j^* leaving or entering each 0D vessel can be either known (and given by the state variable Q of the corresponding ODE system), or unknown and defined in terms of the pressure P^* (as pressure difference over the vessel resistance), depending on the 0D vessel configuration.

The function f_{MC} in (21) is linear in the pressure unknown P^* and, once the value of P^* has been computed, in the jth 0D vessel v^j we prescribe either a condition on the pressure, that is $P_{in}^j = P^*$ or $P_{out}^j = P^*$, or a condition on the flow rate, that is $Q_{in}^j(P^*)$ or $Q_{out}^j(P^*)$ given by the relations in (23), depending on the 0D vessel configuration.

Remark 1. We point out that, in the proposed 0D linear coupling procedure, only one configuration is not admitted, that is the one where all the inlets and outlets of the 0D vessels converging at the junction are of pressure type (P-type). Indeed, in this case, it is easy to see that in the mass conservation function f_{MC} defined in (21) only known quantities occur, that are the flow rates $Q^j, j = 1, \dots, M$, across the 0D vessels, and thus, there is no dependency on the common pressure P^*. As a consequence, both mass conservation and continuity of total pressure would be lost in this configuration.

2.3.3 | Hybrid coupling equations

The most general coupling of vessels at junctions is the one where both 1D and 0D vessels are coupled together. However, a hybrid coupling approach that ensures mass conservation and continuity of total pressure can be easily obtained by appropriately merging the 1D and 0D coupling procedures described in Sections 2.3.1 and 2.3.2, respectively.

Suppose to have a junction connecting N 1D vessels and M 0D vessels. For each 1D vessel, we have to compute the unknown state vector $Q_k^* = (A_k^*, q_k^*)$, with $k = 1, \ldots, N$, whereas for each 0D vessel the input/output quantity to be prescribed at its inlet/outlet, that is P_{in}^j / Q_{in}^j or P_{out}^j / Q_{out}^j, with $j = 1, \ldots, M$, has to be determined.

The hybrid coupling problem is governed by the following nonlinear system

$$
\begin{cases}
f_{MC}(q_1^*, \ldots, q_N^*, p_{tot}^*) = \sum_{k=1}^{N} g_{1D}^k q_k^* + \sum_{j=1}^{M} g_{0D}^j Q_j^* = 0, \\[2mm]
Q_j^* = \begin{cases}
Q^j, & \text{if } v^j \text{ shares its inlet/outlet of } P\text{-type}, \\[2mm]
Q_{in}^j(p_{tot}^*) = \dfrac{p_{tot}^* - P^j}{R_p^j}, & \text{if } v^j \text{ shares its inlet of } Q\text{-type}, \\[2mm]
Q_{out}^j(p_{tot}^*) = \dfrac{P^j - p_{tot}^*}{R_d^j}, & \text{if } v^j \text{ shares its outlet of } Q\text{-type},
\end{cases} & \text{for } j = 2, \ldots, M, \\[6mm]
p(A_1^*) + \dfrac{1}{2}\rho\left(\dfrac{q_1^*}{A_1^*}\right)^2 - p(A_k^*) - \dfrac{1}{2}\rho\left(\dfrac{q_k^*}{A_k^*}\right)^2 = 0, & \text{for } k = 2, \ldots, N, \\[4mm]
\dfrac{q_k^*}{A_k^*} - \dfrac{q_k^{1D}}{A_k^{1D}} + g_{1D}^k \displaystyle\int_{A_k^{1D}}^{A_k^*} \dfrac{c(\tau)}{\tau} d\tau = 0, & \text{for } k = 1, \ldots, N.
\end{cases}
\tag{24}
$$

The first relation in system (24) enforces mass conservation at the junction, taking into account the contribution of all vessels, both 1D and 0D. In particular, the 0D flow rates Q_j^*, with $j = 1, \ldots, M$, entering or leaving the 0D vessels converging at the junction, are defined in the same way as in (23) for the 0D coupling, with the only difference here that the approximate pressure P^* has now been replaced by the exact value of the total pressure p_{tot}^*, to be determined. Hence, the remaining equations in system (24) prescribe the continuity of the total pressure p_{tot}^* between the 1D vessels and the constancy of the generalized Riemann invariants in each 1D vessel. The idea is that we can still define and solve a Riemann problem at the junction interface between the 1D vessels, but when constructing its solution the presence of 0D vessels and their contribution to the flow balance through the junction have to be taken into account, as expressed in system (24).

System (24) includes $2N$ nonlinear equations in $2N$ unknowns, that are $A_1^*, \ldots, A_N^*$ and $q_1^*, \ldots, q_N^*$. By solving numerically this algebraic problem, we obtain the 1D boundary states Q_k^*, for $k = 1, \ldots, N$, and thus the common total pressure p_{tot}^*. The computed value of p_{tot}^* is then used to enforce in each 0D vessel either a condition on the pressure, that is $P_{in}^j = p_{tot}^*$ or $P_{out}^j = p_{tot}^*$, or a condition on the flow rate, that is $Q_{in}^j(p_{tot}^*)$ or $Q_{out}^j(p_{tot}^*)$ as defined in (24), for $j = 1, \ldots, M$, depending on each 0D vessel configuration.

3 | NUMERICAL METHODS

In this section, we present the numerical methods adopted to solve the 1D and 0D blood flow models (Sections 3.1 and 3.2, respectively) and we describe in detail the numerical treatment of the different types of coupling connecting 1D and 0D vessels into a network (Section 3.3). In particular, when using high-order numerical schemes to approximate the solutions of the 1D blood flow model (1) and of the lumped-parameter models (11), high-order coupling procedures are also needed in order to preserve the space and time accuracy of the original schemes over the entire network. The numerical strategy to address this crucial aspect will be addressed in Section 3.3 for the 1D, 0D and hybrid couplings.

Finally, in Section 3.4, we develop an adaptive model selection approach based on *a-priori* model selection criteria to construct hybrid networks of 1D-0D vessels. Our aim is to find relevant criteria, based on vessel geometrical and mechanical properties or on flow distribution information, that enable us to choose the most suitable model to be used for each vessel of a network, ensuring the correct trade-off between the accuracy of the predicted results and the computational cost of the simulations, with respect to the 1D network.

3.1 │ Numerical scheme for the 1D blood flow model

System (1) is discretized using a second-order MUSCL-Hancock (MH) numerical scheme,[46] with ENO (essentially non-oscillatory) reconstruction[47,48] and numerical source computed following the ADER approach.[49] Since the original MUSCL-Hancock scheme was first formulated to deal only with conservation laws without source terms, the MUSCL-Hancock procedure was then extended to take into account also source terms via the ADER approach based on solution of the generalized Riemann problem (GRP), formulated as in Reference 50.

We adopt a finite volume method of the form

$$Q_i^{n+1} = Q_i^n - \frac{\Delta t^n}{\Delta x} \left[F_{i+\frac{1}{2}} - F_{i-\frac{1}{2}} \right] + \Delta t^n S_i, \tag{25}$$

for $i = 1, \dots, \overline{M}$, where $\overline{M}$ is the number of computational cells discretizing the one-dimensional space domain $[0, l]$; $\Delta x = x_{i+\frac{1}{2}} - x_{i-\frac{1}{2}}$ is the constant mesh spacing, where each cell $I_i = \left(x_{i-\frac{1}{2}}, x_{i+\frac{1}{2}} \right)$ has center located in x_i, with $x_{i\pm\frac{1}{2}} = x_i \pm \frac{\Delta x}{2}$; $\Delta t^n = t^{n+1} - t^n$ is the time step discretizing the time domain $[0, t_{end}]$ and constrained by the usual Courant–Friedrichs–Lewy (CFL) stability condition. Finite volume schemes of the form (25) are obtained by integrating the equations of system (6) on the control volume $V = \left[x_{i-\frac{1}{2}}, x_{i+\frac{1}{2}} \right] \times [t_n, t_{n+1}]$ and by introducing suitable approximations of the integral averages.

In the framework of Godunov-type schemes, the MUSCL-Hancock approach achieves second-order accuracy in space and time by computing the intercell flux $F_{i+\frac{1}{2}}$ according to the following three steps:

(I) Data reconstruction and cell boundary values: based on the set of cell averages $\{Q_i^n\}$, we obtain a first-degree reconstruction polynomial vector $\boldsymbol{\Phi}_i(x)$ for each cell I_i by finding a linear polynomial $\varphi_{l,i}(x)$ for each component of the vector of conserved variables, that is

$$\varphi_{l,i}(x) = w_{l,i}^n + (x - x_i)\Delta_{l,i}, \quad \text{for } l = 1, 2, \tag{26}$$

where $w_{l,i}^n$ is the lth component of vector Q_i^n and $\Delta_{l,i}$ is the associated slope of its reconstruction polynomial $\varphi_{l,i}(x)$. Here, the slopes $\Delta_{l,i}$ for all components $w_{l,i}^n$ are computed by using the ENO criterion to preserve conservation and non-oscillatory properties. The boundary extrapolated values are then computed as follows

$$Q_i^L = \boldsymbol{\Phi}_i(x_{i-\frac{1}{2}}), \quad Q_i^R = \boldsymbol{\Phi}_i(x_{i+\frac{1}{2}}). \tag{27}$$

(II) Evolution of boundary extrapolated values by a time $\frac{\Delta t^n}{2}$ accounting for source term

$$\begin{cases} \overline{Q}_i^L = Q_i^L - \frac{1}{2}\frac{\Delta t^n}{\Delta x} \left[F(Q_i^R) - F(Q_i^L) \right] + \frac{\Delta t^n}{2} S(Q_i^L), \\ \overline{Q}_i^R = Q_i^R - \frac{1}{2}\frac{\Delta t^n}{\Delta x} \left[F(Q_i^R) - F(Q_i^L) \right] + \frac{\Delta t^n}{2} S(Q_i^R). \end{cases} \tag{28}$$

(III) Solution of a classical Riemann problem with piecewise constant data $\left(\overline{Q}_i^R, \overline{Q}_{i+1}^L \right)$ to obtain the similarity solution $Q_{i+\frac{1}{2}}\left(\frac{x}{t} \right)$ and compute the intercell flux as

$$F_{i+\frac{1}{2}} = F\left(Q_{i+\frac{1}{2}}(0) \right), \tag{29}$$

where $Q_{i+\frac{1}{2}}(0)$ denotes the value of $Q_{i+\frac{1}{2}}\left(\frac{x}{t} \right)$ at $\frac{x}{t} = 0$. Any approximate Riemann solver can be used to solve the Riemann problem. In this work, we adopt the HLL approximate Riemann solver.[51,52]

Finally, to compute the numerical source we proceed by following the ADER approach[49] and we set

$$S_i = S\left(Q_i^n + \frac{\Delta t^n}{2} \left[-A(Q_i^n)\Delta_i + S(Q_i^n) \right] \right), \tag{30}$$

which is obtained by approximating the volume-integral average of the source term $S(Q(x, t))$ by using the midpoint rule in space and time, where the midpoint value $Q\left(x_i, \frac{\Delta t^n}{2}\right)$ is computed by performing a Taylor expansion in time and applying the Cauchy–Kowalevski method at point x_i.

The number of computational cells for a 1D vessel is given by

$$\overline{M} = \max\left\{\lceil \frac{l}{\Delta x_{\max}} \rceil, 2\right\}, \tag{31}$$

where l is the vessel length.

3.2 | Numerical scheme for zero-dimensional blood flow

Each 0D vessel configuration describing blood flow in a 0D vascular segment is governed by a system of first-order, nonlinear ODEs obtained from (11), which can be rewritten in compact form as

$$\frac{d}{dt}Y_j(t) = F_j(t, Y_j(t), Y_j^D(t)), \quad Y_j(0) = Y_j^0, \tag{32}$$

where $Y_j(t)$ is the state variable vector of vessel v^j and Y_j^0 is the initial condition vector. The nonlinear vector function F_j on the right-hand side of the system depends on $Y_j(t)$ directly and on the vector $Y_j^D(t)$ of the *prescribed data* at the inlet and outlet of the jth vessel. These *prescribed data* may include coupling conditions at internal junctions, coupling conditions to either single-resistance or *RCR* Windkessel elements for terminal vessels, and also external sources $f_{ext}(t)$ to the vessel, such as a prescribed inflow at the inlet of the aorta. In particular, if a 0D vessel shares its inlet and/or outlet at junctions, then the vector $Y_j^D(t)$ will be defined also by the state of its adjacent vessels, according to the different coupling approaches introduced in Section 2.3. For each 0D vessel, the corresponding ODE system of the form (32) is solved using the well-established four-step explicit fourth-order Runge–Kutta (RK4) method with appropriate time step to guarantee the stability of the scheme and the mesh independence of the solution.

3.3 | High-order numerical couplings

In general, given a generic hybrid network of vessels, where 1D and 0D vessels are coupled via the 1D, 0D, and hybrid coupling strategies, all vessels will be evolved by using the same global time step Δt^n, given by

$$\Delta t^n = \min_{k=1,\dots,N_{tot}} \Delta t_k^{n,CFL}, \tag{33}$$

for $n \geq 0$, where N_{tot} is the total number of 1D vessels of the network and $\Delta t_k^{n,CFL}$ is the time step corresponding to the kth 1D vessel at the time level n, computed according to the CFL stability condition. This choice of the global time step Δt^n (33) clearly ensures the stability of the adopted numerical method in all 1D vessels. However, on the other hand, this time step may not be sufficiently small to guarantee also the stability of the explicit numerical scheme used to solve the ODE systems corresponding to the 0D vessels of the network. If that is the case, the global time stepping procedure can be replaced by a local time stepping (LTS) technique, so that 1D and 0D vessels are evolved with two different time steps, Δt^n and Δt^{m_n}, respectively, each one ensuring the stability of the corresponding numerical method. Given the 1D time step Δt^n computed as in formula (33), we define a 0D local time step Δt^{m_n} by dividing the time step Δt^n in a finite number n_{step} of subintervals, as

$$\Delta t^{m_n} = \frac{\Delta t^n}{n_{step}}, \tag{34}$$

where the subscript n to the index m in Δt^{m_n} emphasizes that the 0D time step Δt^m clearly depends on the 1D time step Δt^n at the time level n. In this way, 0D vessels will evolve with reduced local time step Δt^{m_n} from time t^m to time $t^{m+1} = t^m + \Delta t^{m_n}$, $m \geq 0$, while 1D vessels will evolved with time step Δt^n from time t^n to time $t^{n+1} = t^n + \Delta t^n$, $n \geq 0$,

only when $t^{n+1} \equiv t^{m+1}$, that is when the 1D and 0D time levels are synchronized. For full details on the LTS methodology see Reference 22. We also emphasize that the choice of the number of subintervals n_{step} may depend on the specific problem and the network characteristics.

A very important aspect to be addressed is that we want the orders of accuracy of the numerical schemes adopted to solve the 1D and 0D models for a single vessel to be achieved also by the different coupling procedures, at the level of junctions, in order to globally preserve the desired accuracy of the solutions. In the following of this section, we will describe the different methodologies adopted to achieve high-order numerical coupling for the different types of junctions.

3.3.1 | 1D coupling

Let us first consider the 1D coupling approach presented is Section 2.3.1 to join an arbitrary number of 1D vessels. In the simplest case, the initial condition states Q_k^{1D}, with $k = 1, \ldots, N$, provided by the 1D vessels to the Riemann problem (16), are given by the first-order cell-averaged solutions $\left\{ Q_{k,i}^n \right\}$, with either $i = 1$ if $x_J^k = 0$, namely if the kth vessel shares its left vertex with the junction, or $i = \overline{M}_k$ if $x_J^k = l_k$, that is if the kth vessel shares its right vertex with the junction, where $\overline{M}_k$ is the number of computational cells of the kth vessel, for $k = 1, \ldots, N$. However, the resulting numerical coupling strategy to compute the unknown boundary states Q_k^*, with $k = 1, \ldots, N$, and evolve the solution from time t^n to time $t^{n+1} = t^n + \Delta t^n$ is clearly first-order accurate in space and time.

In general, high-order numerical coupling between 1D vessels can be achieved by following, for instance, the methodology presented in Müller and Blanco[30] or the approach introduced in Borsche and Kall.[53] Here, to obtain a 1D numerical coupling strategy that is second-order accurate in space and time, we adopt a simplified approach, as follows. In the RP defined at the junction interface, it is sufficient to replace the cell-averaged values by the evolved boundary extrapolated values defined in step (II) of MUSCL-Hancock scheme, that is

$$Q_k^{1D} = \begin{cases} \overline{Q}_{k,1}^{L,n}, & \text{if } x_J^k = 0, \\ \overline{Q}_{k,\overline{M}_k}^{R,n}, & \text{if } x_J^k = l_k. \end{cases} \tag{35}$$

In particular, if the kth vessel shares its left vertex with the junction, that is $x_J^k = 0$, then we will consider the left evolved boundary extrapolated value in the first computational cell $\overline{Q}_{k,1}^{L,n}$; whereas, if the vessel shares its right vertex with the junction, namely $x_J^k = l_k$, in this case the initial condition state Q_k^{1D} will be given by the right evolved boundary extrapolated value in the last computational cell $\overline{Q}_{k,\overline{M}_k}^{R,n}$ of the vessel 1D domain.

Equipped with these initial condition states, the Riemann problem can be solved as illustrated in Section 2.3.1 to obtain the unknown boundary states Q_k^*, with $k = 1, \ldots, N$. By adopting the midpoint integration rule to approximate the time integral of the interface flux, the computed boundary state vectors are finally used to evaluate the boundary numerical fluxes in the finite volume formula (25) for the 1D vessels converging at the junction

$$\left. \begin{aligned} \text{if } x_J^k = 0, \qquad & F_{\frac{1}{2}}^k = \frac{1}{\Delta t^n} \int_{t^n}^{t^{n+1}} F\left(Q(x_{\frac{1}{2}}, t) \right) dt \\ \text{if } x_J^k = l_k, \qquad & F_{\overline{M}_k + \frac{1}{2}}^k = \frac{1}{\Delta t^n} \int_{t^n}^{t^{n+1}} F\left(Q(x_{\overline{M}_k + \frac{1}{2}}, t) \right) dt \end{aligned} \right\} \approx F_k^* \equiv F(Q_k^*), \tag{36}$$

for $k = 1, \ldots, N$.

3.3.2 | 0D coupling

In the case of 0D coupling, it is straightforward to preserve the fourth-order accuracy in time of the RK4 method also at the level of junctions, in the 0D coupling procedure.

The RK4 scheme, adopted to solve the ODE systems associated to the different 0D vessel configurations and reported in the Supporting Information, is a four-step method. The approximate solution at the next time level $t^{m+1} = t^m + \Delta t^m$ is obtained by summing to the approximate solution at the present time level t^m the product between the weighted average of four increments, $K_1, \ldots, K_4$, and the size of the time interval Δt^m.

Given a junction connecting M 0D vessels, even if each 0D vessel is evolved separately according to the corresponding ODE system governing its dynamics, these vessels are not isolated, but are interacting with each other via the coupling conditions (pressures/flow rates) prescribed at their inlets and outlets converging at the junction. As a consequence, to evolve from time t^m to time t^{m+1} the solution in each 0D vessel according to RK4 method (S.8), the coupling conditions between these vessels must be updated at each of the four intermediate steps of the scheme, namely the 0D coupling problem must be solved at each RK4 intermediate step. This is clear also from the RK4 method's formulae (S.8), where each of the four increments, K_s, $s = 1, \ldots, 4$, is computed by using the intermediate updated RK4 solution and prescribed data, contained in vector $\boldsymbol{Y}^D$, corresponding to each intermediate step. The outline of the algorithm is given in Section S.2 of the Supporting Information.

3.3.3 | Hybrid coupling

We deal now with the last type of coupling, the hybrid coupling between 1D and 0D vessels. In particular, 1D vessels are evolved using the second-order MUSCL-Hancock scheme and 0D vessels are solved adopting the explicit RK4 method, either with a global time step Δt^n or with two different local time steps, Δt^n for the 1D vessels and Δt^{m_n} for the 0D vessels, as explained at the beginning of this section. Here, we propose a numerical strategy that allows to achieve high-order hybrid coupling, to preserve second-order accuracy in space and time in the 1D vessels and the second-order accuracy in time in the 0D vessels.

Let us start from the case of global time step. Suppose to have a junction joining together N 1D vessels and M 0D vessels, and that all these vessels are evolved with the same global time step Δt^n computed as in (33). To evolve the solution in all vessels from time t^n to time $t^{n+1} = t^n + \Delta t^n$, the 1D-0D coupling conditions must be updated at each one of the four intermediate steps of RK4 method (S.8). To be precise, at step s of RK4 scheme, $s = 1, \ldots, 4$, the junction is solved via the hybrid coupling approach proposed in Section 2.3.3 by considering:

- in the 0D vessels, the RK4 intermediate solution obtained at step s of the method to compute the increment K_s, in the same way as illustrated in Section 3.3.2 for 0D coupling;
- in the 1D vessels, the MUSCL boundary extrapolated values $\boldsymbol{Q}_{k,1}^{L,n}/\boldsymbol{Q}_{k,\overline{M}_k}^{R,n}$, with $k = 1, \ldots, N$, evolved by a fraction of the time step Δt^n equal to that used at the intermediate step s of RK4 method, that is

$$
\begin{cases}
\overline{\boldsymbol{Q}}_{k,1}^{L,n+H_s} = \boldsymbol{Q}_{k,1}^{L,n} - \dfrac{H_s \Delta t^n}{\Delta x_k}\left[\boldsymbol{F}(\boldsymbol{Q}_{k,1}^{R,n}) - \boldsymbol{F}(\boldsymbol{Q}_{k,1}^{L,n})\right] + H_s \Delta t^n \boldsymbol{S}(\boldsymbol{Q}_{k,1}^{L,n}), & \text{if } x_J^k = 0, \\[2ex]
\overline{\boldsymbol{Q}}_{k,\overline{M}_k}^{R,n+H_s} = \boldsymbol{Q}_{k,\overline{M}_k}^{R,n} - \dfrac{H_s \Delta t^n}{\Delta x_k}\left[\boldsymbol{F}(\boldsymbol{Q}_{k,\overline{M}_k}^{R,n}) - \boldsymbol{F}(\boldsymbol{Q}_{k,\overline{M}_k}^{L,n})\right] + H_s \Delta t^n \boldsymbol{S}(\boldsymbol{Q}_{k,\overline{M}_k}^{R,n}), & \text{if } x_J^k = l_k,
\end{cases}
\tag{37}
$$

for $s = 1, \ldots, 4$ and $k = 1, \ldots, N$. $H = \left\{0, \frac{1}{2}, \frac{1}{2}, 1\right\}$ is the vector containing the time step fractions to be used to evolve the 1D boundary extrapolated values in the four RK4 intermediate steps. In particular, at step $s = 1$ of RK4 method, we have no evolution of the MUSCL reconstructed variables, at steps $s = 2, 3$ of the scheme the boundary extrapolated values are evolved by a half Δt^n, and at step $s = 4$ we will have the evolution of a complete time step Δt^n.

Then, by solving the hybrid coupling problem, at each step of RK4 method we get:

- the 0D coupling conditions $P_{\text{in/out}}^{j,s}/Q_{\text{in/out}}^{j,s}$, for $j = 1, \ldots, M$, namely pressures and flow rates to be prescribed at the inlets and outlets of the 0D vessels;
- the 1D boundary state vectors $\boldsymbol{Q}_k^{*,s}$, for $k = 1, \ldots, N$, for the 1D vessels.

Once the four intermediate steps of RK4 method are completed, 0D vessels are simply evolved according to RK4 formulae. On the other hand, in each 1D vessel, the time integral of the boundary flux, needed to evolve the 1D solution from time t^n to time t^{n+1} according to the finite volume formula (25), is approximated using a quadrature formula with nodes over the interval $[t^n, t^{n+1}]$ given by the four times corresponding to the four steps of RK4 and the same weights of

the four RK4 increments, as follows

$$
\begin{cases}
\text{nodes:} & \{t_s = t^n + H_s \Delta t^n\}_{s=1,\dots,4}, \\
\text{weights:} & \{\omega_s\}_{s=1,\dots,4},
\end{cases}
\tag{38}
$$

to get

$$
\left.
\begin{aligned}
\text{if } x_J^k = 0, \quad & \boldsymbol{F}_{\frac{1}{2}}^k = \frac{1}{\Delta t^n} \int_{t^n}^{t^{n+1}} \boldsymbol{F}\left(\boldsymbol{Q}(x_{\frac{1}{2}}, t)\right) dt \\
\text{if } x_J^k = l_k, \quad & \boldsymbol{F}_{\overline{M}_k+\frac{1}{2}}^k = \frac{1}{\Delta t^n} \int_{t^n}^{t^{n+1}} \boldsymbol{F}\left(\boldsymbol{Q}(x_{\overline{M}_k+\frac{1}{2}}, t)\right) dt
\end{aligned}
\right\} \approx \sum_{s=1}^{4} \omega_s \boldsymbol{F}\left(\boldsymbol{Q}_k^{*,s}\right),
\tag{39}
$$

for $k = 1, \dots, N$.

With this methodology, we take into account the interaction between 1D and 0D vessels at each intermediate step of RK4 method and we achieve the second-order accuracy of the coupling.

Remark 2. It is clear that adopting the four-step RK4 method to solve the ODE systems governing blood flow in the 0D vessels and the proposed numerical hybrid coupling strategy requires that, at each time step, the hybrid coupling problem must be solved four times at each junction of 1D-0D vessels to preserve the desired second-order accuracy in the solution. Since in the 1D domain we use a second-order accurate numerical scheme, it would be reasonable to employ a second-order method also for the 0D domain, so that each time step would demand to solve the hybrid coupling just two times, thus reducing the computational effort and time of the simulations. However, our choice of using the fourth-order Runge–Kutta scheme is justified by the fact that this method has better stability properties than other possible second-order, explicit numerical schemes for ODE systems. Indeed, as we will see in Section 4 devoted to numerical experiments, when using a sufficiently fine 1D mesh size, the 1D time step obtained according to the CFL condition can be used for both 1D and 0D vessels as global time step, also ensuring the stability of RK4 method and the accuracy of the predicted 0D results. On the other hand, numerical experiments (not reported here) have shown that second-order, explicit schemes, like Heun's method and the midpoint method, are not as stable as the RK4 scheme, thus requiring a significantly smaller time step than the 1D time step computed via the CFL condition. In this case, a "local time stepping procedure", as the one described at the beginning of Section 3.3, could be implemented, but, because of the very small 0D time step, the number of times to solve the hybrid coupling would increase even more in order to synchronize 1D and 0D vessels converging at the same junction.

The proposed strategy can be easily extended also to the case of local time steps Δt^n for 1D vessels, defined as in (33), and Δt^{m_n} for 0D vessels, computed as in (34). From the definitions of these local time steps, we clearly have $\Delta t^n = n_{step} \Delta t^{m_n}$. Hence, starting from time t^n, the numerical procedure illustrated above is performed over each time interval of the form $[t^n + (r-1)\Delta t^{m_n}, t^n + r\Delta t^{m_n}]$, for $r = 1, \dots, n_{step}$, to update the solution in the 0D vessels and to compute the 1D boundary vector states $\left\{\boldsymbol{Q}_k^{*,rs}\right\}_{s=1,\dots,4}$, for $r = 1, \dots, n_{step}$ and $k = 1, \dots, N$. Then, the boundary numerical fluxes in the 1D vessels are obtained by approximating the time integral of the interface flux over the entire interval $[t^n, t^{n+1}]$, with $t^{n+1} = t^n + \Delta t^n = t^n + n_{step}\Delta t^{m_n}$, as

$$
\boldsymbol{F}_{\frac{1}{2}}^k \text{ or } \boldsymbol{F}_{\overline{M}_k+\frac{1}{2}}^k \approx \frac{1}{n_{step}} \sum_{r=1}^{n_{step}} \sum_{s=1}^{4} \omega_s \boldsymbol{F}\left(\boldsymbol{Q}_k^{*,rs}\right),
\tag{40}
$$

for $k = 1, \dots, N$. These boundary flux vectors are finally used to evolve the solution in the 1D vessels from time t^n to time t^{n+1} according to the finite volume formula (25).

3.4 | Adaptivity and *a-priori* model selection criteria

At this point, equipped with both 1D and 0D blood flow models and with suitable numerical coupling strategies, we need an effective methodology to construct hybrid networks of vessels. In particular, we want to identify relevant *a-priori* model selection criteria that, given any network of vessels of which geometrical and mechanical properties are known, allow us to determine the most suitable model, either 1D or 0D, to be used for each vessel of the network.

One of the main goals of the present work is to address the issues of computational cost and efficiency related to the modeling and simulation of blood flow in highly complex networks. Therefore, we look for model selection criteria able to provide the best trade-off between (i) computational cost of the simulations in the resulting hybrid networks, and (ii) accuracy in the predicted results with respect to the reference, computationally expensive 1D results. The starting point is a 1D network, namely a network where all vessels are represented as coupled 1D domains. Then, we explore different model selection criteria to be used to determine the vessels that can be turned into 0D models. The analysis carried out allows us to identify those parameters that generate hybrid network configurations where, on the one hand, the computational cost of the simulations is strongly reduced and, on the other hand, pressure and flow waveforms are reproduced with a good level of accuracy throughout the entire network.

We have proposed and tested the following *a-priori* model selection criteria: vessel length l; vessel radius r_0; intravascular volume $V_0 = (\pi r_0^2)l$; vessel compliance $C_0 := l\left(\frac{\partial A}{\partial p}\right)\Big|_{A=A_0}$; mean flow rate $\overline{Q}$ through the vessel; r_0^3, which is an (inverse) indicator of wall shear stress; r_0^4, which is an (inverse) indicator of resistance; Reynolds number $Re = \frac{\rho D \overline{U}}{\mu}$, where D is the vessel diameter and $\overline{U}$ is the mean blood velocity.

In the following, we are going to illustrate the methodology adopted to assess the performance of these criteria, to identify the most suitable ones to construct hybrid networks of 1D-0D vessels. This adaptive model selection strategy will be then applied in Section 4.2 to two different arterial networks, the 37-artery network presented in Reference 1 and the reduced ADAN56 model reported in Reference 33.

Before starting, we point out that most of the criteria considered above are defined in terms of known geometrical and mechanical vessel properties. However, the mean flow rate $\overline{Q}$ through the vessel, as well as the average flow velocity $\overline{U}$, characterizing the nondimensional Reynolds number Re, are not known *a-priori* in all vessels of any generic network. In the present work, for both arterial networks to which this methodology is to be applied in Section 4.2, the 37-artery network and ADAN56 model, these quantities are computed for all vessels from the available reference solution, that is the 1D results. However, in general, this approach may not be feasible, especially for highly complex and large networks where computational results are not available *a-priori*.

Suppose to have an open arterial network with N_{tot} vessels (but this strategy can be also extended and applied to venous and arterio-venous closed-loop networks). First of all, for each parameter defining a criterion C, with $C \in \left\{l, r_0, V_0, C_0, \overline{Q}, r_0^3, r_0^4, Re\right\}$, we consider different 1D-0D thresholds $\gamma_1^C, \ldots, \gamma_p^C$. To determine these thresholds, we look at the distribution of the parameters of the vessels defining the different criteria: for each parameter, we choose a set of 1D-0D thresholds such that, when moving from a threshold γ_h^C to the consecutive one γ_{h+1}^C, for $h = 1, \ldots, p-1$, the number of 1D vessels that become 0D is sufficiently uniform. We do not require always the same number of vessels to be changed from 1D to 0D, but at least a certain regularity in the sampling procedure. Then, for each criterion C and each criterion threshold γ_h^C, with $h = 1, \ldots, p$, the corresponding hybrid network is constructed as follows

$$v^j = \begin{cases} 0D, & \text{if } C_j < \gamma_h^C, \\ 1D, & \text{otherwise,} \end{cases} \quad \text{for } j = 1, \ldots, N_{tot}, \tag{41}$$

where C_j denotes the value of the parameter defining the criterion C in the jth vessel.

In addition, by performing a dimensional analysis of the 1D blood flow Equations (1) (see Reference 27 for details), we have identified the following nondimensional coefficient, which characterizes the pressure term in the corresponding nondimensional momentum balance equation and may also be used as model selection criterion

$$\Gamma_P = \frac{T_0}{l\overline{U}}c^2, \tag{42}$$

where T_0 is the time scale, l is the longitudinal spatial scale (i.e., the vessel length), $\overline{U}$ is the average flow velocity and c is the wave speed. In particular, if we replace the wave speed c by a constant reference value c_0, the above nondimensional parameter Γ_P can be rewritten in terms of the intravascular volume V_0 and the compliance C_0, as follows

$$\Gamma_P = \frac{T_0}{\rho l\overline{U}}\frac{V_0}{C_0}. \tag{43}$$

As for the Reynolds number Re, calculating the value of the nondimensional pressure coefficient Γ_P in each vessel of a network also depends on available *a-priori* estimates of the average flow velocity $\overline{U}$, as discussed above.

In expression (43) defining Γ_P, the volume V_0 is at the numerator, which means that smaller values of V_0 correspond to smaller values of Γ_P, while, since the compliance C_0 is at the denominator of the definition of Γ_P, we have that smaller values of C_0 give larger values of the nondimensional coefficient Γ_P. Therefore, given a network of vessels and chosen a set of thresholds for the parameter Γ_P, this specific model selection criterion will be tested "in both directions". Namely, for each threshold, two corresponding hybrid networks are constructed, according to both the rule defined in (41) (this criterion will be called Γ_P "from below") and the following one (this criterion will be referred to as Γ_P "from above")

$$v^j = \begin{cases} 1D, & \text{if } C_j < \gamma_h^C, \\ 0D, & \text{otherwise,} \end{cases} \quad \text{for } j = 1, \dots, N_{tot}, \tag{44}$$

with $C = \Gamma_P$.

For each hybrid network available, the CPU time required by the simulation is recorded and the root mean square (RMS) relative errors in the predicted results are computed with respect to the reference 1D results, as follows

$$\varepsilon_P^{RMS} = \sqrt{\frac{1}{n}\sum_{i=1}^n \left(\frac{P_i - P_i^{ref}}{P_i^{ref}}\right)^2}, \qquad \varepsilon_Q^{RMS} = \sqrt{\frac{1}{n}\sum_{i=1}^n \left(\frac{Q_i - Q_i^{ref}}{\max_j\left(Q_j^{ref}\right)}\right)^2}, \tag{45}$$

where $i = 1, \dots, n$ are time points over the cardiac cycle at which the solution is sampled, P and Q are pressure and flow results from the hybrid network, while P^{ref} and Q^{ref} are reference pressure and flow results from the 1D network. In both configurations, in the 1D vessels the solution is sampled at the midpoint of the vessel. Other choices are possible (like, for example, averaged quantities over the 1D domain) and would not affect the conclusions of this work (results not reported here).

Hence, CPU time and errors distributions, as well as efficiency plots can be generated and analyzed for each criterion and compared between different criteria, in order to identify the model selection criteria providing the best trade-off between errors and computational cost.

We emphasize that out goal here is to identify suitable *a-priori* model selection criteria to construct hybrid networks of vessels. However, the choice of the specific threshold to be used for each parameter is not addressed, since it may depend on problem-specific characteristics, the aim of the application in mind and thus the level of accuracy required by the scientific question under consideration.

4 | NUMERICAL EXPERIMENTS

In this section we perform and discuss a series of numerical experiments to validate the proposed coupling approaches, verify their accuracy and test the adaptive model selection strategy devised in Section 3.4.

First, in Section 4.1 a family of convergence rate studies is carried out to check that the expected theoretical order of accuracy of the 1D and hybrid numerical couplings, presented in Sections 3.3.1 and 3.3.3, respectively, is achieved. In particular, we want to verify that the coupling to 0D vessels, as well as any type of boundary conditions, such as the coupling to terminal Windkessel elements, do not affect and harm the expected order of accuracy in the 1D vessels.

Next, the adaptive model selection strategy described in Section 3.4 to construct hybrid networks of vessels is applied to two different arterial models. In Section 4.2.1, we test the proposed methodology to the 37-artery network presented in Reference 1, an arterial tree made up of 37 silicone vessels representing the largest central systemic arteries of the human vascular system. Then, in Section 4.2.2, this adaptive strategy is applied to the ADAN56 model reported in Reference 33, which is a reduced version of the anatomically detailed arterial network (ADAN) model developed by Blanco et al.[3,14] and contains the largest 56 vessels of the human arterial system.

Finally, in Section 4.3 the validity of the 1D junction model presented in Section 2.3.1 is carefully assessed by comparing 1D simulation results for a simple bifurcation model to data obtained from a more complex 3D model.[54] Numerical predictions of flow rate, pressure, and changes in luminal radius are compared at several sites between the 1D and 3D models. In particular, total pressure variation and energy dissipation are evaluated across the bifurcation, to validate the

proposed 1D coupling approach and prove its ability to correctly describe flow splitting and reproduce wave propagation for the considered problem, while ensuring mass conservation and continuity of total pressure.

4.1 | Convergence rate studies

We carry out a set of convergence rate studies in order to verify that the expected order of accuracy of the adopted numerical schemes and, especially, of the proposed numerical coupling strategies is actually attained. We will also show that the problem-specific choice of the boundary conditions to be prescribed at initial and terminal branches of a network does not affect such order of accuracy. In particular, we have to check that both the 1D and the hybrid couplings preserve the expected, global second-order of accuracy, in both space and time, in the 1D vessels.

To this end, in Sections 4.1.1–4.1.3, by applying the method of manufactured solutions, we construct three different test problems for a modified nonlinear system of equations that is a perturbation of the original system via a source term vector. In this way, the modified non-homogeneous nonlinear system has a smooth, exact solution which can be used to assess the convergence rates of the numerical solution. Then, in Section 4.1.4, a convergence rate study is performed on different hybrid configurations of an aortic bifurcation model.

In the first three test problems performed by adopting the method of manufactured solutions, the exact solution is known, whereas, in the convergence rate study on the aortic bifurcation model, the exact solution is not known and replaced by a numerical reference solution. In the 1D vessels, the error at the output time between the numerical and the exact/reference solutions of each variable $\{A, q\}$ is measured in L^1-, L^2-, and L^∞-norms. The numerical solution is first reconstructed over each computational cell by applying the ENO reconstruction procedure. Then, by following the approach described in Reference 55, the integrals defining the error in the continuous L^1- and L^2-norms are approximated using a suitable quadrature formula over each computational cell: in the first three tests where the exact solution is known, we simply use the midpoint rule; for the aortic bifurcation model where a reference solution is available, we adopt the Gauss–Lobatto quadrature formula with 7 integration points. In both cases, the error in L^∞-norm is obtained by taking the maximum error arising in any of the integration points in any of the cells.

4.1.1 | Single vessel

We consider a single 1D vessel and we prescribe the following smooth function $\widehat{\boldsymbol{Q}}(x, t)$

$$\widehat{\boldsymbol{Q}}(x, t) = \begin{pmatrix} \widehat{A}(x, t) \\ \widehat{q}(x, t) \end{pmatrix} = \begin{pmatrix} A^c + \delta_A A^c \sin\left(\frac{2\pi}{l} x\right) \cos\left(\frac{2\pi}{T_0} t\right) \\ q^c - \delta_A A^c \frac{l}{T_0} \cos\left(\frac{2\pi}{l} x\right) \sin\left(\frac{2\pi}{T_0} t\right) \end{pmatrix}, \tag{46}$$

where the quantities A^c and q^c are average values, while the term δ_A represents the fluctuation around the average. The smooth function $\widehat{\boldsymbol{Q}}(x, t)$ does not necessarily satisfy the original 1D blood flow system (6) or, equivalently (8), but by inserting (46) into (8) we obtain a new non-homogeneous nonlinear system

$$\partial_t \boldsymbol{Q} + \boldsymbol{A}(\boldsymbol{Q}) \partial_x \boldsymbol{Q} = \boldsymbol{S}(\boldsymbol{Q}) + \widehat{\boldsymbol{S}}(x, t), \tag{47}$$

which represents a perturbation of the original system (8) and of which the function $\widehat{\boldsymbol{Q}}(x, t)$ is a smooth, exact solution. The new source term vector $\widehat{\boldsymbol{S}}(x, t)$, which depends on space x and time t only, arises from the fact that (46) is not a solution of the original system (6) and its explicit expression can be calculated using algebraic manipulators (not reported here).

Geometrical and mechanical vessel properties are: $r_0 = 1.4$ cm, $h = 0.5$ mm, $\rho = 1.060$ g/cm^3, $\mu = 0$ dyne s/cm^2, $E = 1.2 \cdot 10^7$ dyne/cm^2, $P_0 = p_{ext} = 0$ dyne/cm^2. Furthermore, we set: $l = 10^2$ cm, $T_0 = 1.0$ s, $A^c = A_0 = \pi r_0^2$, $\delta_A = 0.1$ and $q^c = 100$ ml/s. To perform the convergence rate study, we start from the coarsest mesh with $\overline{M} = 4$ computational cells and at each mesh refinement step we double the number of cells of the previous step. The output time of the simulations is $t_{end} = 0.5$ s and the time step is computed according to the CFL stability condition with $CFL = 0.9$. The initial condition is given by the smooth function (46) evaluated at $t = 0$, the 1D vessel is evolved by using the second-order

TABLE 1 Errors and empirical convergence rates obtained with the method of manufactured solutions for the single vessel test problem, with both periodic boundary conditions and prescribed variable boundary conditions with Riemann invariants.

Test	$\overline{M}$	L^1 A (cm^2)	q (ml/s)	L^2 A	q	L^∞ A	q	$O(L^1)$ A	q	$O(L^2)$ A	q	$O(L^\infty)$ A	q
Single vessel	4	4.93e+00	8.74e+03	5.52e-01	8.78e+02	8.32e-02	1.00e+02	-	-	-	-	-	-
+ periodic BCs	8	1.48e+00	1.20e+03	1.80e-01	1.24e+02	3.20e-02	1.66e+01	1.74	2.86	1.62	2.82	1.38	2.59
	16	4.32e-01	2.82e+02	4.94e-02	2.99e+01	7.73e-03	5.09e+00	1.77	2.09	1.86	2.05	2.05	1.70
	32	1.11e-01	6.94e+01	1.24e-02	7.50e+00	1.95e-03	1.51e+00	1.96	2.02	2.0	2.00	1.99	1.75
	64	2.70e-02	1.71e+01	3.00e-03	1.86e+00	4.65e-04	2.66e-01	2.04	2.02	2.04	2.01	2.07	2.51
	128	6.72e-03	4.26e+00	7.52e-04	4.64e-01	1.16e-04	7.44e-02	2.01	2.01	2.00	2.00	2.00	1.84
Single vessel	4	8.39e+00	1.06e+04	9.63e-01	1.25e+03	1.42e-01	1.74e+02	-	-	-	-	-	-
+ Riemann inv. BCs	8	4.48e+00	1.87e+03	4.75e-01	2.37e+02	7.48e-02	4.43e+01	0.90	2.50	1.02	2.40	0.93	1.97
	16	1.27e+00	4.46e+02	1.39e-01	5.42e+01	2.28e-02	1.23e+01	1.82	2.07	1.77	2.13	1.71	1.84
	32	3.18e-01	1.09e+02	3.56e-02	1.32e+01	6.51e-03	3.30e+00	1.99	2.03	1.97	2.04	1.81	1.90
	64	7.99e-02	2.70e+01	9.07e-03	3.19e+00	1.64e-03	7.02e-01	1.99	2.01	1.97	2.05	1.99	2.23
	128	2.00e-02	6.71e+00	2.27e-03	7.93e-01	4.05e-04	1.75e-01	2.00	2.01	2.00	2.01	2.02	2.01

MUSCL-Hancock scheme presented in Section 3.1 and the same test problem is solved by prescribing two different sets of boundary conditions. In the first case, periodic boundary conditions are assigned at both left and right extremities of the vessel; instead, in the second case, at each boundary interface the value of one of the two variables, either cross-sectional area or flow rate, is prescribed to be equal to the corresponding variable of the exact solution, while the other variable is computed by imposing the continuity of the Riemann invariants across the boundary interface. Here, we will show results obtained by prescribing the value of the flow rate q at the left interface and the value of the cross-sectional area A at the right boundary, but other choices are also possible.

Errors between the numerical solution and the exact solution and empirical convergence rates are computed in norms L^1, L^2, and L^∞ and are reported in Table 1. The expected convergence rates are reached in both variables, A and q, for all norms and regardless the choice of the prescribed boundary conditions. Indeed, from Table 1 we conclude that errors are decreasing and the numerical solution is converging to the exact one with the correct and expected order of accuracy also in the case where boundary conditions are assigned via the continuity of the Riemann invariants.

4.1.2 | Single vessel coupled to a Windkessel model

In this section, we extend the method of manufactured solutions described and adopted in the previous convergence study of a single 1D vessel to the case of a 1D vessel coupled to an *RCR* Windkessel (WK) terminal model. Indeed, we want to verify that the coupling between the 1D vessel and the three-element lumped-parameter model does not affect and penalize the expected convergence rate in the 1D vessel.

The time evolution of the pressure $P_{wk}(t)$ in the Windkessel is governed by the following linear ODE

$$\begin{cases} \dfrac{d}{dt}P_{wk}(t) = \dfrac{Q_{in}(t) - Q_{wk}(t)}{C}, \\ Q_{wk}(t) = \dfrac{P_{wk}(t) - P_{out}}{R_2} \end{cases} \quad \Rightarrow \quad \dfrac{d}{dt}P_{wk}(t) = \dfrac{1}{C}\left[Q_{in}(t) - \dfrac{P_{wk}(t) - P_{out}}{R_2}\right], \tag{48}$$

where $Q_{wk}(t)$ is the flow rate through the Windkessel model, the parameters C and R_2 denote the compliance and the distal resistance of the *RCR* model, respectively, $Q_{in}(t)$ is the time-dependent inflow prescribed at the inlet of the Windkessel and P_{out} is a constant outflow pressure assigned at its outlet. In particular, if in the 1D vessel we still prescribe the following

smooth, exact function for the flow rate $\widehat{q}(x, t)$

$$\widehat{q}(x, t) = q^c - \delta_A A^c \frac{l}{T_0} \cos\left(\frac{2\pi}{l}x\right) \sin\left(\frac{2\pi}{T_0}t\right), \tag{49}$$

then, for the mass conservation principle, the inflow $Q_{\text{in}}(t)$ to the Windkessel model will be given by the flow rate leaving the 1D vessel, that is

$$Q_{\text{in}}(t) = \widehat{q}(x = l, t) = q^c - \delta_A A^c \frac{l}{T_0} \sin\left(\frac{2\pi}{T_0}t\right), \quad t \geq 0. \tag{50}$$

Equipped with the explicit expression (50) of $Q_{\text{in}}(t)$, by inserting (50) into the ODE (48) and integrating in time such equation, with the help of the integrating factor $e^{\int \frac{1}{R_2 C} dt} = e^{\frac{t}{R_2 C}}$ it is possible to derive the analytical solution of the three-element lumped-parameter model with prescribed time-dependent inflow $Q_{\text{in}}(t)$ and constant output pressure P_{out}. After straightforward calculations, we get

$$\widehat{P}_{wk}(t) = P_{\text{out}} + \tilde{\gamma}e^{-\frac{t}{R_2 C}} + R_2 \left\{ q^c - \frac{\delta_A A^c l}{T_0^2 + (2\pi R_2 C)^2} \left[T_0 \sin\left(\frac{2\pi}{T_0}t\right) - 2\pi R_2 C \cos\left(\frac{2\pi}{T_0}t\right) \right] \right\}, \tag{51}$$

where $\tilde{\gamma}$ is the integration constant obtained by imposing the initial condition $\widehat{P}_{wk}(t = 0) = P_{wk,0}$ and given by

$$\tilde{\gamma} = P_{wk,0} - P_{\text{out}} - R_2 \left[q^c + \frac{(\delta_A A^c l)(2\pi R_2 C)}{T_0^2 + (2\pi R_2 C)^2} \right]. \tag{52}$$

Together with the conservation of flow, we also want the continuity of pressure to be ensured at the vessel-Windkessel coupling interface. Therefore, the exact, smooth function for the vessel cross-sectional area $\widehat{A}(x, t)$ must be chosen such that

$$p(\widehat{A}(x = l, t)) = P_{in,wk}(t) = \widehat{P}_{wk}(t) + R_1 Q_{\text{in}}(t) = \widehat{P}_{wk}(t) + R_1 \widehat{q}(x = l, t), \quad t \geq 0, \tag{53}$$

where R_1 is the proximal resistance of the Windkessel model. Then, the smooth function for $\widehat{A}(x, t)$ proposed in (46) can be appropriately modified as follows, so that condition (53) is satisfied for any $t \geq 0$

$$\widehat{A}(x, t) = A_0 \left[1 + \frac{1}{K}\left(\widehat{P}_{wk}(t) + R_1 \widehat{q}(x = l, t) - P_0\right) \right]^2 + \delta_A A^c \sin\left(\frac{2\pi}{l}x\right) \cos\left(\frac{2\pi}{T_0}t\right), \tag{54}$$

where the first term in (54) is the inverse of the tube law (3)–(4) (with $m = 0.5$, $n = 0$ and $p_{ext} = 0$) evaluated at $P_{in,wk}(t)$ as given in (53) and replaces the constant average quantity A^c. It easy to check that, for any $t \geq 0$, the proposed function (54) for $\widehat{A}(x, t)$ satisfies the pressure continuity condition (53).

Hence, the smooth functions (54) and (49) constitute the analytical solution to the modified nonlinear blood flow system of the form (47), while the function (51) is the exact solution to the *RCR* Windkessel model governed by equation (48). These functions have been constructed in a way that the coupling conditions between the two models, namely conservation of mass and continuity of pressure, are exactly verified.

This test problem is applied to the upper thoracic aorta model reported in Reference 33, where the thoracic aorta from the aortic root to the descending aorta is simulated as a single vessel with uniform properties coupled to a three-element lumped parameter model of the rest of the systemic circulation. Geometrical and mechanical properties of both the vessel and the Windkessel are taken from Reference 33 and summarized in Table 2. The tube law (3) is adopted with $P_0 = P_d$ and $A_0 = A_d$, where P_d and A_d are the diastolic pressure and the corresponding vessel cross-section. Furthermore, we set: $T_0 = 1.0$ s, $A^c = A_d$, $\delta_A = 0.1$, $q^c = 0$ ml/s and $P_{wk,0} = 0$ dyne/cm^2. To perform the convergence rate study, we refine the mesh size in the 1D vessel by a factor of 2. The output time of the simulations is $t_{end} = 0.5$ s and the time step is computed according to the CFL stability condition with $CFL = 0.9$. The 1D vessel is solved by using the second-order MUSCL-Hancock scheme, while the Windkessel model is evolved using RK4 method with the same time step of the 1D vessel. At the left vessel boundary, we prescribe the flow rate and compute the cross-sectional area from the continuity of

TABLE 2 Geometrical and mechanical properties of the model of the upper thoracic aorta coupled to an *RCR* Windkessel element.

Property	Value
Length, l	24.137 cm
Radius at diastolic pressure, r_d	1.2 cm
Area at diastolic pressure, A_d	$\pi r_d^2 = 4.5$ cm^2
Wall thickness, h	1.2 mm
Blood density, ρ	1.060 g/cm^3
Blood viscosity, μ	0.04 dyne s/cm^2
Velocity profile order, ζ	9
Young's modulus, E	$4.0 \cdot 10^6$ dyne/cm^2
Diastolic pressure, P_d	$9.4\hat{6} \cdot 10^4$ dyne/cm^2
External pressure, p_{ext}	0
Outflow pressure, P_{out}	0
WK resistance, R_1	$1.1752 \cdot 10^2$ dyne s/cm^5
WK compliance, C	$1.0163 \cdot 10^{-3}$ cm^5/dyne
WK resistance, R_2	$1.1167 \cdot 10^3$ dyne s/cm^5

TABLE 3 Errors and empirical convergence rates obtained with the method of manufactured solutions for the test problem consisting of a single 1D vessel coupled to an *RCR* Windkessel element.

Test	$\overline{M}$	L^1 A (cm^2)	q (ml/s)	L^2 A	q	L^∞ A	q	$O(L^1)$ A	q	$O(L^2)$ A	q	$O(L^\infty)$ A	q
Single vessel + WK element	4	1.70e+00	1.28e+03	3.84e-01	2.62e+02	1.22e-01	6.14e+01	-	-	-	-	-	-
	8	5.54e-01	1.69e+02	1.17e-01	3.49e+01	2.97e-02	8.80e+00	1.62	2.92	1.71	2.91	2.04	2.80
	16	1.41e-01	2.88e+01	3.05e-02	7.33e+00	8.62e-03	2.68e+00	1.97	2.55	1.94	2.25	1.78	1.71
	32	3.64e-02	5.40e+00	8.17e-03	1.16e+00	2.40e-03	3.71e-01	1.96	2.41	1.90	2.66	1.84	2.86
	64	9.14e-03	1.17e+00	2.04e-03	2.67e-01	6.26e-04	1.16e-01	1.99	2.20	2.00	2.12	1.94	1.68
	128	2.29e-03	2.72e-01	5.13e-04	6.42e-02	1.58e-04	3.59e-02	2.00	2.11	2.00	2.06	1.99	1.69

the Riemann invariant; at the right boundary interface, which is coupled to the three-element Windkessel, we compute the vessel unknown boundary state $Q^* = (A^*, q^*)$ by setting

$$q^* = \frac{p(A^*) - P_{wk}}{R_1}, \tag{55}$$

and imposing the continuity of the Riemann invariant to connect the unknown state Q^* to the given state in the last computational cell of the vessel. Once Q^* has been calculated, we prescribe the inflow to the Windkessel element as $Q_{in} = q^*$. Since equation (48) for the pressure P_{wk} in the Windkessel, equipped with the initial condition $P_{wk}(t = 0) = P_{wk,0}$, is solved numerically by using RK4 method, the coupling conditions between the 1D vessel and the terminal Windkessel model are updated at each one of the four intermediate steps of RK4 scheme and the time integral of the boundary flux in the 1D vessel is approximated with a procedure analogous to the one proposed in Section 3.3.3 for the hybrid coupling between 1D and 0D vessels.

Errors between the numerical solution and the exact solution and empirical convergence rates for this convergence study are summarized in Table 3. We observe that the numerical solution converges with the expected order in all norms, proving that the coupling between the 1D vessel and the Windkessel model is able to preserve the correct order of accuracy in the 1D vessel.

TABLE 4 Errors and empirical convergence rates obtained with the method of manufactured solutions for the test problem consisting of a closed-loop network of two 1D vessels connected at both extremities.

Test	$\overline{M}$	L^1 A (cm^2)	q (ml/s)	L^2 A	q	L^∞ A	q	$O(L^1)$ A	q	$O(L^2)$ A	q	$O(L^\infty)$ A	q
Two-vessel network	4	5.16e+00	8.49e+03	6.04e-01	8.59e+02	9.54e-02	1.03e+02	-	-	-	-	-	-
	8	1.48e+00	1.20e+03	1.81e-01	1.24e+02	3.22e-02	1.66e+01	1.80	2.82	1.74	2.79	1.57	2.63
	16	4.32e-01	2.82e+02	4.94e-02	2.99e+01	7.73e-03	5.09e+00	1.78	2.09	1.87	2.05	2.06	1.70
	32	1.11e-01	6.94e+01	1.24e-02	7.50e+00	1.95e-03	1.51e+00	1.96	2.02	2.00	2.00	1.99	1.75
	64	2.70e-02	1.71e+01	3.00e-03	1.86e+00	4.65e-04	2.66e-01	2.04	2.02	2.04	2.01	2.07	2.51
	128	6.72e-03	4.26e+00	7.52e-04	4.64e-01	1.16e-04	7.44e-02	2.01	2.01	2.00	2.00	2.00	1.84

4.1.3 | Closed-loop two-vessel network

Here we reproduce the convergence test proposed by Müller and Blanco in Reference 30, which is performed over a network of two 1D vessels connected at both extremities, thus forming a closed loop where each connection represents a 1D coupling problem.

The method of manufactured solutions is adopted: the smooth, exact function $\widehat{Q}(x, t)$, all geometrical and mechanical properties for both vessels and the other parameters, the simulation setup for the convergence study are those used in the convergence test for the single vessel performed in Section 4.1.1.

Table 4 displays the errors between the numerical solution and the exact solution measured in the norms L^1, L^2, and L^∞ and the corresponding empirical convergence rates, for one of the two vessels of the closed-loop network. Also in this test problem, the expected convergence rates are reached for all norms, thus demonstrating that the adopted 1D numerical coupling strategy is second-order accurate.

4.1.4 | Aortic bifurcation model

We consider a single bifurcation model, the aortic bifurcation model reported in Reference 33, which consists of a parent vessel, the abdominal aorta, branching into two daughter vessels, the iliac arteries. The 1D and different hybrid configurations of this bifurcation model are constructed, to verify that the expected convergence rates are always achieved by the proposed numerical schemes:

Test 1   All vessels: 1D;
Test 2   Aorta: 1D; L iliac: 0D, two-split (P_{in}, Q_{out})-type; R iliac: 0D, (P_{in}, P_{out})-type;
Test 3   Aorta: 0D, (Q_{in}, Q_{out})-type; L iliac: 1D; R iliac: 0D, two-split (P_{in}, Q_{out})-type;
Test 4   Aorta: 1D; L iliac: 1D; R iliac: 0D, (P_{in}, P_{out})-type.

In the first test, the three coupled 1D vessels define a 1D coupling problem; in Tests 2 and 3, we have two different arrangements of a junction connecting one 1D vessel and two 0D vessels; in the last test, a hybrid coupling problem between two 1D vessels and one 0D vessel is to be solved.

The inflow boundary condition $q_{in}(t)$ prescribed at the inlet of the abdominal aorta is an in vivo signal taken from Reference 32 and available in the Supporting Information of Reference 33; both iliac arteries are coupled to *RCR* Windkessel terminal models, with a methodology similar to the one described and adopted in Section 4.1.2 for the single 1D vessel coupled to a Windkessel model. Geometrical and mechanical properties of this network are taken from Reference 33 and listed in Table 5. Initial pressure and velocity are set to zero for all vessels, while initial cross-sectional areas corresponding to zero pressure are computed from the tube law (3), with $P_0 = P_d$ and $A_0 = A_d$.

To perform the convergence rate study, in all tests we set the maximum mesh size for the coarsest mesh to $\Delta x_{max} = 2$ cm. In each vessel of the bifurcation model, the number of computational cells corresponding to the mesh size Δx_{max} is computed according to formula (31), which gives $\overline{M}_1 = 5$ in both parent and daughter vessels. Then, the number of cells used in each mesh refinement step in each one of the vessels is always obtained by doubling the number of cells used in the previous step. For each configuration, the exact solution is replaced by a reference solution computed on a very fine

TABLE 5 Geometrical and mechanical properties of the aortic bifurcation model from Reference 33.

Property	Aorta	Iliac arteries
Length, l	8.6 cm	8.5 cm
Radius at diastolic pressure, r_d	0.86 cm	0.60 cm
Area at diastolic pressure, A_d	2.3235 cm^2	1.1310 cm^2
Wall thickness, h	1.032 mm	0.72 mm
Blood density, ρ	1.060 g/cm^3	
Blood viscosity, μ	0.04 dyne s/cm^2	
Velocity profile order, ζ	9	
Young's modulus, E	5.0·10^6 dyne/cm^2	7.0·10^6 dyne/cm^2
Diastolic pressure, P_d	9.4ê ·10^4 dyne/cm^2	9.4ê ·10^4 dyne/cm^2
External pressure, p_{ext}	0	
Outflow pressure, P_{out}	-	0
WK resistance, R_1	-	6.8123·10^2 dyne s/cm^5
WK compliance, C	-	3.6664·10^{-5} cm^5/dyne
WK resistance, R_2	-	3.1013·10^4 dyne s/cm^5

mesh with $\overline{M}_{ref} = \overline{M}_1 \cdot 2^8 = 1280$ computational cells. For all tests, the output time is taken as $t_{end} = 20T_0$, with $T_0 = 1.1$ s, which ensures that the periodic regime has been reached in all vessels of the network; a global time step is used and computed as in (33), with CFL number $CFL = 0.9$.

We point out that, since 1D mesh size Δx and time step Δt are related via the CFL stability condition and since we use the same global time step for all 1D and 0D vessels, in the hybrid configurations (Test 2–4) the space refinement in the 1D vessels also implies a refinement of the time resolution in the 0D vessels.

Tables 6–9 display the computed errors and empirical convergence rates corresponding to the four configurations considered of the aortic bifurcation model, for both cross-sectional area and flow rate and in all the three norms, L^1, L^2, and L^∞. For the 1D configuration, Table 6 shows that the errors decrease and the numerical solution converges with the expected order in all vessels and for all norms, even with reduced number of computational cells discretizing the domain. Hence, these results prove once again that the 1D numerical coupling presented in Section 3.3.1 is second-order accurate in space and time and preserves the expected order in all 1D vessels joining at the junction. In the same way, for all the three different hybrid configurations assessed, we conclude that the expected convergence rates are achieved in all 1D vessels of each test and for all norms, as demonstrated in Tables 7–9. The hybrid numerical coupling proposed in Section 3.3.3 is then proved to be second-order accurate, in both space and time, in solving the 1D vessels of the junction. In particular, these results show that, by adopting the methodology proposed in Section 3.3.3 to solve the hybrid coupling at junctions of 1D and 0D vessels, the accuracy of the solution in the 1D vessels is not affected by the coupling with 0D vessels.

In conclusion, this convergence study demonstrates that the expected convergence rates are achieved by both the 1D and hybrid numerical coupling procedures introduced in Section 3.3 to solve networks of vessels.

4.2 | Application of the adaptive model selection strategy

Here we apply the adaptive model selection strategy proposed and described in Section 3.4 to two different arterial models, the 37-artery network presented in Reference 1 and the reduced ADAN56 model reported in Reference 33. Among all the *a-priori* model selection criteria considered, we want to identify the ones with the best performance, namely those criteria that, when employed to determine the most suitable model (1D/0D) to be used for each vessel of a network, provide the best trade-off between computational cost and accuracy in the resulting hybrid network configurations.

We proceed as follows. For each arterial model, we look at the distribution of the parameters of the vessels defining the different criteria, in order to choose, for each criterion, a set of 1D-0D thresholds to be used to construct the corresponding hybrid configurations to test. As discussed in Section 3.4, these sets of 1D-0D thresholds are selected in a way to ensure

TABLE 6 Test 1: Errors and empirical convergence rates obtained for the 1D configuration of the aortic bifurcation model.

Vessel	$\overline{M}$	L^1 A (cm²)	q (ml/s)	L^2 A	q	L^∞ A	q	$O(L^1)$ A	q	$O(L^2)$ A	q	$O(L^\infty)$ A	q
Aorta (1D)	5	1.31e-04	9.09e-02	5.44e-05	3.92e-02	5.63e-05	5.02e-02	-	-	-	-	-	-
	10	3.48e-05	2.14e-02	1.49e-05	8.97e-03	1.71e-05	1.13e-02	1.91	2.09	1.87	2.13	1.72	2.16
	20	8.77e-06	5.44e-03	3.82e-06	2.29e-03	4.36e-06	2.68e-03	1.99	1.98	1.96	1.97	1.97	2.07
	40	2.26e-06	1.42e-03	1.01e-06	6.21e-04	1.06e-06	7.04e-04	1.96	1.93	1.92	1.88	2.03	1.93
	80	5.81e-07	3.65e-04	2.75e-07	1.68e-04	3.98e-07	2.39e-04	1.96	1.97	1.88	1.89	1.42	1.56
L/R iliac (1D)	5	1.36e-05	1.09e-02	5.75e-06	4.22e-03	5.54e-06	3.48e-03	-	-	-	-	-	-
	10	2.95e-06	2.71e-03	1.29e-06	1.06e-03	1.52e-06	9.47e-04	2.21	2.01	2.16	1.99	1.86	1.88
	20	6.90e-07	6.60e-04	3.01e-07	2.53e-04	3.84e-07	2.23e-04	2.09	2.04	2.10	2.07	1.99	2.08
	40	1.71e-07	1.61e-04	7.51e-08	6.31e-05	1.02e-07	6.17e-05	2.01	2.03	2.00	2.00	1.91	1.86
	80	4.68e-08	4.00e-05	2.05e-08	1.59e-05	2.75e-08	1.99e-05	1.87	2.01	1.88	1.99	1.89	1.63

TABLE 7 Test 2: Errors and empirical convergence rates obtained for a hybrid configuration of the aortic bifurcation model.

Vessel	$\overline{M}$	L^1 A (cm²)	q (ml/s)	L^2 A	q	L^∞ A	q	$O(L^1)$ A	q	$O(L^2)$ A	q	$O(L^\infty)$ A	q
Aorta (1D)	5	1.52e-04	6.75e-02	6.12e-05	2.87e-02	5.82e-05	3.52e-02	-	-	-	-	-	-
	10	3.75e-05	1.75e-02	1.55e-05	7.36e-03	1.69e-05	9.22e-03	2.02	1.95	1.98	1.96	1.78	1.93
	20	1.02e-05	6.00e-03	4.43e-06	2.67e-03	5.23e-06	2.73e-03	1.88	1.54	1.81	1.46	1.69	1.76
	40	2.66e-06	1.36e-03	1.10e-06	6.04e-04	1.21e-06	6.16e-04	1.94	2.15	2.01	2.14	2.12	2.15
	80	6.43e-07	3.55e-04	2.67e-07	1.57e-04	2.90e-07	2.03e-04	2.05	1.93	2.04	1.95	2.06	1.60

TABLE 8 Test 3: Errors and empirical convergence rates obtained for a hybrid configuration of the aortic bifurcation model.

Vessel	$\overline{M}$	L^1 A (cm²)	q (ml/s)	L^2 A	q	L^∞ A	q	$O(L^1)$ A	q	$O(L^2)$ A	q	$O(L^\infty)$ A	q
L iliac (1D)	5	1.42e-05	8.32e-03	6.57e-06	3.33e-03	5.39e-06	3.28e-03	-	-	-	-	-	-
	10	3.51e-06	1.74e-03	1.56e-06	7.93e-04	1.61e-06	1.14e-03	2.02	2.25	2.07	2.07	1.74	1.52
	20	8.51e-07	4.43e-04	3.76e-07	2.01e-04	4.09e-07	2.72e-04	2.04	1.98	2.05	1.98	1.98	2.07
	40	2.12e-07	1.10e-04	9.40e-08	5.08e-05	1.15e-07	7.48e-05	2.01	2.01	2.00	1.98	1.84	1.86
	80	5.18e-08	2.77e-05	2.32e-08	1.29e-05	2.91e-08	2.06e-05	2.03	1.99	2.02	1.98	1.98	1.86

that, for each criterion, the number of 1D vessels that become 0D when moving from a threshold to the consecutive one is kept quite uniform and regular. For the numerical experiments performed in this section, the specific thresholds adopted to test the different *a-priori* model selection criteria are reported in Tables 11 and 12 for the 37-artery network, in Tables 14 and 15 for ADAN56 model.

For both the 37-artery network and ADAN56 model, the characteristic mesh spacing for 1D vessels is $\Delta x_{max} = 1$ mm, with all vessels discretized by at least two computational cells. The CFL number is set to 0.9 for all simulations and, at each time level n, a global time step Δt^n is used and computed as in (33). For the 0D simulations, the time step is constant and set to $\Delta t^m = 10^{-4}$ s, which ensures the stability of the adopted numerical method to solve 0D vessels and the mesh independence of the solution, for both the 37-artery network and ADAN56 model. The output time t_{end} is not fixed, but each simulation is run until periodic regime is reached in all vessels of the network, where periodicity is defined

TABLE 9 Test 4: Errors and empirical convergence rates obtained for a hybrid configuration of the aortic bifurcation model.

Vessel	$\overline{M}$	L^1		L^2		L^∞		$O(L^1)$		$O(L^2)$		$O(L^\infty)$	
		A (cm^2)	q (ml/s)	A	q	A	q	A	q	A	q	A	q
Aorta (1D)	5	1.45e-04	9.74e-02	6.04e-05	4.16e-02	6.18e-05	5.20e-02	-	-	-	-	-	-
	10	3.77e-05	2.28e-02	1.62e-05	9.67e-03	2.05e-05	1.15e-02	1.94	2.10	1.90	2.11	1.59	2.17
	20	9.63e-06	5.76e-03	4.20e-06	2.46e-03	5.23e-06	2.69e-03	1.97	1.98	1.95	1.97	1.97	2.10
	40	2.47e-06	1.49e-03	1.12e-06	6.64e-04	1.37e-06	7.36e-04	1.96	1.95	1.91	1.89	1.94	1.87
	80	6.22e-07	3.81e-04	2.92e-07	1.76e-04	4.06e-07	2.42e-04	1.99	1.97	1.94	1.92	1.75	1.61
L iliac (1D)	5	1.26e-05	8.87e-03	5.45e-06	3.56e-03	5.70e-06	3.73e-03	-	-	-	-	-	-
	10	2.88e-06	2.68e-03	1.27e-06	1.02e-03	1.32e-06	8.02e-04	2.13	1.73	2.10	1.80	2.11	2.22
	20	7.01e-07	6.61e-04	3.05e-07	2.61e-04	3.33e-07	1.91e-04	2.04	2.02	2.06	1.96	1.98	2.07
	40	1.82e-07	1.69e-04	7.68e-08	6.80e-05	8.47e-08	6.10e-05	1.94	1.96	1.99	1.94	1.98	1.65
	80	4.50e-08	4.28e-05	1.90e-08	1.75e-05	2.22e-08	1.97e-05	2.02	1.98	2.01	1.96	1.93	1.63

TABLE 10 Main model parameters of the 37-artery network.

Property	Value
Blood density, ρ	1.050 g/cm^3
Blood viscosity, μ	0.025 dyne s/cm^2
Velocity profile order, ζ	9
Young's modulus, E	$1.2 \cdot 10^7$ dyne/cm^2
Diastolic pressure, P_d	0
External pressure, p_{ext}	0
Outflow pressure, P_{out}	$4.2663 \cdot 10^3$ dyne/cm^2 (3.2 mmHg)

as the L^∞-distance between the normalized solutions over two consecutive cardiac cycles to be smaller than a tolerance of 10^{-3}. In the 0D and hybrid configurations of both arterial models, the 0D vessel type to assign to each 0D vessel is chosen as follows: (Q_{in}, Q_{out})-type if the 0D vessel is the first vessel at the inlet of the network; (P_{in}, P_{out})-type if the 0D vessel is a terminal vessel, coupled either to a single-resistance or to an *RCR* Windkessel model; two-split (P_{in}, Q_{out})-type 0D vessel otherwise. For each criterion C and each criterion threshold γ_h^C, $h = 1, \ldots, p$, the RMS relative errors between the computational results obtained from the hybrid network configuration and the reference 1D results are computed as explained in Section 3.4 according to formulae (45).

All simulations were executed in Python, running on a Linux Ubuntu 18.04 machine with AMD® Ryzen™ Threadripper™ 3990X Processor (Base Clock: 2.9 GHz, Max. Boost Clock: up to 4.3 GHz, 64 CPU Cores/128 threads, total L3 cache: 256 MB). In particular, to retrieve the CPU times, each simulation was run over a single cardiac cycle for five consecutive times, the CPU time of each execution was recorded and then the mean CPU time was computed by taking the average between the different values obtained. Furthermore, the coefficient of variation, defined as the ratio of the standard deviation to the mean CPU time, was computed for each set of five CPU times to verify that the variability of the sample in relation to the mean CPU time value was negligible (results not reported).

4.2.1 | 37-arteries network

We consider the arterial network presented in Reference 1, for which in vitro pressure and flow measurements were acquired at multiple locations. The tree is made up of 37 silicone vessels representing the largest central systemic arteries of the human vascular system. At the inlet of the ascending aorta, a periodic flow measured in the experiment is prescribed as a periodic inflow boundary condition. Outflow boundary conditions are prescribed by coupling terminal vessels to
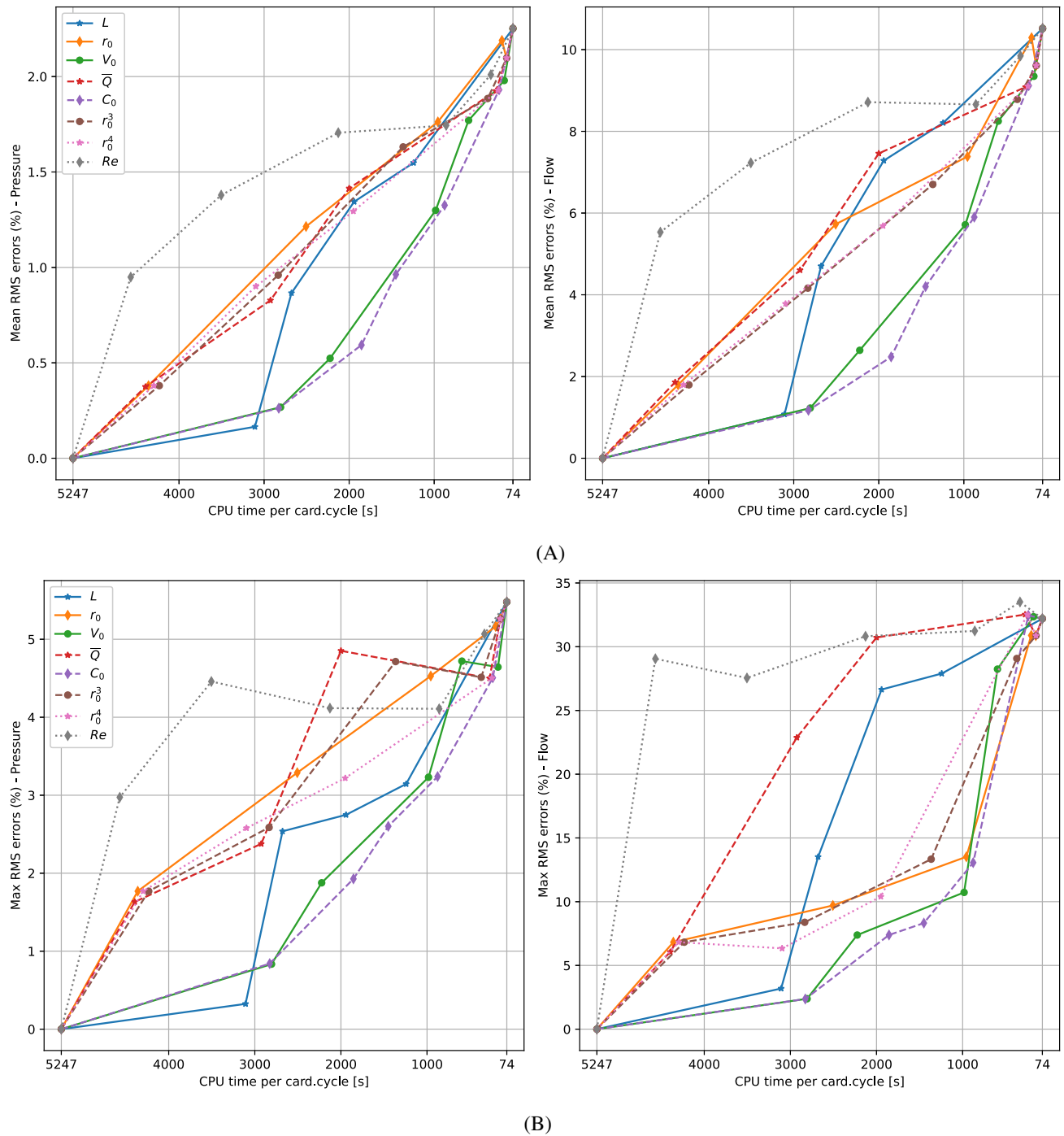
FIGURE 2 Efficiency plots generated for the **37-artery network** with CPU time per cardiac cycle versus (A) mean and (B) maximum RMS relative errors for both pressure and flow rate, to assess and compare the performance of the different *a-priori* model selection criteria tested.

single-resistance models, characterizing the peripheral resistance to the flow. In all vessels, whether 1D or 0D, zero pressure and flow rate are imposed as initial conditions, and the cross-sectional area corresponding to the zero initial pressure is computed from the tube law (3), for each 1D vessel, or (15), for each 0D vessel, with reference pressure $P_0 = P_d = 0$ and cross-sectional area $A_0 = A_d$. General model parameters of this arterial network are summarized in Table 10, while for a complete set of parameters, we refer the reader to References 1 and 2 and to the Supplementary Information of Reference 33. We remark that, differently from the just mentioned papers, in this work 1D vascular segments do not include vessel tapering, but the reference constant radius r_0 is computed as the mean value between the cross-sectional radii at the inlet and outlet of the vessel, r_{in} and r_{out}, respectively.

TABLE 11 Results obtained by applying the proposed adaptive model selection strategy to the **37-artery network**.

Criterion C	Thresh. γ^C	Tot.1D length (cm)	Tot.1D cells	Mean CPU time (s)	Speed-up wrt 1D	Mean ε_P^{RMS} (%) (std.dev)	Mean ε_Q^{RMS} (%) (std.dev)	Max ε_P^{RMS} (%)	Max ε_Q^{RMS} (%)
1D	-	524.9	5250	5246.76	-	-	-	-	-
0D	-	0.0	0	73.92	71.0	2.25 (1.40)	1.05e+01 (5.15)	5.48	3.22e+01
Length l (cm)	5.0	507.7	5077	3107.76	1.7	1.65e-01 (6.93e-02)	1.08 (5.34e-01)	3.24e-01	3.19
	13.0	441.9	4419	2678.07	2.0	8.66e-01 (5.58e-01)	4.70 (2.19)	2.54	1.35e+01
	18.0	311.6	3116	1941.23	2.7	1.34 (7.15e-01)	7.28 (4.87)	2.75	2.66e+01
	20.0	196.0	1960	1242.85	4.2	1.55 (7.98e-01)	8.21 (5.09)	3.14	2.79e+01
Radius r_0 (cm)	0.2	427.1	4272	4359.05	1.2	3.80e-01 (3.46e-01)	1.80 (1.53)	1.77	6.82
	0.3	236.1	2362	2506.87	2.1	1.21 (8.83e-01)	5.73 (1.79)	3.29	9.70
	0.4	75.1	752	956.91	5.5	1.76 (1.25)	7.38 (2.52)	4.53	1.35e+01
	0.7	31.1	312	203.63	25.8	2.19 (1.30)	1.03e+01 (4.89)	5.17	3.09e+01
	1.0	21.4	215	150.23	34.9	2.10 (1.41)	9.61 (5.22)	5.26	3.09e+01
Volume V_0 (cm^3)	2.0	460.2	4603	2805.93	1.9	2.67e-01 (2.18e-01)	1.23 (5.49e-01)	8.34e-01	2.38
	3.0	360.7	3608	2223.83	2.4	5.24e-01 (3.91e-01)	2.64 (1.84)	1.88	7.38
	6.0	177.7	1778	983.01	5.3	1.30 (8.98e-01)	5.71 (2.14)	3.23	1.07e+01
	10.0	100.3	1004	595.47	8.8	1.77 (1.27)	8.25 (4.87)	4.72	2.82e+01
	15.0	26.8	268	176.51	29.7	1.98 (1.22)	9.35 (5.43)	4.64	3.24e+01
Compl. C_0 (cm^5/dyne)	3.0e-06	464.7	4648	2827.20	1.9	2.62e-01 (2.20e-01)	1.17 (5.26e-01)	8.40e-01	2.37
	4.5e-06	351.0	3511	1854.93	2.8	5.93e-01 (4.66e-01)	2.48 (1.18)	1.9	7.39
	1.0e-05	271.4	2715	1450.35	3.6	9.63e-01 (6.82e-01)	4.20 (1.61)	2.60	8.32
	1.5e-05	158.2	1583	877.42	6.0	1.33 (8.94e-01)	5.90 (2.50)	3.24	1.31e+01
	2.5e-05	38.0	381	236.65	22.2	1.93 (1.23)	9.12 (5.56)	4.51	3.25e+01
Mean flow $\overline{Q}$ (ml/s)	3.0	435.3	4354	4394.34	1.2	3.75e-01 (3.41e-01)	1.86 (1.42)	1.63	6.06
	4.0	282.1	2822	2925.38	1.8	8.27e-01 (4.99e-01)	4.60 (3.85)	2.38	2.29e+01
	5.0	185.4	1855	1999.65	2.6	1.41 (1.11)	7.46 (5.75)	4.85	3.07e+01
	7.0	45.3	454	273.68	19.2	1.92 (1.23)	9.09 (5.55)	4.50	3.25e+01
	20.0	21.4	215	149.47	35.1	2.10 (1.41)	9.61 (5.22)	5.26	3.09e+01

TABLE 11 (Continued)

Criterion C	Thresh. γ^C	Tot.1D length (cm)	Tot.1D cells	Mean CPU time (s)	Speed-up wrt 1D	Mean ε_P^{RMS} (%) (std.dev)	Mean ε_Q^{RMS} (%) (std.dev)	Max ε_P^{RMS} (%)	Max ε_Q^{RMS} (%)
r_0^3 (cm^3)	8.0e-03	427.1	4272	4232.07	1.2	3.80e-01 (3.46e-01)	1.80 (1.53)	1.80	6.82
	2.0e-02	277.2	2773	2833.90	1.9	9.60e-01 (6.78e-01)	4.16 (1.57)	2.59	8.38
	5.0e-02	123.4	1235	1365.26	3.8	1.63 (1.30)	6.70 (2.69)	4.71	1.33e+01
	1.0e-01	59.3	594	371.07	14.1	1.88 (1.22)	8.78 (4.72)	4.51	2.91e+01
	1.0	21.4	215	147.70	35.5	2.10 (1.41)	9.61 (5.22)	5.26	3.09e+01
r_0^4 (cm^4)	1.5e-03	427.1	4272	4296.30	1.2	3.80e-01 (3.46e-01)	1.80 (1.53)	1.80	6.82
	3.0e-03	301.0	3011	3096.38	1.7	9.01e-01 (6.77e-01)	3.78 (1.24)	2.58	6.34
	1.0e-02	183.5	1836	1949.93	2.7	1.29 (8.92e-01)	5.69 (2.09)	3.22	1.04e+01
	5.0e-02	41.5	416	247.34	21.2	1.93 (1.23)	9.11 (5.56)	4.50	3.25e+01
	1.0	21.4	215	149.38	35.1	2.10 (1.41)	9.61 (5.22)	5.26	3.09e+01
Reynolds number Re	250	450.7	4508	4567.84	1.1	9.49e-01 (6.63e-01)	5.53 (5.70)	2.97	2.91e+01
	300	340.5	3406	3504.47	1.5	1.38 (1.04)	7.23 (5.40)	4.46	2.75e+01
	350	198.7	1988	2127.82	2.5	1.71 (1.02)	8.71 (5.38)	4.12	3.08e+01
	400	132.6	1327	859.06	6.1	1.74 (1.00)	8.66 (5.49)	4.11	3.12e+01
	450	51.3	514	333.92	15.7	2.01 (1.22)	9.85 (5.54)	5.07	3.35e+01

Note: For each *a-priori* model selection criterion C tested, the different 1D-0D thresholds $\gamma_1^C, \ldots, \gamma_P^C$ considered for this arterial model are listed in column 2. For each criterion and each criterion threshold, we report precise values of: total 1D length and total number of 1D computational cells of the hybrid network configuration; mean CPU time per cardiac cycle of the simulation and speed-up with respect to the 1D simulation; mean (with standard deviation between brackets) and maximum RMS relative errors (in %) in both pressure and flow rate in the predicted results with respect to the reference 1D solution.

Figure 2 displays the efficiency plots obtained for the 37-artery network showing CPU times, on the *x*-axis, versus mean and maximum RMS relative errors, on the *y*-axis, in both pressure and flow rate. In each plot, each curve of a different color corresponds to a different criterion tested, while, on each curve, each marker corresponds to a different 1D-0D threshold considered for that parameter. The CPU time axis is inverted: all efficiency curves arise from the common left lower spot, which corresponds to the 1D simulation, for which we have zero errors and maximum CPU time, and merge into the common right upper spot, which corresponds to the 0D simulation, for which we obtain the largest errors and the smallest computational cost. As we move from the 1D to the 0D network, passing through different sets of hybrid configurations, the number of 1D vessels in the network decreases, and so does the total number of 1D computational cells, resulting in an increasing reduction in the computational cost of the simulations and, on the other hand, a progressive increase in pressure and flow errors. By looking at the efficiency plots corresponding to the mean RMS errors (top row of Figure 2), we conclude that, at least for this arterial network, the intravascular volume V_0 (in green) and the vessel compliance C_0 (in violet) can be identified as the most suitable *a-priori* model selection criteria to construct hybrid networks of 1D-0D vessels, since they provide the best trade-off between computational cost of the simulations and accuracy of the results. Indeed, for several thresholds, at least the first 3/4 thresholds for both volume V_0 and compliance C_0, as the CPU times decrease, errors in both pressure and flow rate are not increasing too much, but remain within a reasonable range, still ensuring a good level of accuracy in the predicted results. Volume and compliance efficiency curves are considerably below the curves obtained for all the other model selection criteria, for which the reduction in terms of computational cost is always associated to a more significant increase in the errors magnitude. Mean RMS errors are relevant since they give a general overview of the entire network performance. Moreover, these observations are also confirmed by the efficiency plots corresponding to the maximum RMS errors (bottom row of Figure 2), where intravascular volume and vessel compliance stand again as the most convenient model selection criteria. Since we are looking at the maximum RMS errors over the entire arterial model, the error magnitude is quite higher, especially in the flow rate results, than the mean RMS errors, but the obtained curve trend is very similar to that just described for the mean RMS errors efficiency plots.

The sets of 1D-0D thresholds used for the different *a-priori* model selection criteria and the features of each hybrid network configuration constructed (total 1D length and total number of 1D computational cells) are reported in Table 11. For each model selection criterion and each criterion threshold, these tables also summarize precise values of: average CPU time per cardiac cycle and speed-up with respect to the 1D simulation, measured as the ratio between the CPU times of the 1D and hybrid simulations; mean and maximum RMS relative errors (in percent) in the predicted pressure and flow results, with respect to the reference 1D solution, with indication also of the standard deviation for mean RMS errors. CPU time and error values presented in Table 11 support the analysis and observations from the efficiency plots in Figure 2 discussed above.

Results for the nondimensional coefficient Γ_P, tested as model selection criterion both "from below" and "from above", are reported in Table 12 and efficiency plots corresponding to this parameter are shown in Figure 3 compared to that of the vessel compliance and the intravascular volume. These efficiency plots demonstrate that the nondimensional coefficient Γ_P does not represent a valid and good model selection criterion to construct hybrid networks of vessels, as confirmed also by precise values of CPU times and RMS relative errors detailed in Table 12. Indeed, when adopting this criterion both "from below" and "from above" to create a hybrid configuration of the 37-artery network, its performance is clearly not as good as that of the vessel compliance C_0 and the intravascular volume V_0. In particular, if we look at the mean RMS errors, we observe a steep increase in both pressure and flow errors even with the first thresholds, meaning that also a small gain in terms of CPU time would come at the cost of a significant loss in terms of accuracy. In addition, since according to its definition (43) Γ_P is directly related to volume V_0, but inversely related to the compliance C_0, neither the criterion Γ_P "from below" nor the criterion Γ_P "from above" can provide a unified model selection criterion in which both volume and compliance are embedded.

For this arterial network, the vessel compliance C_0 and the intravascular volume V_0 have been identified as the best *a-priori* model selection criteria to be adopted to construct hybrid network configurations, where a good balance between computational efficiency and accuracy is accomplished. Thus, we look now at some qualitative comparisons between results obtained from the 1D and 0D models and some hybrid configurations of the 37-artery network, generated by using some 1D-0D thresholds either for C_0 or for V_0.

Figure 4 illustrates the computational results obtained for a hybrid configuration of the 37-artery network constructed using the intravascular volume V_0 as model selection criterion with a 1D-0D threshold of $V_0 = 6$ cm^3. The total 1D length of this hybrid configuration, given by the sum of the lengths of the 1D vessels, is reduced from 524.9 cm (the total 1D length of the 1D network) to 177.7 cm; the CPU time required to perform the 1D simulation with mesh-independent results is about 5246.76 s, while the CPU time demanded for the hybrid simulation is considerably reduced to 983.01 s, with a
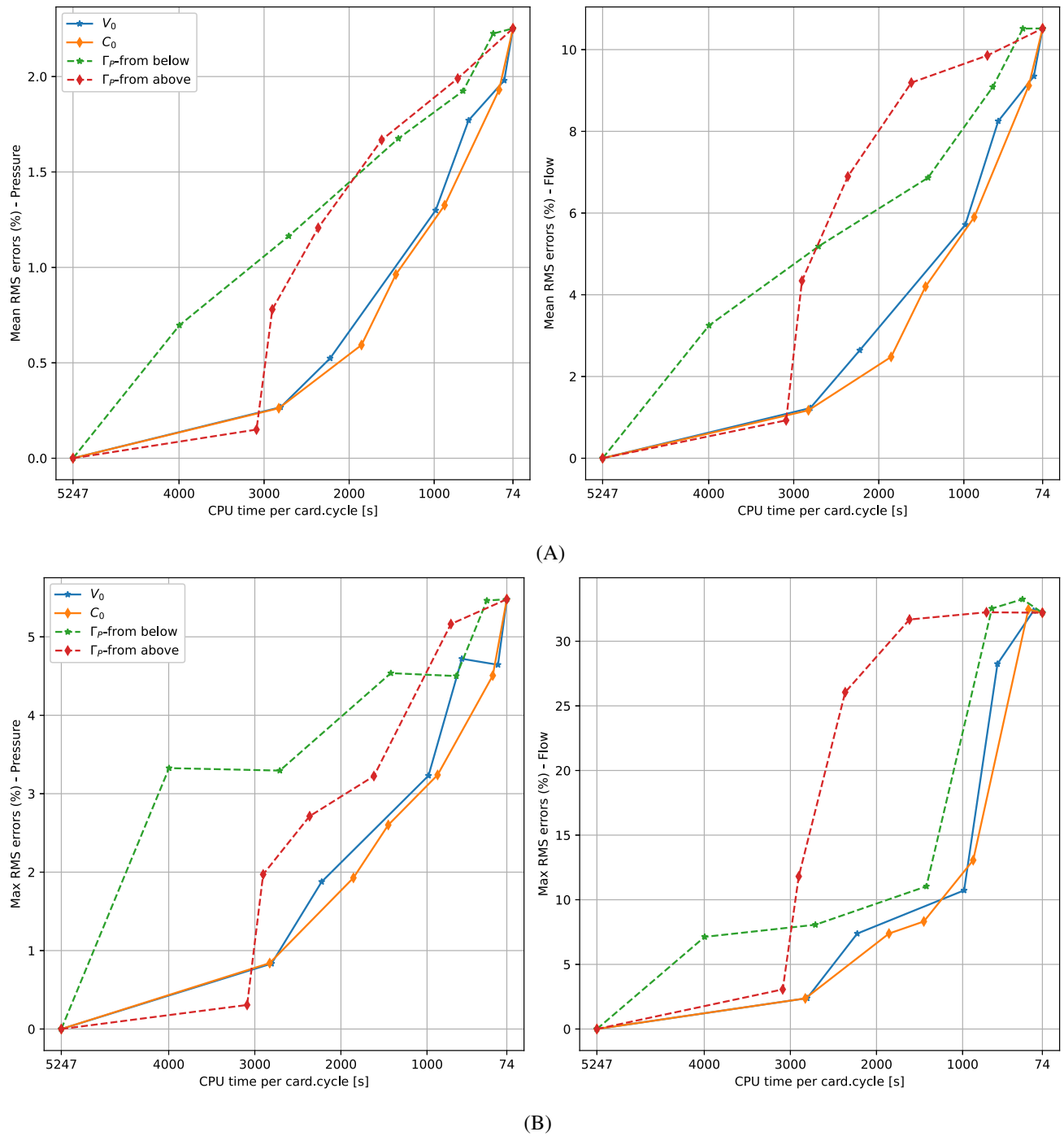
(A)

(B)

FIGURE 3 Efficiency plots generated for the **37-artery network** with CPU time per cardiac cycle versus (A) mean and (B) maximum RMS relative errors for both pressure and flow rate, to assess the performance of the two *a-priori* model selection criteria based on the nondimensional coefficient Γ_P and compare them to the results obtained from the volume and compliance criteria.

speed-up of about 5.3. Clearly, the highest speed-up is obtained with the 0D configuration, which is simulated with a CPU time per cardiac cycle of about 73.92 s, corresponding to a speed-up of 71 times with respect to the 1D simulation, but with a much more significant loss in terms of accuracy of the solution. Indeed, in the results for the hybrid configuration, mean RMS errors are around 1.3% for pressure and 5.7% for flow rate, while, in the 0D network, they are almost doubled with values around 2.3% for pressure and 10.5% for flow rate; similarly, maximum RMS errors remain smaller than 3.5% for pressure and smaller than 10% for flow rate in the hybrid network configuration, while, for the 0D results, maximum errors rise up to almost 5.5% for pressure and 32% for flow rate. In Figure 4, computational results obtained from the 1D,

TABLE 12 Results obtained by applying the proposed adaptive model selection strategy to the **37-artery network**.

Criterion C	Thresh. γ^C	Tot.1D length (cm)	Tot.1D cells	Mean CPU time (s)	Speed-up wrt 1D	Mean ε_P^{RMS} (%) (std.dev)	Mean ε_Q^{RMS} (%) (std.dev)	Max ε_P^{RMS} (%)	Max ε_Q^{RMS} (%)
Γ_P "from below"	1.2e+03	393.2	3933	3995.64	1.3	6.96e-01 (7.19e-01)	3.25 (1.69)	3.33	7.13
	1.5e+03	259.9	2600	2709.32	1.9	1.16 (8.71e-01)	5.18 (1.58)	3.29	8.07
	2.5e+03	129.0	1291	1420.85	3.7	1.68 (1.29)	6.86 (2.19)	4.54	1.10e+01
	5.5e+03	46.6	467	660.61	7.9	1.92 (1.23)	9.08 (5.5)	4.50	3.25e+01
	1.0e+04	13.4	135	305.64	17.2	2.23 (1.41)	1.05e+01 (5.36)	5.46	3.32e+01
Γ_P "from above"	1.0e+04	511.5	5115	3089.11	1.7	1.50e-01 (6.52e-02)	9.27e-01 (4.86e-01)	3.07e-01	3.07
	5.5e+03	478.3	4783	2903.13	1.8	7.80e-01 (5.18e-01)	4.34 (1.99)	1.97	1.18e+01
	2.5e+03	395.9	3959	2363.64	2.2	1.21 (6.82e-01)	6.90 (5.11)	2.71	2.61e+01
	1.5e+03	265.0	2650	1617.22	3.2	1.67 (7.47e-01)	9.19 (5.51)	3.22	3.17e+01
	1.2e+03	131.7	1317	723.17	7.3	1.99 (1.13)	9.86 (5.36)	5.16	3.22e+01

Note: Continuation of Table 11.

0D and hybrid configurations of the 37-artery network are compared for two vessels: the left iliac-femoral I (vess. 31), which is a 1D vessel in the hybrid network, and the left ulnar (vess. 14), which is a 0D vessel in the hybrid network.

The computational results displayed in Figure 5 are obtained from a hybrid network configuration constructed using the vessel compliance C_0 a model selection criterion with a 1D-0D threshold of $C_0 = 1.5 \cdot 10^{-5}$ cm^5/dyne. Here, the total 1D length of the hybrid configuration is 158.2 cm and the CPU time demanded to perform the simulation is about 877.42 s, with a speed-up of 6 times with respect to the 1D simulation. As expected, the improvement in terms of computational cost is not as relevant as for the 0D network, but this is balanced by the good level of accuracy preserved in the predicted results: in the results for the hybrid network, mean RMS errors are around 1.3% for pressure and 5.9% for flow rate, maximum RMS errors are smaller than 3.5% for pressure and smaller than 13.5% for flow rate. In Figure 5, the computational results obtained from this hybrid configuration of the 37-artery network are compared to 1D and 0D results for two vessels: the abdominal aorta I (vess. 23), which is a 1D vessel in the hybrid network, and the right anterior tibial (vess. 34), which is a 0D vessel in the hybrid network.

As confirmed by the computed CPU times and errors, Figures 4 and 5 show that both hybrid configurations are still able to produce good approximations of pressure and flow waveforms and that the essential features, shape, and amplitude, of these waves are well-captured, including the systolic pressure peak. Even if some accuracy is lost with respect to the 1D results, a great improvement is obtained with respect to the 0D results. In fact, when compared to the reference 1D results, in the 0D results we frequently observe oscillations that are amplified and/or delayed, curve peaks that are under-/over-estimated in both pressure and flow waveforms. These phenomena are significantly reduced and corrected in the results produced by the hybrid network configuration. This analysis is valid for both 1D and 0D vessels of the two hybrid networks; in particular, the nonlinearity included in the 0D models, through the nonlinear pressure-area relation and the nonlinear parameters L and R, as demonstrated in Reference 27, strongly improves the ability of these 0D models to approximate pressure and flow waveforms in 0D vessels. Overall, even if the differences are not negligible, there is good agreement between the results predicted by the hybrid network and the reference 1D results, and the reasonable loss in terms of accuracy is balanced by the considerable improvement in terms of computational efficiency.

We observe that, in both the hybrid networks considered, the one obtained with the volume threshold of $V_0 = 6$ cm^3 and the other constructed with the compliance threshold of $C_0 = 1.5 \cdot 10^{-5}$ cm^5/dyne, the entire aorta is 1D, except for just one very short aortic segment, the abdominal aorta III, which is 0D. Hence, the very good agreement of these results with the reference, 1D results is likely ensured also by the fact that, with these model selection criteria and these specific 1D-0D thresholds, the main aortic vessels are kept 1D and thus, pressure and flow distributions in these vessels are still reproduced with a very good level of accuracy. When applying this methodology to more complex networks of vessels, specific vessels or portions of the network, like the aortic trunk, could be enforced to be 1D and the chosen *a-priori* model selection criteria would be then applied to all the other vessels. This was not done here, in order to blindly test the performance of the different model selection criteria.
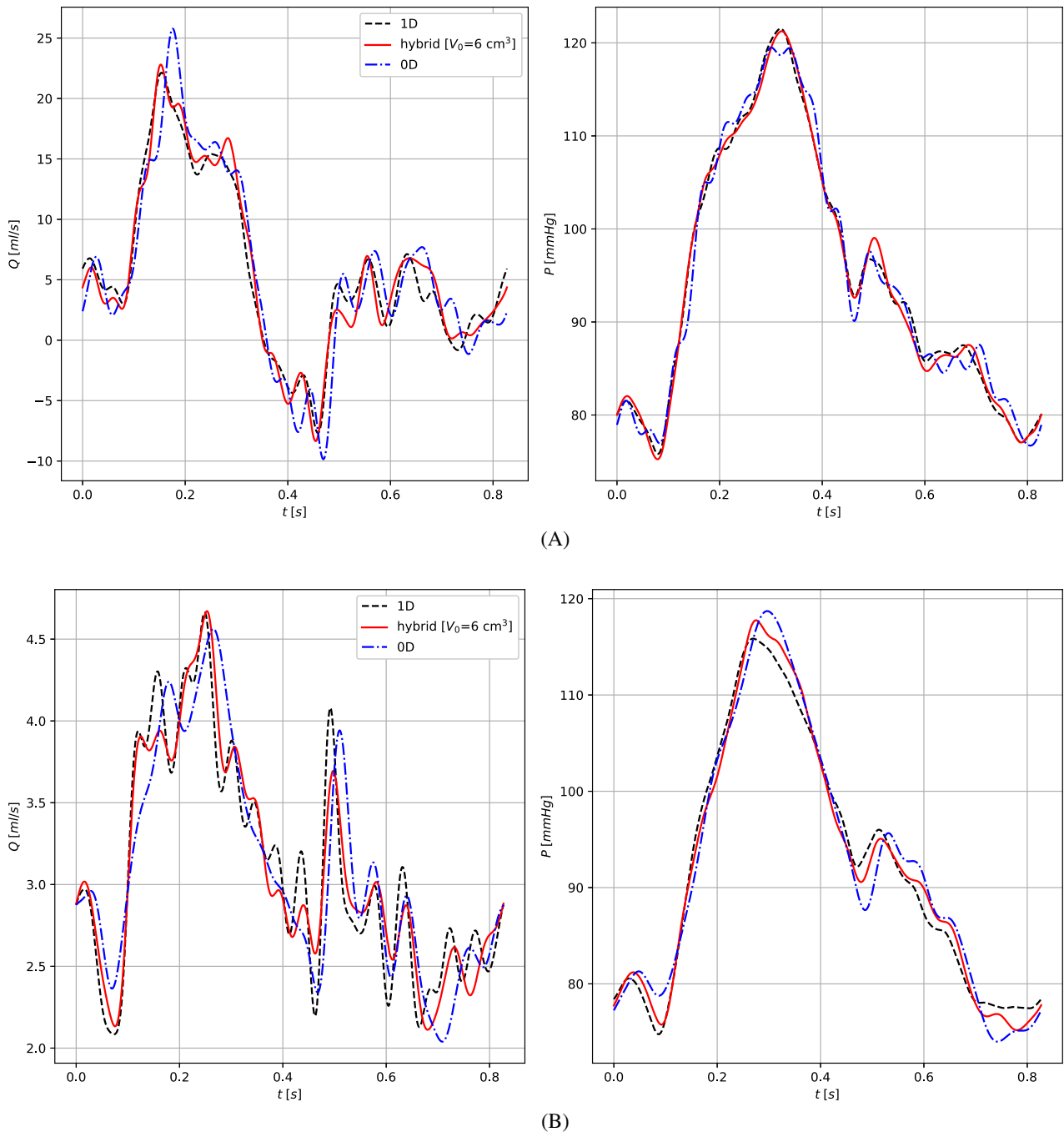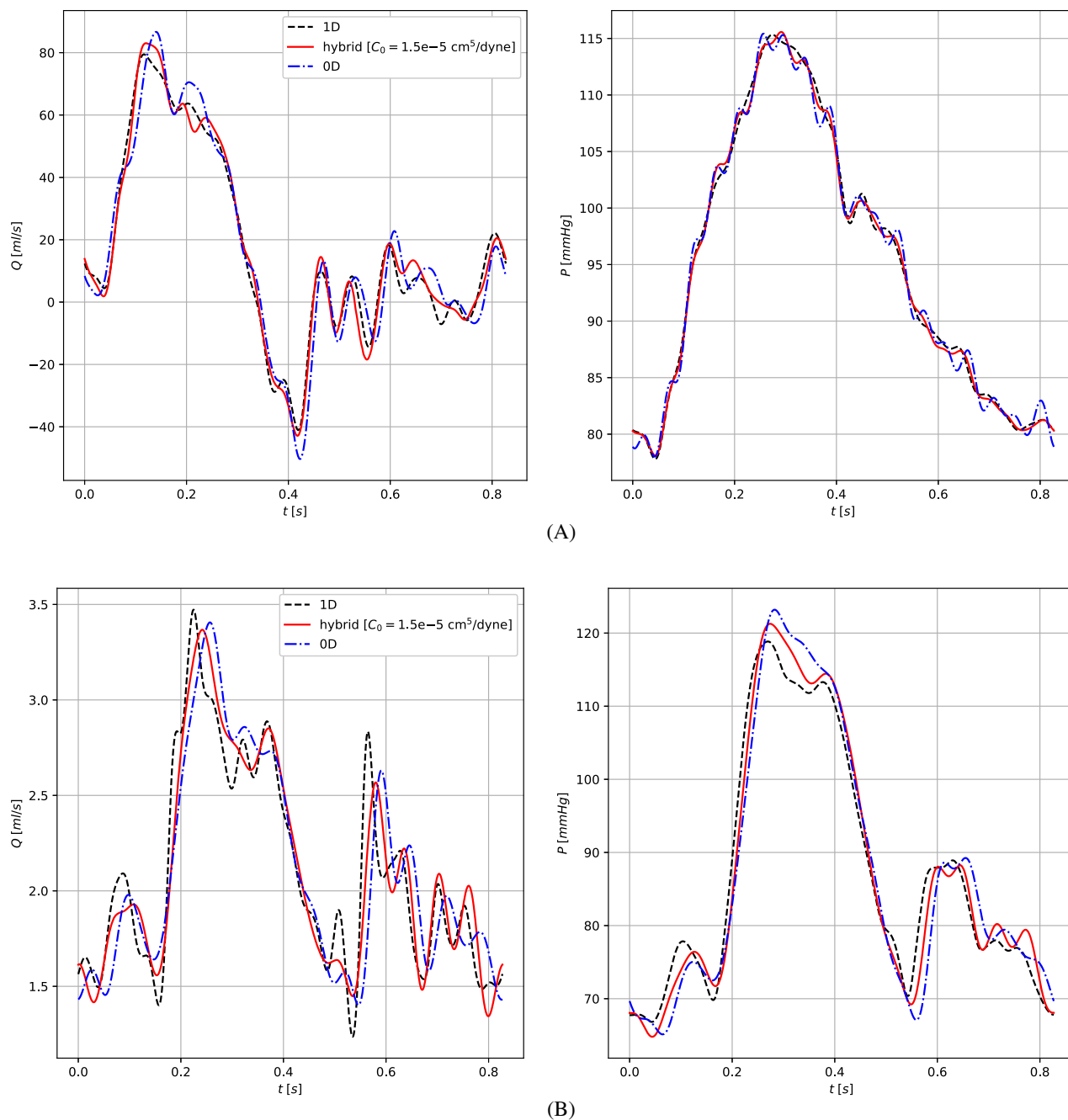
FIGURE 4 Qualitative comparison between computational results for flow rate and pressure obtained from the 1D (dashed black line), the 0D (blue dashed-dotted line), and a hybrid (red continuous line) configuration of the **37-artery network**, where the last is constructed using the volume V_0 as model selection criterion, with a 1D-0D threshold of $V_0 = 6$ cm³. (A) Left iliac-femoral I (1D); (B) left ulnar (0D)

4.2.2 | Reduced ADAN56 model

The second arterial network to which we apply the proposed adaptive model selection strategy is a reduced version of the anatomically detailed arterial network (ADAN) model developed by Blanco et al..[3,14] This model, hereafter referred to as ADAN56 model, was presented in Reference 33 and contains the largest 56 vessels of the human arterial system.

At the inlet of the aorta, a periodic inflow boundary condition is prescribed, whose inflow signal is given in the Supplementary Information of Reference 33; terminal vessels are coupled to *RCR* Windkessel models. In the tube law (3), or equivalently (15) for 0D vessels, we set $P_0 = P_d = 10^5$ dyne/cm² and $A_0 = A_d$; in each vessel, zero flow rate, diastolic

FIGURE 5 Qualitative comparison between computational results for flow rate and pressure obtained from the 1D (dashed black line), the 0D (blue dashed-dotted line), and a hybrid (red continuous line) configuration of the **37-artery network**, where the last is constructed using the compliance C_0 as model selection criterion, with a 1D-0D threshold of $C_0 = 1.5 \cdot 10^{-5}$ cm^5/dyne. (A) Abdominal aorta I (1D); (B) right anterior tibial (0D)

pressure P_d and corresponding cross-sectional area A_d are imposed as initial conditions. Main model parameters for this arterial network are given in Table 13, while the full model parametrization is included in Reference 33. Also here, as for the 37-artery network, we do not consider vessel tapering, but each vessel is characterized by a constant reference radius r_0.

Figure 6 shows the efficiency plots obtained for the ADAN56 model displaying CPU times, on the inverted x-axis, versus mean and maximum RMS relative errors, on the y-axis, in both pressure and flow rate results. By examining the efficiency plots corresponding to the mean RMS errors (top row of Figure 6), we conclude that, as for the 37-artery network, also for this arterial model the intravascular volume V_0 (in green) and the vessel compliance C_0 (in violet) provide

T A B L E 13 Main parameters of the reduced ADAN56 model.

Property	Value
Blood density, ρ	1.040 g/cm^3
Blood viscosity, μ	0.04 dyne s/cm^2
Velocity profile order, ζ	2
Young's modulus, E	2.25·10^6 dyne/cm^2
Diastolic pressure, P_d	10^5 dyne/cm^2
External pressure, p_{ext}	0
Outflow pressure, P_{out}	0

a very good trade-off between computational cost of the simulations and errors in the predicted results, thus supporting the choice of these two criteria as the most suitable *a-priori* model selection criteria to construct hybrid networks of vessels. Volume and compliance efficiency curves show that several increasing 1D-0D thresholds of both parameters produce hybrid configurations of ADAN56 model which can be simulated at a lower computational cost, but still preserving a good level of accuracy in the solution and with small RMS errors. These observations are also confirmed by the efficiency plots corresponding to the maximum RMS errors (bottom row of Figure 6), where, even if not as clearly as for the 37-artery network, volume V_0 and compliance C_0 can still be distinguished among the other criteria for their quite satisfactory job. It is interesting to note that, for this arterial network, also the vessel radius r_0 and its third and fourth power, r_0^3 and r_0^4, respectively, turn out to be good model selection criteria, in the sense that their performance in terms of trade-off between computational efficiency and accuracy is comparable to that of V_0 and C_0. This was not observed for the 37-artery network, and this is not surprising given that they are two very different networks, especially with ADAN56 model based on solid geometric and anatomic considerations. On the other hand, length, mean flow rate, and Reynolds number appear to be the criteria with the worst performance, since the gain obtained in terms of computational efficiency comes always with a significant loss in terms of accuracy of the solution, with errors that considerably increase in both flow rate and pressure. However, since we are looking for general criteria that can be applied to any network of vessels, we conclude that the intravascular volume V_0 and vessel compliance C_0 can be chosen as *a-priori* model selection criteria defining the adaptive model selection strategy proposed in Section 3.4 to construct hybrid networks of 1D-0D vessels.

The sets of 1D-0D thresholds used for the different *a-priori* model selection criteria and the features of each hybrid network configuration constructed (total 1D length and total number of 1D computational cells) are summarized in Table 14, together with precise values of average CPU times per cardiac cycle, mean (with standard deviation) and maximum RMS relative errors (in percent). Once again, also for this arterial model, CPU time and error values reported in Table 14 validate the observations and outcomes from the efficiency plots presented in Figure 6 discussed above.

Results and efficiency plots for the nondimensional coefficient Γ_P, tested as model selection criterion both "from below" and "from above", are presented in Table 15) and in Figure 7, respectively. Analysis and considerations on the performance of the parameter Γ_P and its use as *a-priori* model selection criterion "from below" and/or "from above" are the same as for the 37-artery network.

Figures 8 and 9 depict the computational results obtained for a hybrid configuration of ADAN56 model constructed using the intravascular volume V_0 as model selection criterion with a 1D-0D threshold of $V_0 = 3.5$ cm^3. The total 1D length of the 1D network is 888.874 cm and in the hybrid configuration is reduced to 161.583 cm. The CPU times demanded to perform the 1D and 0D simulations are about 5382.75 and 201.17 s, respectively, with a 1D to 0D computational time ratio of about 26.8; on the other hand, the CPU time required by the hybrid network configuration is around 935.63 s, with a speed-up of almost 6 times, which is a quite remarkable improvement. A good level of accuracy of the solution is also preserved: in the results for the hybrid configuration, mean RMS errors are around 1.6% for pressure and 4.7% for flow rate, while, in the 0D network, they are doubled with values around 3.2% for pressure and 9.5% for flow rate. Similarly, maximum RMS errors remain smaller than 6% for pressure and smaller than 16% for flow rate in the hybrid network configuration, while, for the 0D results, maximum errors jump up to almost 12% for pressure and 38% for flow rate. Computational results obtained from the 1D, 0D and hybrid configurations of ADAN56 model are compared in Figure 8 for the aortic arch IV (vess. 19a) and the abdominal aorta V (vess. 47), which are both 1D vessels in the hybrid network, and in Figure 9 for the right internal iliac (vess. 51) and the right posterior tibial (vess. 55c), which are both 0D vessels in the hybrid network.
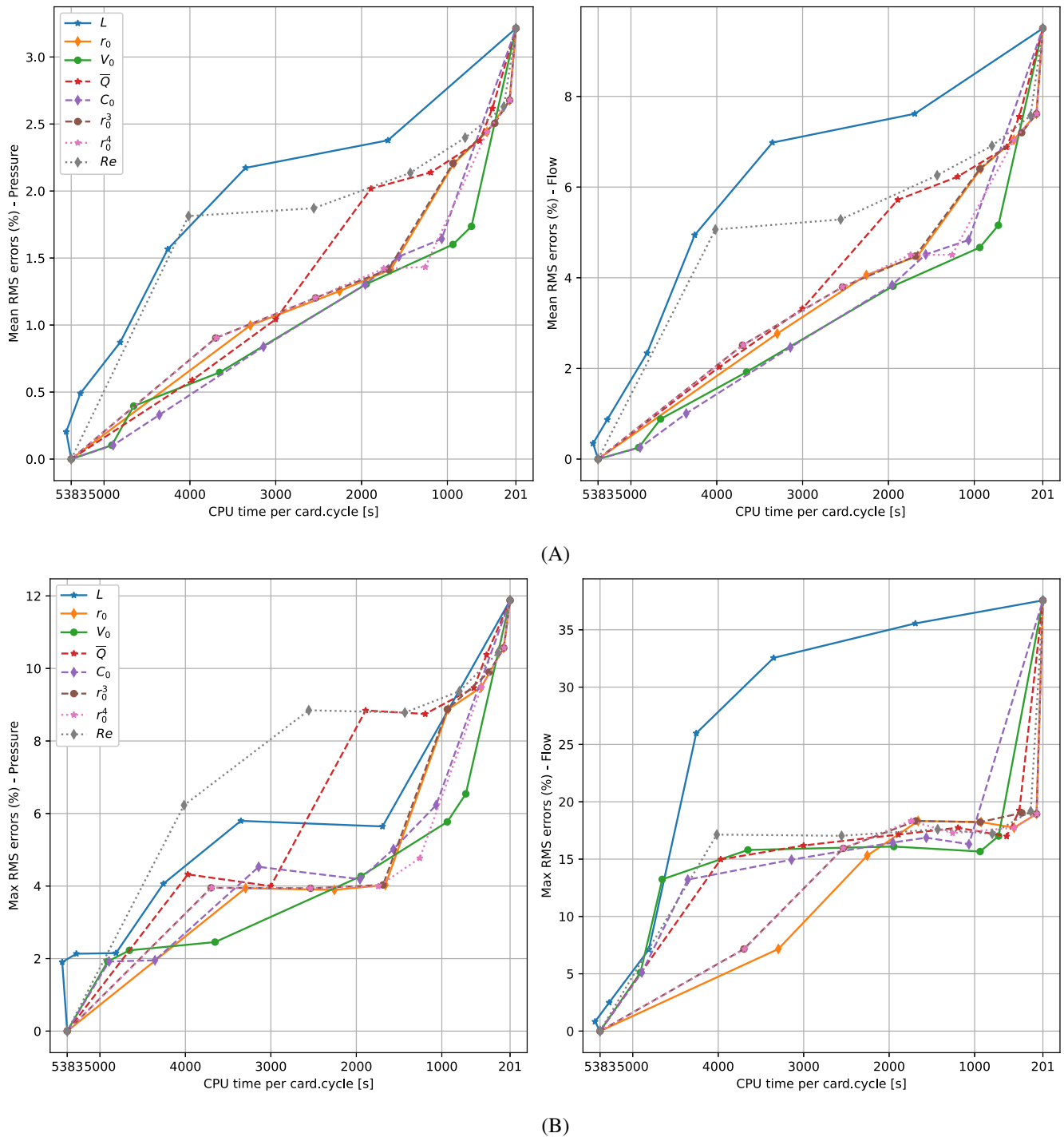
FIGURE 6 Efficiency plots generated for **ADAN56 model** with CPU time per cardiac cycle versus (A) mean and (B) maximum RMS relative errors for both pressure and flow rate, to assess and compare the performance of the different *a-priori* model selection criteria tested.

The computational results displayed in Figures 10 and 11 are obtained from a hybrid network configuration constructed using the vessel compliance C_0 a model selection criterion with a 1D-0D threshold of $C_0 = 7 \cdot 10^{-6}$ cm^5/dyne. The total 1D length of the hybrid configuration is 337.697 cm and the CPU time required by the simulation is about 1957.06 s, with a speed-up of around 2.8 times with respect to the 1D simulation. Here, the speed-up is moderate with respect to the previous hybrid configuration, but still the accuracy preserved in the predicted results is quite satisfactory: in the results for the hybrid network, mean RMS errors are around 1.3% for pressure and 3.8% for flow rate, while maximum RMS errors are smaller than 4.5% for pressure and smaller than 16.5% for flow rate. Results produced by the different

TABLE 14 Results obtained by applying the proposed adaptive model selection strategy to the **ADAN56 model**.

Criterion C	Thresh. χ^C	Tot.1D length (cm)	Tot.1D cells	Mean CPU time (s)	Speed-up wrt 1D	Mean ε_P^{RMS} (%) (std.dev)	Mean ε_Q^{RMS} (%) (std.dev)	Max ε_P^{RMS} (%)	Max ε_Q^{RMS} (%)
1D	-	888.874	8931	5382.75	-	-	-	-	-
0D	-	0.0	0	201.17	26.8	3.21 (2.72)	9.50 (5.81)	1.19e+01	3.76e-01
Length l (cm)	1.0	881.994	8859	5441.23	1.0	2.04e-01 (2.68e-01)	3.45e-01 (1.98e-01)	1.90	8.27e-01
	4.0	845.875	8492	5275.82	1.0	4.91e-01 (4.38e-01)	8.70e-01 (5.84e-01)	2.13	2.49
	7.0	788.765	7914	4812.49	1.1	8.71e-01 (5.49e-01)	2.34 (1.08)	2.15	7.11
	12.0	704.901	7069	4257.26	1.3	1.57 (1.03)	4.94 (3.12)	4.06	2.60e+01
	20.0	547.776	5489	3351.54	1.6	2.17 (1.46)	6.98 (4.29)	5.80	3.26e+01
	30.0	278.854	2792	1693.60	3.2	2.38 (1.37)	7.62 (4.50)	5.64	3.56e+01
Radius r_0 (cm)	0.14	583.651	5873	3295.85	1.6	9.98e-01 (9.07e-01)	2.77 (1.49)	3.94	7.17
	0.2	399.774	4028	2256.57	2.4	1.25 (9.29e-01)	4.06 (2.97)	3.89	1.53e+01
	0.25	291.064	2934	1660.08	3.2	1.41 (1.03)	4.48 (3.35)	4.03	1.83e+01
	0.3	146.926	1485	924.05	5.8	2.21 (2.05)	6.40 (4.04)	8.88	1.82e+01
	0.4	68.706	697	538.6	10.0	2.44 (2.18)	7.04 (4.14)	9.48	1.77e+01
	0.8	29.427	298	276.03	19.5	2.68 (2.43)	7.62 (4.61)	1.06e+01	1.89e+01
Volume V_0 (cm³)	0.5	831.403	8353	4909.36	1.1	1.03e-01 (3.32e-01)	2.54e-01 (8.50e-01)	1.92	5.11
	1.0	785.323	7887	4655.03	1.2	3.96e-01 (4.93e-01)	8.83e-01 (1.65)	2.23	1.32e+01
	1.5	618.008	6206	3653.06	1.5	6.47e-01 (5.65e-01)	1.92 (2.85)	2.46	1.58e+01
	2.0	335.966	3379	1945.62	2.8	1.31 (9.22e-01)	3.82 (3.02)	4.27	1.61e+01
	3.5	161.583	1626	935.63	5.8	1.60 (1.20)	4.67 (3.30)	5.77	1.57e+01
	6.0	119.544	1201	719.10	7.5	1.74 (1.33)	5.16 (3.44)	6.54	1.70e+01
Compl. C_0 (cm⁵/dyne)	1.0e-06	831.403	8353	4893.75	1.1	1.03e-01 (3.32e-01)	2.54e-01 (8.50e-01)	1.92	5.11
	3.0e-06	733.734	7371	4356.27	1.2	3.29e-01 (3.99e-01)	1.01 (2.07)	1.95	1.32e+01
	4.0e-06	530.066	5326	3142.61	1.7	8.38e-01 (8.31e-01)	2.46 (3.06)	4.53	1.49e+01
	7.0e-06	337.697	3397	1957.06	2.8	1.30 (9.21e-01)	3.84 (3.02)	4.19	1.64e+01
	1.2e-05	185.900	1871	1065.98	5.0	1.51 (1.08)	4.51 (3.32)	5.02	1.69e+01
	2.0e-05	138.415	1392	820.45	6.6	1.64 (1.28)	4.83 (3.35)	6.23	1.63e+01

TABLE 14 (Continued)

Criterion C	Thresh. γ^C	Tot.1D length (cm)	Tot.1D cells	Mean CPU time (s)	Speed-up wrt 1D	Mean ε_P^{RMS} (%) (std.dev)	Mean ε_Q^{RMS} (%) (std.dev)	Max ε_P^{RMS} (%)	Max ε_Q^{RMS} (%)
Mean flow $\overline{Q}$ (ml/s)	1.0	676.814	6804	3971.03	1.4	5.90e-01 (7.94e-01)	2.03 (3.10)	4.32	1.50e+01
	2.0	517.434	5205	3000.82	1.8	1.04 (9.35e-01)	3.32 (3.09)	4.00	1.62e+01
	3.0	323.937	3265	1891.16	2.8	2.02 (2.06)	5.72 (4.08)	8.84	1.71e+01
	7.0	192.820	1944	1193.76	4.5	2.14 (2.03)	6.23 (3.99)	8.75	1.77e+01
	12.0	91.472	925	625.26	8.6	2.37 (2.20)	6.88 (4.10)	9.46	1.70e+01
	40.0	32.781	333	348.00	15.5	2.62 (2.39)	7.55 (4.57)	1.04e+01	1.92e+01
r_0^3 (cm^3)	2.5e-03	644.828	6485	3699.25	1.5	9.04e-01 (9.29e-01)	2.51 (1.63)	3.95	7.16
	5.0e-03	444.396	4476	2535.65	2.1	1.20 (9.27e-01)	3.80 (2.94)	3.94	1.59e+01
	1.5e-02	291.064	2934	1687.63	3.2	1.41 (1.03)	4.48 (3.35)	4.03	1.83e+01
	2.5e-02	146.926	1485	935.12	5.8	2.21 (2.05)	6.40 (4.04)	8.88	1.82e+01
	8.0e-02	48.721	495	447.38	12.0	2.51 (2.28)	7.20 (4.35)	9.90	1.90e+01
	5.0e-01	29.427	298	274.40	19.7	2.68 (2.43)	7.62 (4.61)	1.06e+01	1.89e+01
r_0^4 (cm^4)	3.5e-04	644.828	6485	3691.79	1.5	9.04e-01 (9.29e-01)	2.51 (1.63)	3.95	7.16
	6.0e-04	444.396	4476	2537.48	2.1	1.20 (9.27e-01)	3.80 (2.94)	3.94	1.59e+01
	3.0e-03	300.056	3026	1742.58	3.1	1.42 (1.03)	4.51 (3.36)	3.99	1.83e+01
	7.0e-03	210.784	2125	1257.52	4.3	1.43 (1.04)	4.50 (3.31)	4.80	1.73e+01
	3.0e-02	68.706	697	536.05	10.0	2.44 (2.18)	7.04 (4.14)	9.48	1.77e+01
	5.0e-01	29.427	298	271.89	19.8	2.68 (2.43)	7.62 (4.61)	1.06e+01	1.89e+01
Reynolds number Re	100	672.184	6755	4016.17	1.3	1.81 (1.80)	5.06 (3.86)	6.23	1.71e+01
	200	428.294	4309	2556.33	2.1	1.87 (2.11)	5.29 (4.31)	8.85	1.70e+01
	300	233.790	2355	1432.08	3.8	2.14 (2.02)	6.26 (3.94)	8.78	1.76e+01
	500	112.775	1138	793.73	6.8	2.40 (2.14)	6.91 (4.07)	9.37	1.72e+01
	900	31.583	321	343.46	15.7	2.63 (2.41)	7.57 (4.58)	1.04e+01	1.92e+01

Note: For each C, the different 1D-0D thresholds $\gamma_1^C, \ldots, \gamma_P^C$ considered for this arterial model are listed in column 2. For each criterion and each criterion threshold, we report precise values of: total 1D length and total number of 1D computational cells of the hybrid network configuration; mean CPU time per cardiac cycle of the simulation and speed-up with respect to the 1D simulation; mean (with standard deviation between brackets) and maximum RMS relative errors (in %) in both pressure and flow rate in the predicted results with respect to the reference 1D solution.

TABLE 15 Results obtained by applying the proposed adaptive model selection strategy to the **ADAN56 model**.

Criterion C	Thresh. γ^C	Tot.1D length (cm)	Tot.1D cells	Mean CPU time (s)	Speed-up wrt 1D	Mean ε_P^{RMS} (%) (std.dev)	Mean ε_Q^{RMS} (%) (std.dev)	Max ε_P^{RMS}(%)	Max ε_Q^{RMS}(%)
Γ_P "from below"	5.0e+02	637.180	6410	3890.71	1.4	1.02 (8.79e-01)	3.29 (2.17)	4.46	9.52
	1.2e+03	368.513	3714	2383.80	2.3	1.53 (1.11)	4.75 (2.49)	5.37	1.67e+01
	1.8e+03	216.016	2181	1552.66	3.5	2.74 (2.32)	8.10 (4.35)	1.03e+01	2.44e+01
	4.0e+03	137.147	1385	1082.76	5.0	2.96 (2.67)	8.73 (5.04)	1.15e+01	2.99e+01
	1.0e+04	103.401	1043	855.10	6.3	3.08 (2.71)	9.01 (5.08)	1.17e+01	2.89e+01
	1.6e+04	24.199	246	348.43	15.5	3.19 (2.70)	9.32 (5.31)	1.18e+01	2.89e+01
Γ_P "from above"	1.6e+04	864.675	8685	5330.20	1.0	1.13e-01 (1.77e-01)	4.75e-01 (1.44)	1.34	1.27e+01
	1.0e+04	785.473	7888	4891.78	1.1	3.28e-01 (4.88e-01)	1.33 (3.17)	2.42	1.58e+01
	4.0e+03	751.727	7546	4553.05	1.2	6.11e-01 (4.37e-01)	2.16 (3.06)	2.41	1.57e+01
	1.8e+03	672.858	6750	4133.75	1.3	1.14 (8.40e-01)	3.57 (3.42)	3.11	1.80e+01
	1.2e+03	520.362	5217	3224.80	1.7	2.70 (2.33)	7.98 (4.76)	8.74	2.55e+01
	5.0e+02	251.694	2521	1546.75	3.5	3.06 (2.73)	8.86 (5.44)	1.22e+01	3.43e+01

Note: Continuation of Table 14.

network configurations are compared in Figure 10 for the abdominal aorta III (vess. 43) and the left popliteal I (vess. 59 b), which are both 1D vessels in the hybrid network, and in Figure 11 for the right radial (vess. 8) and the right anterior tibial (vess. 4), which are both 0D vessels in the hybrid network.

In accordance with computed CPU times and errors, from Figures 8–11 we conclude that, in the two hybrid configurations of ADAN56 model considered, pressure and flow profiles are reproduced with a very good level of accuracy and agreement with the reference 1D results, in both 1D and 0D vessels. Overall, shape and amplitude of pressure and flow waveforms are well-approximated, preserving all their characteristic features. The evident delay of both pressure and flow waveforms, observed in certain 0D vessels of the 0D configuration, with respect to the 1D reference waves, is almost absent in the results obtained using the hybrid configuration (right anterior tibial in Figure 9, left popliteal I in Figure 10, right anterior tibial in Figure 11, for instance). In these results, flow and pressure systolic peaks are very well-captured also in the 0D vessels, with a considerable improvement with respect to the 0D results, which, in general, present larger over-/under-estimated systolic peaks (abdominal aorta V in Figure 8, right radial and right anterior tibial in Figure 11, for instance). Furthermore, amplified or shifted wave oscillations are observed in the 0D results when compared to those obtained from the hybrid network, with respect to the reference 1D solution (aortic arch IV and abdominal aorta V in Figure 8, right internal iliac in Figure 9, abdominal aorta III in Figure 10, for instance).

Remark 3. A feature of ADAN model is that, in the purely elastic case where viscoelastic properties of vessel walls are neglected, when refining the mesh to obtain mesh-independent results, very small new waves arise in the solutions, in the pressure and flow waveforms, which are not spurious oscillations. In the hybrid network configurations of ADAN56 model considered so far, the new small waves that are observed may be also generated by the wave reflection due to the strong interaction between 1D and 0D models.

Remark 4. For both arterial models considered, the characteristic mesh spacing for 1D vessels was set to $\Delta x_{max} = 1$ mm, to ensure the mesh independence of the 1D results. The very fine mesh size also restricts the global time step used to solve the entire network, thus contributing to increase the computational cost of the simulations.

4.3 | On the validity of 1D junction/bifurcation models

The flow at a junction/bifurcation of two or more vessels is intrinsically three-dimensional and local flow details can be reproduced only using a local 3D description of flow. However, in the present work, as well as, more generally, in
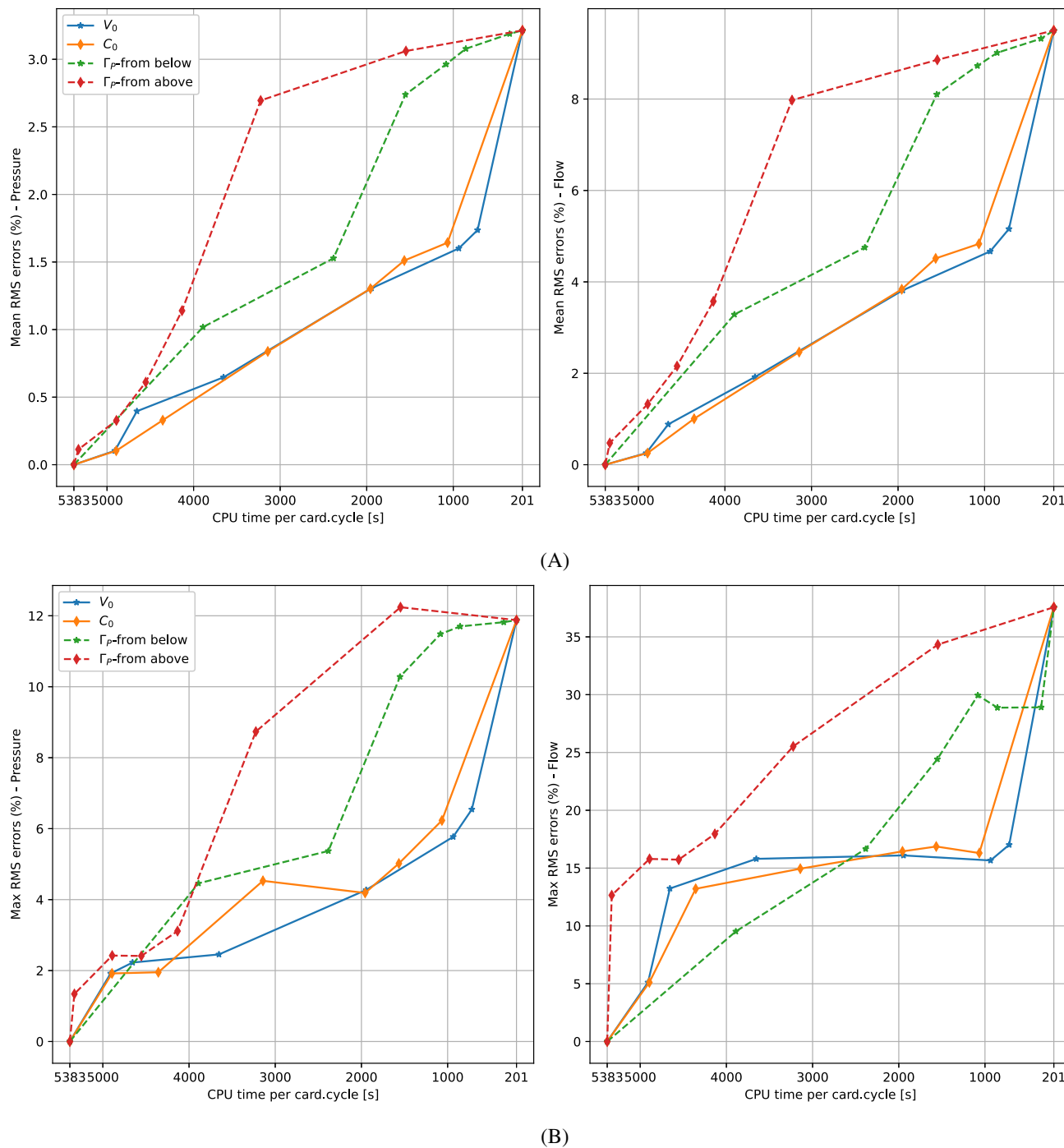
FIGURE 7 Efficiency plots generated for **ADAN56 model** with CPU time per cardiac cycle versus (A) mean and (B) maximum RMS relative errors for both pressure and flow rate, to assess the performance of the two *a-priori* model selection criteria based on the nondimensional coefficient Γ_P and compare them to the results obtained from the volume and compliance criteria.

the one-dimensional blood flow modeling framework, the focus is on (i) correctly describing flow splitting and wave propagation and (ii) preserving relevant quantities, such as mass and total pressure, at each junction of a network, rather than resolving the local 3D flow dynamics. In fact, by adopting a 1D junction model as the one illustrated in Section 2.3.1, the 1D coupling of vessels is modeled and solved in a way that mass and total pressure are preserved at each junction and wave propagation phenomena are reproduced throughout the entire network, even if the local flow dynamics is simplified. This approach is suitable when the local 3D flow details at junctions are less relevant than accounting for wave propagation phenomena across the vascular network, Furthermore, it is worth noting that adopting 3D models for
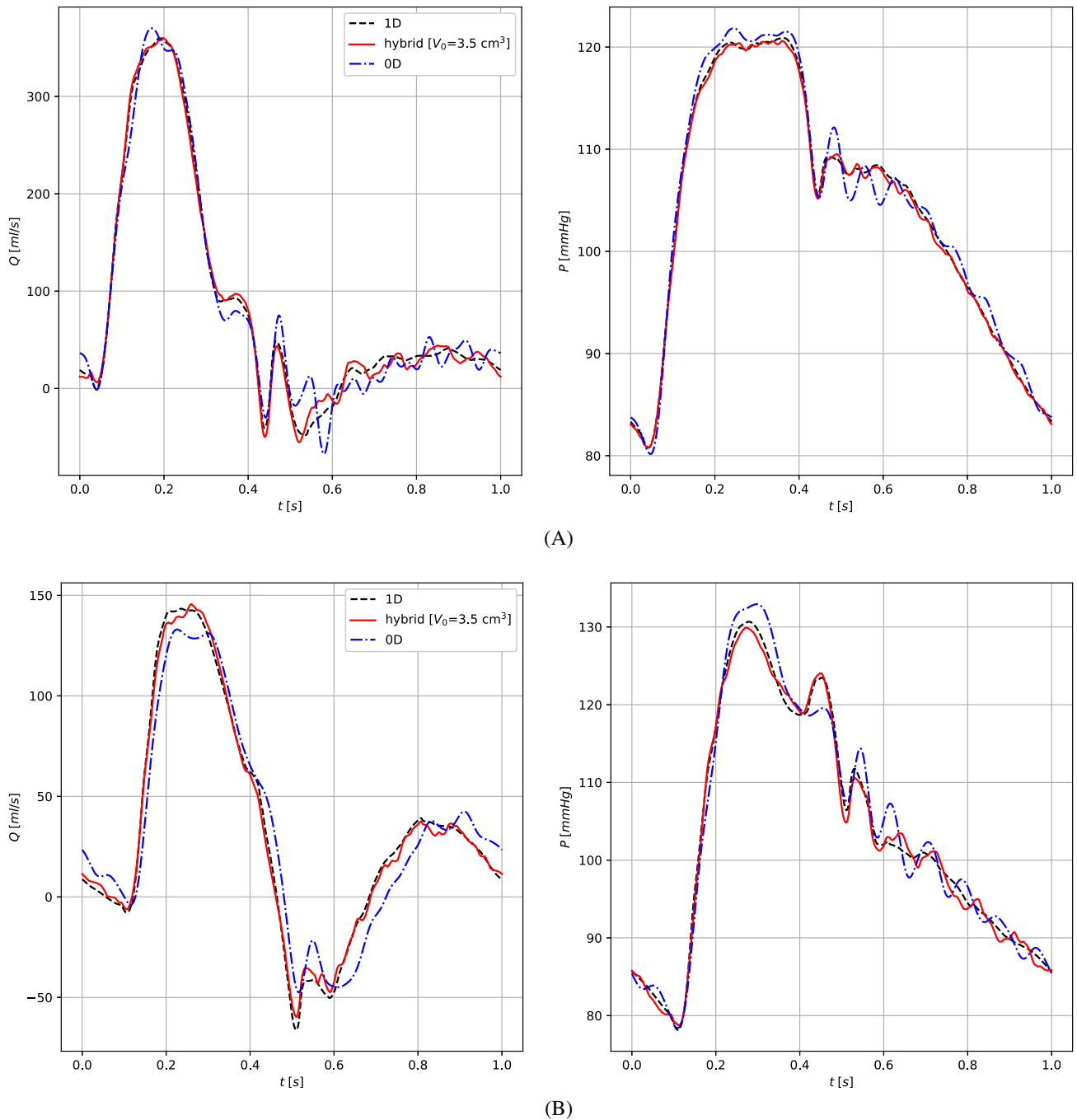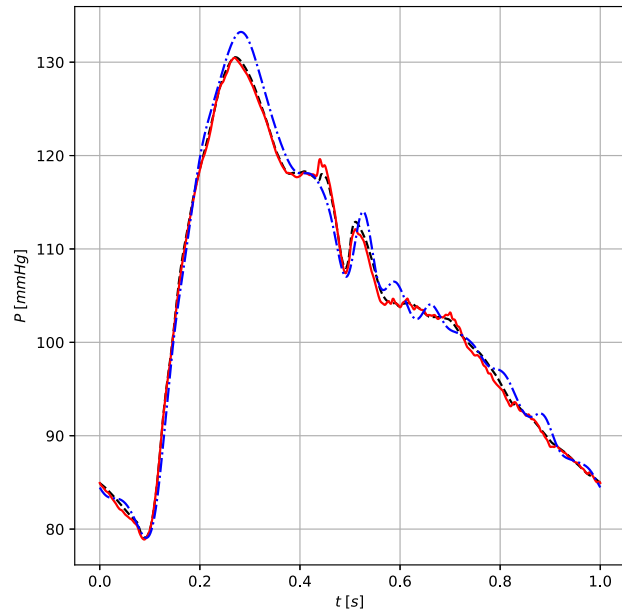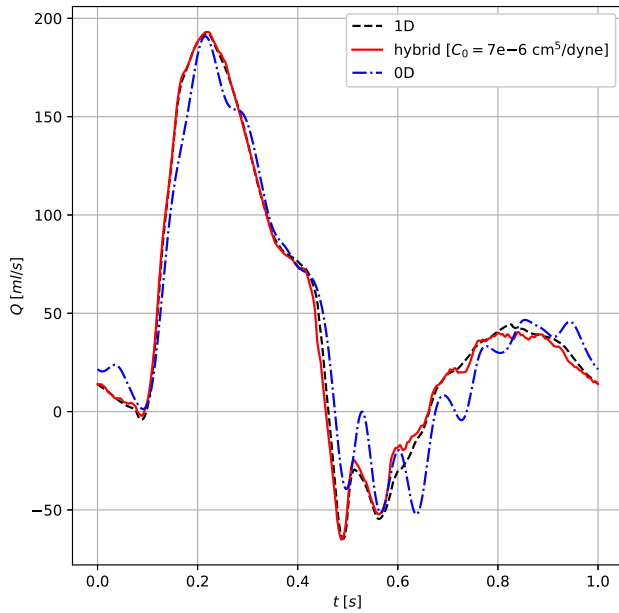
FIGURE 8 Qualitative comparison between computational results for flow rate and pressure obtained from the 1D (dashed black line), the 0D (blue dashed-dotted line), and a hybrid (red continuous line) configuration of **ADAN56 model**, where the last is constructed using the volume V_0 as model selection criterion, with a 1D-0D threshold of $V_0 = 3.5$ cm^3. (A) Aortic arch IV (1D); (B) abdominal aorta V (1D)

representing the entire networks, and even using a local 3D approach at junctions only, would result in an intractable mathematical problem due to its complexity and computational cost when applied to realistic vascular networks.

In 1D junction models, the real geometric structure of a junction of vessels is simplified by imposing that the junction is lumped at one point and by neglecting the effect of the angles between the vessels. Under these assumptions, a domain splitting technique is adopted to cast the global coupling problem into a set of 1D problems, where each vessel is associated with its own intrinsic coordinate system and suitable interface/coupling conditions are required, to appropriately couple the 1D domains converging at the junction point. In this work, this framework has been extended also to junctions of 0D vessels and junctions where 1D and 0D vessels are coupled together.
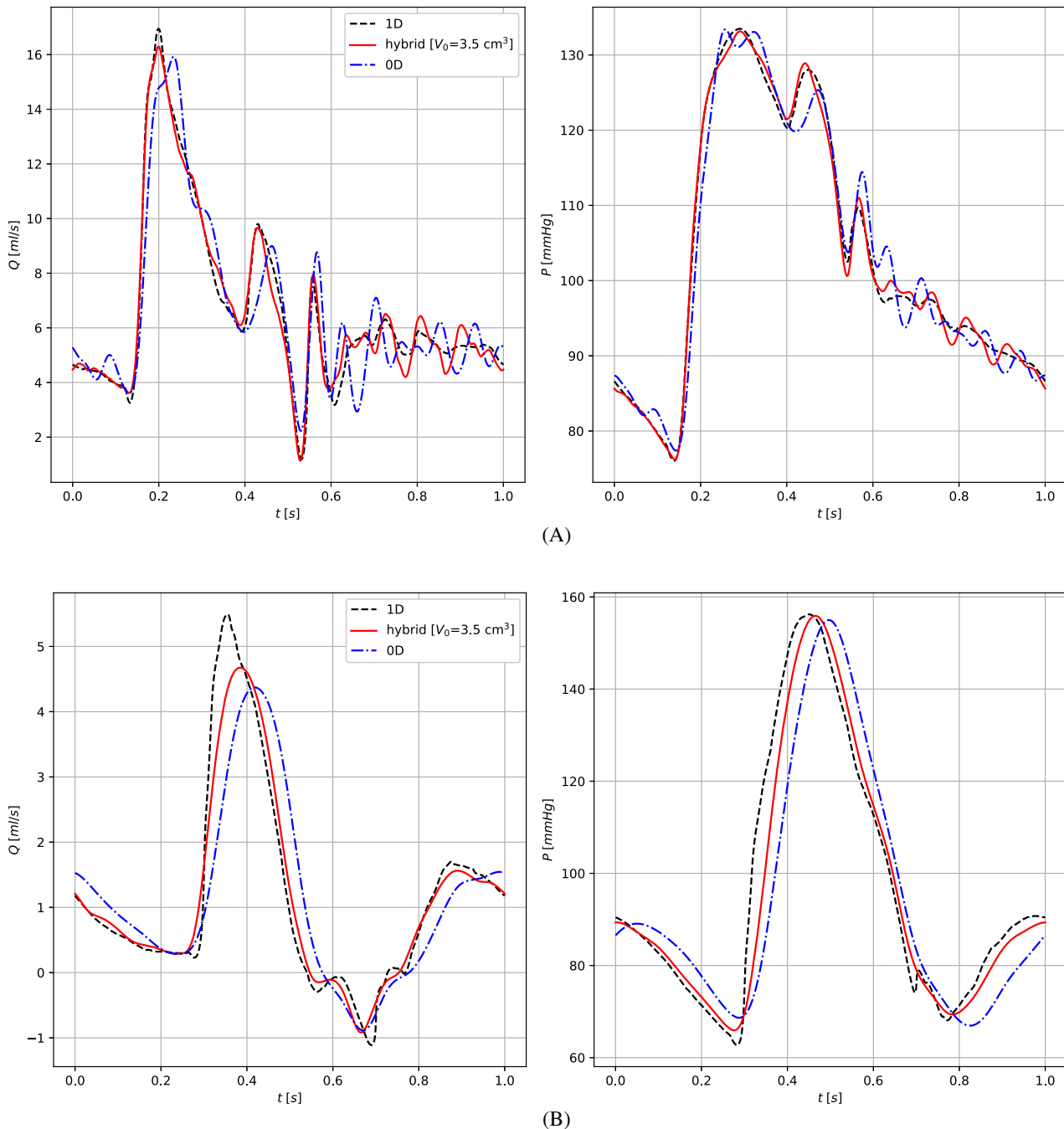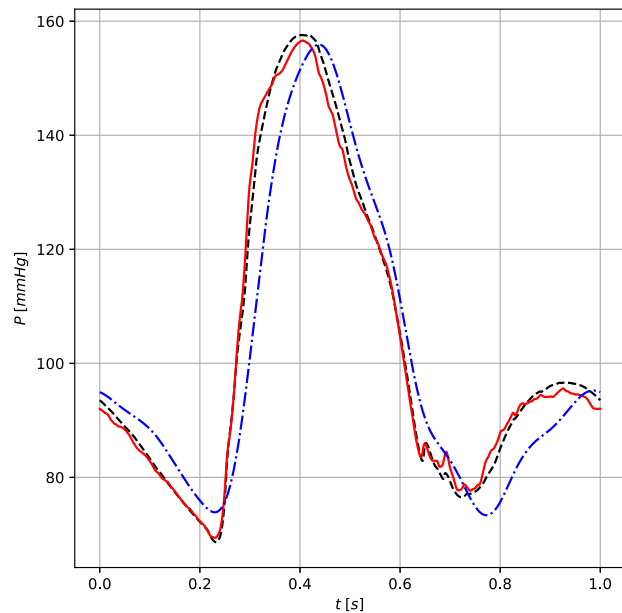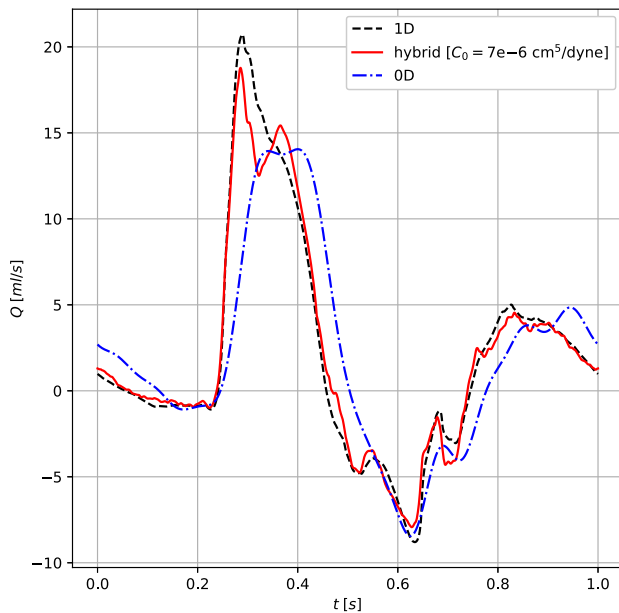
FIGURE 9 Qualitative comparison between computational results for flow rate and pressure obtained from the 1D (dashed black line), the 0D (blue dashed-dotted line), and a hybrid (red continuous line) configuration of **ADAN56 model**, where the last is constructed using the volume V_0 as model selection criterion, with a 1D-0D threshold of $V_0 = 3.5$ cm^3. (A) Right internal iliac (0D); (B) right posterior tibial (0D)

The pure 1D-model-like vessel coupling is a well-established methodology and its validity has been widely documented by works where 1D models have been validated against both in vitro experimental models[1,2] and more complex 3D-FSI models,[32,53] showing that it is reasonable to describe flow at junctions by means of a 1D model, especially when the focus is on reproducing flow rate variation along time, pressure wave propagation and average velocities in vascular networks with a good balance between accuracy and computational cost.

In blood flow in networks, flow splitting at junctions is primarily governed by peripheral resistance (resistances at terminal points of the 1D network representing the downstream vasculature), while its dependence upon the flow characteristics at junctions is negligible. This fact explains why flow is reasonably well-captured by 1D and 0D models. The

FIGURE 10   Qualitative comparison between computational results for flow rate and pressure obtained from the 1D (dashed black line), the 0D (blue dashed-dotted line), and a hybrid (red continuous line) configuration of **ADAN56 model**, where the last is constructed using the compliance C_0 as model selection criterion, with a 1D-0D threshold of $C_0 = 7 \cdot 10^{-6}$ cm^5/dyne. (A) Abdominal aorta III (1D); (B) left popliteal I (1D)

peripheral resistance is indeed orders of magnitude larger than any disturbance in the resistance that a junction can introduce, thus making the contribution of junction losses almost negligible, as largely demonstrated in the previously cited validation studies. For instance, in Reference 1 the authors model energy losses at bifurcations by adding a loss coefficient into the continuity of the total pressure $\left(p + \frac{1}{2}\rho u^2\right)$, which takes into account the branching angles and the flow and area ratios of the vessels joining at the bifurcation. They observe that the addition of these loss coefficients in the simulations does not have a significant effect on pressure and flow waveforms, but energy losses at bifurcations have a secondary, thus negligible, effect on blood flow in large arteries. At least for arteries, in $\left(p + \frac{1}{2}\rho u^2 + losses\right)$, the pressure term p is indeed
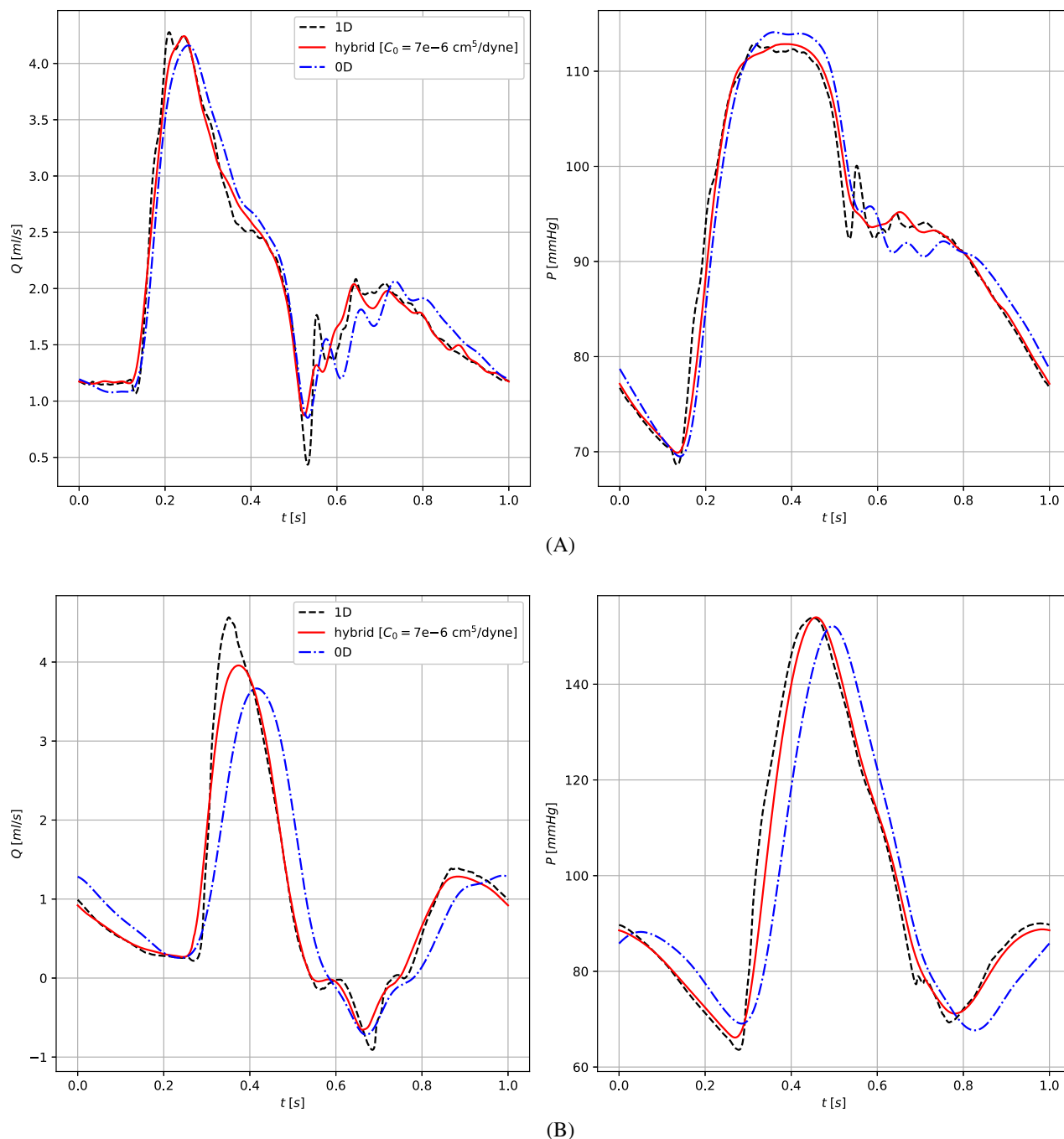
FIGURE 11 Qualitative comparison between computational results for flow rate and pressure obtained from the 1D (dashed black line), the 0D (blue dashed-dotted line), and a hybrid (red continuous line) configuration of **ADAN56 model**, where the last is constructed using the compliance C_0 as model selection criterion, with a 1D-0D threshold of $C_0 = 7 \cdot 10^{-6}$ cm^5/dyne. (A) Right radial (0D); (B) right anterior tibial (0D)

the dominant one, making the total pressure $\left(p + \frac{1}{2}\rho u^2\right)$, or even the pressure p alone (because of the relatively low flow velocities), a suitable coupling condition. Once again, this depends on the fact that peripheral resistance is larger than junction resistance and plays a dominant role in flow splitting at junctions.

The quantitative study performed on the aortic bifurcation model and proposed in the following aims at validating the 1D modeling approach for blood flow in vascular networks with 3D-FSI data and at demonstrating the validity and ability of the 1D formulation to correctly describe flow splitting and wave propagation across junctions of vessels. We consider the aortic bifurcation model of the convergence rate study presented in Section 4.1.4, but with several geometrical

TABLE 16 Geometrical and mechanical properties of the aortic bifurcation model from Reference 53.

Property	Aorta	Iliac arteries
Length, l	12.0 cm	12.0 cm
Radius at diastolic pressure, r_d	0.86 cm	0.60 cm
Wall thickness, h	0.876 mm	0.876 mm
Blood density, ρ	1.060 g/cm^3	
Blood viscosity, μ	0.04 dyne s/cm^2	
Velocity profile order, ζ	9	
Young's modulus, E	6.0·10^6 dyne/cm^2	6.0·10^6 dyne/cm^2
External pressure, p_{ext}	0	
Outflow pressure, P_{out}	-	0
WK resistance, R_1	-	6.8128·10^2 dyne s/cm^5
WK compliance, C	-	3.6678·10^{-5} cm^5/dyne
WK resistance, R_2	-	3.1013·10^4 dyne s/cm^5

and mechanical vessel properties modified according to Reference 53 and reported in Table 16. 3D-FSI data used for comparison and validation of our 1D model were kindly made available to us by the authors of Reference 53 and we refer the reader to this work for further details about the 3D model formulation and resolution. 3D and 1D data are sampled in time at different spatial locations, namely at the mid and end points of the aorta and at the inlet and mid point of the iliac arteries, for pressure, flow rate and radius. In the 1D problem set-up, the diastolic pressure P_d is no longer set to the same values for all vessels, but the diastolic pressure to be prescribed in each 1D vessel is obtained from the corresponding 3D solution at the vessel midpoint as the pressure P^{3D} at which $\Delta R^{3D} = R^{3D} - r_d = 0$, being r_d the vessel radius at diastolic pressure. For both 1D and 3D simulations the output time is taken as $t_{end} = 30T_0$, with $T_0 = 1.1$. The 1D aortic bifurcation model is solved adopting the numerical methods illustrated in Section 3, with $\Delta x_{max} = 1$ mm and $CFL = 0.9$.

First of all, the 1D numerical solution is compared to the 3D data using the following relative error metrics

$$
\varepsilon_X^{\text{RMS}} = \sqrt{\frac{1}{n}\sum_{i=1}^{n}\left(\frac{X_i^{1D}-X_i^{3D}}{X_i^{3D}}\right)^2}, \qquad \varepsilon_Q^{\text{RMS}} = \sqrt{\frac{1}{n}\sum_{i=1}^{n}\left(\frac{Q_i^{1D}-Q_i^{3D}}{\max_j\left(Q_j^{3D}\right)}\right)^2},
$$

$$
\varepsilon_X^{MAX} = \max_i\left|\frac{X_i^{1D}-X_i^{3D}}{X_i^{3D}}\right|, \qquad \varepsilon_Q^{MAX} = \max_i\left|\frac{Q_i^{1D}-Q_i^{3D}}{\max_j\left(Q_j^{3D}\right)}\right|,
$$

$$
\varepsilon_X^{\text{SYS}} = \frac{\max_i\left(X_i^{1D}\right)-\max_i\left(X_i^{3D}\right)}{\max_i\left(X_i^{3D}\right)}, \qquad \varepsilon_Q^{\text{SYS}} = \frac{\max_i\left(Q_i^{1D}\right)-\max_i\left(Q_i^{3D}\right)}{\max_i\left(Q_i^{3D}\right)}, \tag{56}
$$

$$
\varepsilon_X^{\text{DIAS}} = \frac{\min_i\left(X_i^{1D}\right)-\min_i\left(X_i^{3D}\right)}{\min_i\left(X_i^{3D}\right)}, \qquad \varepsilon_Q^{\text{DIAS}} = \frac{\min_i\left(Q_i^{1D}\right)-\min_i\left(Q_i^{3D}\right)}{\max_i\left(Q_i^{3D}\right)},
$$

for flow rate Q and for $X = P$ (pressure), R (radius), P_{tot} (total pressure), with

$$
P_{tot} = P + \frac{1}{2}\rho U^2, \qquad U := \frac{Q}{A} = \frac{Q}{\pi R^2}. \tag{57}
$$

In (56), $i = 1, \ldots, n$ are time points over the cardiac cycle at which the 1D/3D solution is sampled, the superscript "$1D$" denotes the results at each time point i from the 1D simulation at a single spatial location, while the superscript "$3D$" denotes the cross-sectional averaged results at each time point i from the 3D model at a single cross-section.

TABLE 17 Relative errors (in %) in the 1D solution with respect to the 3D solution as defined in (56) evaluated at several spatial location: The midpoint and outlet point of the aorta (parent vessel) and the inlet point and midpoint of the iliac artery (daughter vessel).

Relative errors (%)	Midpoint Ao	Outlet Ao	Inlet Il	Midpoint Il
ε_Q^{RMS}	0.799	1.479	1.169	1.235
ε_P^{RMS}	0.784	0.754	0.728	0.761
ε_R^{RMS}	0.104	0.132	0.496	4.871e-02
$\varepsilon_{P_{tot}}^{RMS}$	0.786	0.757	0.725	0.760
ε_Q^{MAX}	2.616	4.179	3.433	3.256
ε_P^{MAX}	1.992	1.860	1.674	1.730
ε_R^{MAX}	0.186	0.229	1.003	0.113
$\varepsilon_{P_{tot}}^{MAX}$	2.000	1.875	1.665	1.730
ε_Q^{SYS}	−1.109	−1.394	3.143	2.256
ε_P^{SYS}	−5.673e-03	−0.413	−0.574	−0.715
ε_R^{SYS}	−4.712e-02	−8.167e-02	−1.003	−0.109
$\varepsilon_{P_{tot}}^{SYS}$	−1.358e-02	−0.418	−0.579	−0.714
ε_Q^{DIAS}	0.967	1.690	−0.222	8.514e-02
ε_P^{DIAS}	0.406	0.259	0.409	0.306
ε_R^{DIAS}	−1.370e-02	−0.128	9.585e-02	3.960e-02
$\varepsilon_{P_{tot}}^{DIAS}$	0.407	0.259	0.409	0.306

Relative errors between 1D and 3D data are summarized in Table 17. From this table, we can observe that there is a very good agreement between the results predicted by the two models, with errors consistently small in all metrics, variables and vessel locations considered, illustrating that the 1D formulation is able to correctly capture the multiple wave reflections generated at the junction, which contribute to shape pressure, flow and area waveforms in these vessels.

One of the coupling conditions prescribed in the 1D junction model proposed in Section 2.3.1 is the continuity of total pressure. The total pressure variation across the junction from the aorta outlet point to the iliac inlet point is evaluated for both 1D and 3D models according to the following relative error metrics

$$
\varepsilon_X^{\text{RMS},*} = \sqrt{\frac{1}{n}\sum_{i=1}^{n}\left(\frac{X_i^{out,Ao} - X_i^{in,Il}}{X_i^{out,Ao}}\right)^2}, \qquad \varepsilon_X^{\text{MAX},*} = \max_i \left|\frac{X_i^{out,Ao} - X_i^{in,Il}}{X_i^{out,Ao}}\right|,
$$
$$
\varepsilon_X^{\text{SYS},*} = \frac{\max_i\left(X_i^{out,Ao}\right) - \max_i\left(X_i^{in,Il}\right)}{\max_i\left(X_i^{out,Ao}\right)}, \qquad \varepsilon_X^{\text{DIAS},*} = \frac{\min_i\left(X_i^{out,Ao}\right) - \min_i\left(X_i^{in,Il}\right)}{\min_i\left(X_i^{out,Ao}\right)},
$$

(58)

for $X = P_{tot}$, where the superscript "out, Ao" denotes the 1D/3D solution at the outlet point of the aorta, while the superscript "in, Il" denotes the 1D/3D solution at the inlet point of the iliac artery. Relative errors for both 1D and 3D aortic bifurcation models are shown and compared in Table 18. From this table, we can see that there is no variation in total pressure across the 1D junction model, as expected. Furthermore, we observe that the total pressure variation across the 3D junction is also extremely small, with a maximum relative error below 0.5%. These observations are confirmed by the total pressure ratios reported in the same Table 18, which are very close to 1.0 for both 1D and 3D models. Hence, the very little, almost negligible, change in total pressure across the 3D junction suggests that the continuity of total pressure represents a consistent and suitable coupling condition to be prescribed in this kind of reduced-order junction models. Figure 12 displays the total pressure curves at the outlet point of the aorta and at inlet point of the iliac in the 3D model, and at the outlet point of the aorta in the 1D model. The two total pressure profiles from the 3D model are almost perfectly overlapped and the total pressure curve from the 1D model also shows an excellent agreement with the 3D results.

TABLE 18 Comparison between 1D and 3D total pressure variation across the junction.

Relative errors (%)	1D	3D
$\varepsilon_{P_{tot}}^{RMS,*}$	0.000	0.125
$\varepsilon_{P_{tot}}^{MAX,*}$	0.000	0.410
$\varepsilon_{P_{tot}}^{SYS,*}$	0.000	-0.162
$\varepsilon_{P_{tot}}^{DIAS,*}$	0.000	0.149
$\text{mean}\left(\dfrac{P_{tot}^{in,Il}}{P_{tot}^{out,Ao}}\right)$	1.000000	0.999843
$\text{max}\left(\dfrac{P_{tot}^{in,Il}}{P_{tot}^{out,Ao}}\right)$	1.000000	1.001766

Note: Relative errors (in %) in the total pressure at the inlet point of the iliac artery with respect to the total pressure at the outlet point of the aorta are computed as in (58). Mean and maximum values of the total pressure ratio $P_{tot}^{in,Il}/P_{tot}^{out,Ao}$ are also reported for both 1D and 3D aortic bifurcation models.
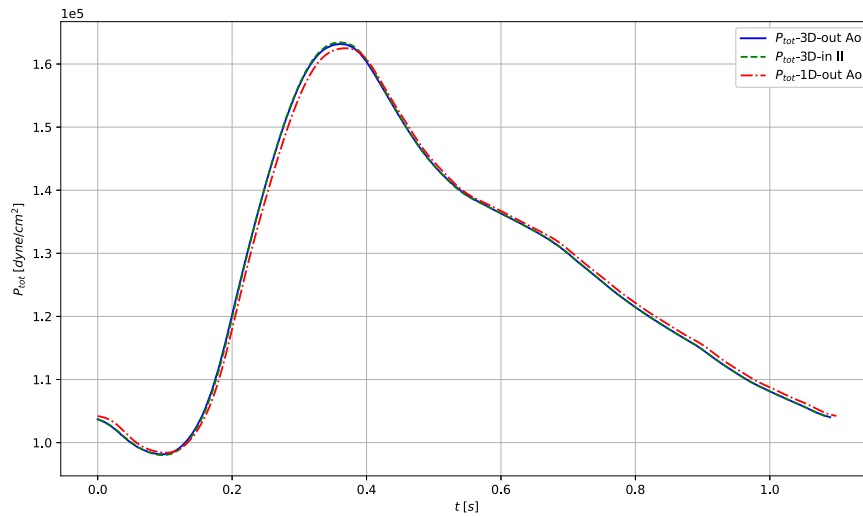
FIGURE 12 Qualitative comparison between total pressure profiles at the outlet point of the aorta (blue continuous line) and at the inlet point of the iliac (green dashed line) of the 3D model, and at the outlet point of the aorta (red dashed-dotted line) of the 1D model.

Next, we analyze the relative contributions of single terms in the total pressure by defining the following coefficients

$$\gamma_P = \frac{P}{P_{tot}}, \qquad \gamma_K = \frac{\frac{1}{2}\rho U^2}{P_{tot}}, \tag{59}$$

for the pressure term P and the kinetic term $\frac{1}{2}\rho U^2$, respectively. Mean and maximum values of the coefficients γ_P and γ_K at several sites are reported in Table 19 for both 1D and 3D models. These results clearly show that the pressure term is the dominant term in the total pressure, while the contribution of the kinetic term is almost negligible (at least in arteries, thanks to the relatively low flow velocities). Once again, this suggests the total pressure, or even the pressure alone, to be a suitable coupling condition for vessels at junctions and this depends on the fact that peripheral resistance is larger than junction resistance, playing a dominant role in flow splitting at junctions.

Next, we define the time integral of the energy flux ($Q \cdot P_{tot}$) as follows

$$E := \int_0^{T_0} (Q(t) \cdot P_{tot}(t)) \; dt, \tag{60}$$

TABLE 19 Analysis of relative contributions of single terms, pressure, and kinetic terms, in the total pressure, estimated according to the coefficients γ_P and γ_K defined in (59) and evaluated at four different locations: Mid and outlet point of the aorta, inlet, and mid point of the iliac artery, for both 1D and 3D models.

	1D				3D			
	Midpoint Ao	**Outlet Ao**	**Inlet Il**	**Midpoint Il**	**Midpoint Ao**	**Outlet Ao**	**Inlet Il**	**Midpoint Il**
mean(γ_P)	0.9996	0.9997	0.9997	0.9998	0.9996	0.9997	0.9997	0.9998
max(γ_P)	1.000	1.000	1.000	1.000	1.000	1.000	1.000	1.000
mean(γ_K)	4.049e-04	2.608e-04	2.874e-04	2.004e-04	4.164e-04	2.745e-04	2.689e-04	1.947e-04
max(γ_K)	3.728e-03	2.520e-03	2.761e-03	1.923e-03	3.737e-03	2.554e-03	2.500e-03	1.791e-03

TABLE 20 Analysis of energy dissipation for both 1D and 3D aortic bifurcation models.

Time integral of energy flux (g cm^2/s^2)	1D	3D
$E_{mid,Ao}$	1194378.136	1216388.680
$E_{out,Ao}$	1192772.882	1203724.804
$E_{in,Il}$	596387.071	600369.322
$E_{mid,Il}$	595231.962	597595.398
$E_{out,il}$	594422.133	595446.895
$E_{out,WK}$	0.000	0.000
Energy dissipation (%)	**1D**	**3D**
$(E_{out,Ao} - 2E_{in,Il})/E_{out,Ao}$	0.000	0.248
$(E_{out,Ao} - 2E_{mid,Il})/E_{out,Ao}$	0.194	0.709
$(E_{out,Ao} - 2E_{out,Il})/E_{out,Ao}$	0.329	1.066
$(E_{out,Ao} - 2E_{out,WK})/E_{out,Ao}$	100.000	100.000
$2(E_{out,Il} - E_{out,WK})/E_{out,Ao}$	99.671	98.934

Note: Values of the time integral of the energy flux defined in (60) at different locations arranged from the midpoint of the aorta to the outlet point of the Windkessel model are reported, together with estimates of the energy dissipation (in %) by the junction (due to the junction resistance) and the Windkessel elements (due to the peripheral resistance).

to quantify the amount of energy associated to a specific vessel location over a complete cycle $[0, T_0]$. This integral is approximated adopting the composite trapezoidal rule and evaluated using the available 1D and 3D numerical solutions at several sites. By taking the outlet point of the aorta as the reference point, the energy dissipation by the junction and by the Windkessel models is estimated by computing the difference of the energy flux time integrals at the aorta reference point and at a selected point along the iliac arteries, normalized with respect to the time integral of the energy flux at the aorta end point. For instance, the energy dissipation by the junction only is computed as

$$E_{diss}^J = \frac{E_{out,Ao} - 2E_{in,Il}}{E_{out,Ao}}. \tag{61}$$

We point out that formula (60) is exact for 1D quantities, while, when applied to the 3D results, it represents only an estimate as it is computed using 1D-like, cross-sectional averaged, quantities. The correct and equivalent formula for 3D signals should make use of the full 3D velocity and pressure fields, which were not available for the present study. As a consequence, here we apply formula (60) also to the cross-sectional averaged 3D results to show that energy in the 1D model behaves like (at least a first-order estimate of) the energy in the 3D model. Table 20 summarizes and compares the results obtained for both 1D and 3D models corresponding to: (i) values of the energy flux time integral computed at several sites of the aorta and iliac arteries; (ii) estimates of energy dissipation (in %) by the junction and the Windkessel elements. From this table, we observe that there is no energy dissipation by the 1D junction, up to convergence errors introduced by the numerical resolution of the nonlinear junction problem, thus concluding that the 1D junction model

is energy-preserving. On the other hand, the energy dissipation by the 3D junction is also very small, of about 0.25% of the total energy estimated at the outlet point of the aorta. Indeed, we can clearly see that the energy is almost entirely dissipated by the Windkessel models: about 99.7% and 98.9% of the total energy at the reference end point of the aorta is dissipated by the Windkessel terminal elements in the 1D and 3D models, respectively. In conclusion, the energy in the 1D model behaves like (at least a first-order estimate of) the energy in the 3D model and the energy dissipated in the 1D model is negligible compared to that of the Windkessel model. This is again determined by the fact that peripheral resistance is significantly larger than junction resistance. To conclude, it is worth noting that the analysis and results presented in this section are valid for physiological situations, while this might not be true in pathological cases, as, for example, in the presence of a stenosis across a junction.

5 | CONCLUDING REMARKS AND FUTURE WORK

One of the main challenges of modeling one-dimensional blood flow in highly complex networks of vessels and cardiovascular models, possibly interacting with other systems and physiological and metabolic models, is the very high computational cost and execution time, which can further increase when long time scales are to be simulated.

In this work, we have proposed an adaptive model selection strategy based on *a-priori* model selection criteria. This methodology allows us to construct hybrid networks of 1D-0D vessels where the computational cost of the simulations is strongly reduced and a good level of accuracy in the predicted results is ensured, to capture and reproduce the main essential features of pressure and flow waveforms in both 1D and 0D vessels. This has been achieved by first developing a methodology for the high-order hybrid numerical coupling between 1D and 0D vessels through junctions. This technique allows to solve coupled 1D and 0D vessels converging at a junction with their own numerical schemes, but taking into account the interaction between these vessels to ensure that the desired order of accuracy of the solution in 1D vessels is preserved. This is done by appropriately approximating the time integral of the boundary flux at the junction interface for each 1D vessel. By applying the adaptive model selection strategy to the 37-artery network and ADAN56 model, we have identified the vessel compliance C_0 and the intravascular volume V_0 to be the most suitable *a-priori* model selection criteria to construct hybrid networks, since for both arterial models they provide the best trade-off between computational efficiency of the simulations and accuracy of the results. For both these criteria, several increasing 1D-0D thresholds generate hybrid configurations of the two arterial networks with more and more 0D vessels which are able to provide a good balance between computational cost, which is considerably reduced, and errors, which remain within a reasonable range and are not growing too much. We emphasize again that an automatic choice of the specific threshold to be used for each parameter, either the volume V_0 or the compliance C_0, was not addressed here, since it may depend on problem-specific characteristics, the aim of the application in mind and thus the required level of accuracy by which the physical process has to be described.

We consider this work as the first step towards a high-performance modeling and computational framework to efficiently solve highly complex networks of 1D-0D vessels. As a first relevant usage of the proposed methodology, this framework will be applied to more complex cardiovascular models, such as the ADAN model developed by Blanco et al.[3,14] and the global, closed-loop, multiscale model of the entire human circulation developed by Müller and Toro[4,13] and recently extended by Toro et al..[18] In addition to integrate the *a-priori* model selection strategy into such models, this methodology will be also improved from both the modeling and numerical point of view. The viscoelastic properties of vessel walls will be included in both 1D and 0D blood flow models, and varying geometrical and mechanical vessel properties will be incorporated in the 1D models. Concerning the numerical and computational aspects, we plan to extend the hybrid numerical coupling to higher-order schemes by adopting, for instance, the ADER approach, and to adapt and integrate the LTS solver proposed by Müller et al. in Reference 22 to solve the hybrid networks, for further computational improvements. Indeed, the utilization of an LTS procedure will become absolutely necessary when this novel methodology is applied to much more complex networks and models, where the heterogeneity of spatial and/or temporal scales is relevant. We expect this adaptive model selection strategy coupled with the LTS solver to be significantly more effective when applied to such models and to determine a further, crucial improvement in terms of computational efficiency.

DATA AVAILABILITY STATEMENT

The data that support the findings of this study are available from the corresponding author upon reasonable request.

ORCID

Beatrice Ghitti 🄳 https://orcid.org/0000-0002-8769-2454

REFERENCES

1. Matthys KS, Alastruey J, Peiró J, et al. Pulse wave propagation in a model human arterial network: assessment of 1-D numerical simulations against in vitro measurements. *J Biomech*. 2007;40(15):3476-3486. doi:10.1016/j.jbiomech.2007.05.027
2. Alastruey J, Khir AW, Matthys KS, et al. Pulse wave propagation in a model human arterial network: assessment of 1-D visco-elastic simulations against in vitro measurements. *J Biomech*. 2011;44(12):2250-2258. doi:10.1016/j.jbiomech.2011.05.041
3. Blanco P, Watanabe S, Passos M, Lemos P, Feijóo R. An anatomically detailed arterial network model for one-dimensional computational hemodynamics. *IEEE Trans Bio-Med Eng*. 2015;62:736-753.
4. Müller LO, Toro EF. A global multiscale mathematical model for the human circulation with emphasis on the venous system. *Int J Numer Methods Biomed Eng*. 2014;30(7):681-725.
5. Aviolo AP. Multi-branched model of the human arterial system. *Med Biol Eng Comput*. 1980;18:709-718. doi:10.1007/BF02441895
6. Stergiopulos N, Young DF, Rogge TR. Computer simulation of arterial flow with applications to arterial and aortic stenoses. *J Biomech*. 1992;25(12):1477-1488. doi:10.1016/0021‐9290(92)90060‐e
7. Olufsen MS, Peskin CS, Kim WY, Pedersen EM, Nadim A, Larsen J. Numerical simulation and experimental validation of blood flow in arteries with structured-tree outflow conditions. *Ann Biomed Eng*. 2000;28:1281-1299. doi:10.1114/1.1326031
8. Formaggia L, Lamponi D, Quarteroni A. One-dimensional models for blood flow in arteries. *J Eng Math*. 2003;47(3/4):251-276.
9. Sherwin SJ, Franke V, Peiró J, Parker KH. One-dimensional modelling of a vascular network in space-time variables. *J Eng Math*. 2003;47:217-250. doi:10.1023/B:ENGI.0000007979.32871.e2
10. Mynard JP, Nithiarasu P. A 1D arterial blood flow model incorporating ventricular pressure, aortic valve and regional coronary flow using the locally conservative Galerkin (LCG) method. *Commun Numer Meth Eng*. 2008;24(5):367-417. doi:10.1002/cnm.1117
11. Reymond P, Merenda F, Perren F, Rüfenacht D, Stergiopulos N. Validation of a one-dimensional model of the systemic arterial tree. *Am J Physiol Heart Circ Physiol*. 2009;297(1):H208-H222. doi:10.1152/ajpheart.00037.2009
12. Reymond P, Bohraus Y, Perren F, Lazeyras F, Stergiopulos N. Validation of a patient-specific one-dimensional model of the systemic arterial tree. *Am J Physiol Heart Circ Physiol*. 2011;301(3):H1173-H1182. doi:10.1152/ajpheart.00821.2010
13. Müller LO, Toro EF. Enhanced global mathematical model for studying cerebral venous blood flow. *J Biomech*. 2014;47(13):3361-3372.
14. Blanco PJ, Watanabe SM, Dari E, Passos MAR, Feijóo RA. Blood flow distribution in an anatomically detailed arterial network model: criteria and algorithms. *Biomech Model Mechanobiol*. 2014;13:1303-1330. doi:10.1007/s10237‐014‐0574‐8
15. Mynard JP, Smolich JJ. One-dimensional haemodynamic modeling and wave dynamics in the entire adult circulation. *Ann Biomed Eng*. 2015;43(6):1443-1460.
16. Blanco PJ, Müller LO, Watanabe SM, Feijóo RA. On the anatomical definition of arterial networks in blood flow simulations: comparison of detailed and simplified models. *Biomech Model Mechanobiol*. 2020;19:1663-1678. doi:10.1007/s10237‐020‐01298‐4
17. Blanco PJ, Müller LO, Spence JD. Blood pressure gradients in cerebral arteries: a clue to pathogenesis of cerebral small vessel disease. *Stroke Vasc Neurol*. 2017;2(3):108-117. doi:10.1136/svn‐2017‐000087
18. Toro EF, Celant M, Zhang Q, et al. Cerebrospinal fluid dynamics coupled to the global circulation in holistic setting: mathematical models, numerical methods and applications. *Int J Numer Meth Biomed Eng*. 2022;38(1):e3532. doi:10.1002/cnm.3532
19. Alastruey J, Moore SM, Parker KH, David T, Peiró J, Sherwin SJ. Reduced modelling of blood flow in the cerebral circulation coupling 1-D, 0-D and cerebral auto-regulation models. *Int. J. Numer. Meth. Fluids*. 2008;56:1061-1067. doi:10.1002/FLD.1606
20. Blanco P, Trenhago P, Fernandes L, Feijóo R. On the integration of the baroreflex control mechanism in a heterogeneous model of the cardiovascular system: modeling the baroreflex mechanism in the cardiovascular system. *Int J Numer Meth Biomed Eng*. 2012;28(4):412-433. doi:10.1002/cnm.1474
21. Fernandes LG, Trenhago PR, Feijóo RA, Blanco PJ. Integrated cardiorespiratory system model with short timescale control mechanisms. *Int J Numer Meth Biomed Eng*. 2021;37(11):e3332. doi:10.1002/cnm.3332
22. Müller L, Blanco P, Watanabe S, Feijóo R. A high-order local time stepping finite volume solver for one-dimensional blood flow simulations: application to the ADAN model. *Int J Numer Methods Biomed Eng*. 2015;32(10):2761. doi:10.1002/cnm.2761
23. Fossan FE, Mariscal-Harana J, Alastruey J, Hellevik LR. Optimization of topological complexity for one-dimensional arterial blood flow models. *J R Soc Interf*. 2018;15(149):20180546. doi:10.1098/rsif.2018.0546

24. Epstein S, Willemet M, Chowienczyk PJ, Alastruey J. Reducing the number of parameters in 1D arterial blood flow modeling: less is more for patient-specific simulations. *Am J Physiol Heart Circ Physiol*. 2015;309(1):H222-H234. doi:10.1152/ajpheart.00857.2014

25. Safaei S, Blanco PJ, Müller LO, Fossan FE, Hellevik LR, Hunter PJ. Bond graph model of cerebral circulation: toward clinically feasible systemic blood flow simulations. *Front Physiol*. 2018;9:148. doi:10.3389/fphys.2018.00148

26. Mirramezani M, Shadden SC. A distributed lumped parameter model of blood flow. *Ann Biomed Eng*. 2020;48(12):2870-2886. doi:10.1007/s10439‐020‐02545‐6

27. Ghitti B, Toro EF, Müller LO. Nonlinear lumped-parameter models for blood flow simulations in networks of vessels. *ESAIM M2AN*. 2022;56(5):1579-1627. doi:10.1051/m2an/2022052

28. Toro EF, Siviglia A. Flow in collapsible tubes with discontinuous mechanical properties: mathematical model and exact solutions. *Commun Comput Phys*. 2013;13(2):361-385.

29. Spilimbergo A, Toro EF, Müller LO. One-dimensional blood flow with discontinuous properties and transport: mathematical analysis and numerical schemes. *Commun Comput Phys*. 2021;29(3):649-697. doi:10.4208/cicp.OA‐2020‐0132

30. Müller L, Blanco P. A high order approximation of hyperbolic conservation laws in networks: application to one-dimensional blood flow. *J Comput Phys*. 2015;300:423-437.

31. Reymond P, Crosetto P, Deparis S, Quarteroni A, Stergiopulos N. Physiological simulation of blood flow in the aorta: comparison of hemodynamic indices as predicted by 3-D FSI, 3-D rigid wall and 1-D models. *Med Eng Phys*. 2013;35(6):784-791. doi:10.1016/j.medengphy.2012.08.009

32. Xiao N, Alastruey J, Figueroa CA. A systematic comparison between 1-D and 3-D hemodynamics in compliant arterial models. *Int J Numer Method Biomed Eng*. 2014;30(2):204-231. doi:10.1002/cnm.2598

33. Boileau E, Nithiarasu P, Blanco PJ, et al. A benchmark study of numerical schemes for one-dimensional arterial blood flow modelling. *Int J Numer Methods Biomed Eng*. 2015;31(10):e02732.

34. Alastruey J, Xiao N, Fok H, Schaeffter T, Figueroa CA. On the impact of modelling assumptions in multi-scale, subject-specific models of aortic haemodynamics. *J R Soc Interf*. 2016;13(119):20160073. doi:10.1098/rsif.2016.0073

35. Moore SM, Moorhead KT, Chase JG, David T, Fink J. One-dimensional and three-dimensional models of cerebrovascular flow. *J Biomech Eng*. 2005;127(3):440-449. doi:10.1115/1.1894350

36. Grinberg L, Cheever E, Anor T, Madsen JR, Karniadakis GE. Modeling blood flow circulation in intracranial arterial networks: a comparative 3D/1D simulation study. *Ann Biomed Eng*. 2011;39(1):297-309. doi:10.1007/s10439‐010‐0132‐1

37. Blanco PJ, Bulant CA, Müller LO, et al. Comparison of 1D and 3D models for the estimation of fractional flow reserve. *Sci Rep*. 2018;8(1):17275. doi:10.1038/s41598‐018‐35344‐0

38. Fossan FE, Sturdy J, Müller LO, et al. Uncertainty quantification and sensitivity analysis for computational FFR estimation in stable coronary artery disease. *Cardiovasc Eng Technol*. 2018;9(4):597-622. doi:10.1007/s13239‐018‐00388‐w

39. Müller LO, Fossan FE, Bråten TA, Jørgensen A, Wiseth R, Hellevik LR. Impact of baseline coronary flow and its distribution on fractional flow reserve prediction. *Int J Numer Method Biomed Eng*. 2019;37(11):e3246.

40. Fossan FE, Müller LO, Sturdy J, et al. Machine learning augmented reduced-order models for FFR-prediction. *Comput Methods Appl Mech Eng*. 2021;384:113892. doi:10.1016/j.cma.2021.113892

41. Saito M, Ikenaga Y, Matsukawa M, Watanabe Y, Asada T, Lagrée PY. One-dimensional model for propagation of a pressure wave in a model of the human arterial network: comparison of theoretical and experimental results. *J Biomech Eng*. 2011;133:121005. doi:10.1115/1.4005472

42. Toro EF. Brain venous haemodynamics, neurological diseases and mathematical modelling. A review. *Appl Math Comput*. 2016;272:542-579.

43. Formaggia L, Quarteroni A, Veneziani A, eds. *Cardiovascular Mathematics: Modeling and Simulation of the Circulatory System*. No. 1 in MS & A: Modeling, Simulation & Applications. Springer; 2009.

44. Formaggia L, Veneziani A. *Reduced and multiscale models for the human cardiovascular system*. Technical report, Politecnico di Milano; 2015.

45. Milišić V, Quarteroni A. Analysis of lumped parameter models for blood flow simulations and their relation with 1D models. *ESAIM M2AN*. 2004;38(4):613-632. doi:10.1051/m2an:2004036

46. van Leer B. On the Relation between the Upwind–Differencing Schemes of Godunov, Engquist-Osher and Roe. *SIAM J Sci Stat Comput*. 1985;5(1):1-20.

47. Harten A, Osher S. Uniformly high–order accurate nonoscillatory schemes. I. *SIAM J Numer Anal*. 1987;24(2):279-309.

48. Harten A, Engquist B, Osher S, Chakravarthy SR. Uniformly high order accuracy essentially non–oscillatory schemes, III. *J Comput Phys*. 1987;71:231-303.

49. Toro E, Millington R, Nejad L. Towards very high-order Godunov schemes. In: Toro EF, ed. *Godunov Methods: Theory and Applications. Edited Review*. Kluwer Academic/Plenum Publishers; 2001:905-937.

50. Castro CE, Toro EF. Solvers for the high-order Riemann problem for hyperbolic balance laws. *J Comput Phys*. 2008;227(4):2481-2513. doi:10.1016/j.jcp.2007.11.013

51. Harten A, Lax PD, van Leer B. On upstream differencing and Godunov–type schemes for hyperbolic conservation laws. *SIAM Rev*. 1983;25(1):35-61.

52. Toro EF. *Riemann Solvers and Numerical Methods for Fluid Dynamics: A Practical Introduction*. 3rd ed. Springer-Verlag; 2009.

53. Borsche R, Kall J. High order numerical methods for networks of hyperbolic conservation laws coupled with ODEs and lumped parameter models. *J Comput Phys.* 2016;327:678-699. doi:10.1016/j.jcp.2016.10.003

54. Jin W, Alastruey J. Arterial pulse wave propagation across stenoses and aneurysms: assessment of one-dimensional simulations against three-dimensional simulations and in vitro measurements. *J R Soc Interf*. 2021;18(177):20200881. doi:10.1098/rsif.2020.0881

55. Dumbser M, Käser M. Arbitrary high order non-oscillatory finite volume schemes on unstructured meshes for linear hyperbolic systems. *J Comput Phys.* 2007;221(2):693-723. doi:10.1016/j.jcp.2006.06.043

SUPPORTING INFORMATION

Additional supporting information can be found online in the Supporting Information section at the end of this article.